Geoscientific
Model Development

CHIMERE 2013: a model for regional atmospheric composition modelling

L. Menut[1], B. Bessagnet[2], D. Khvorostyanov[1], M. Beekmann[3], N. Blond[4], A. Colette[2], I. Coll[3], G. Curci[5], G. Foret[3], A. Hodzic[6], S. Mailler[1], F. Meleux[2], J.-L. Monge[1], I. Pison[7], G. Siour[3], S. Turquety[1], M. Valari[1], R. Vautard[7], and M. G. Vivanco[8]

[1]Laboratoire de Météorologie Dynamique, IPSL, CNRS, UMR8539, 91128 Palaiseau Cedex, France
[2]Institut national de l'environnement industriel et des risques, Parc technologique ALATA, 60550 Verneuil en Halatte, France
[3]Laboratoire Interuniversitaire des Systèmes Atmosphériques, IPSL, CNRS, UMR 7583, Université Paris Est Créteil (UPEC) and Université Paris Diderot (UPD), Créteil, France
[4]Laboratoire Image Ville Environnement, CNRS/UDS, UMR7362, Strasbourg, France
[5]Dipartimento di Scienze Fisiche e Chimiche – CETEMPS, Universita degli Studi dell'Aquila, L'Aquila, Italy
[6]NCAR Atmospheric Chemistry Division, 3450 Mitchell Lane, Boulder, Colorado, USA
[7]Laboratoire des Sciences du Climat et de l'Environnement, IPSL, CEA-CNRS-UVSQ, UMR8212, Gif sur Yvette, France
[8]Environment Department, CIEMAT, Madrid, Spain

Correspondence to: L. Menut (menut@lmd.polytechnique.fr)

Abstract. Tropospheric trace gas and aerosol pollutants have adverse effects on health, environment and climate. In order to quantify and mitigate such effects, a wide range of processes leading to the formation and transport of pollutants must be considered, understood and represented in numerical models. Regional scale pollution episodes result from the combination of several factors: high emissions (from anthropogenic or natural sources), stagnant meteorological conditions, kinetics and efficiency of the chemistry and the deposition. All these processes are highly variable in time and space, and their relative contribution to the pollutants budgets can be quantified with chemistry-transport models. The CHIMERE chemistry-transport model is dedicated to regional atmospheric pollution event studies. Since it has now reached a certain level a maturity, the new stable version, CHIMERE 2013, is described to provide a reference model paper. The successive developments of the model are reviewed on the basis of published investigations that are referenced in order to discuss the scientific choices and to provide an overview of the main results.

1 Introduction

The rapid growth of urban areas and increased industrialisation have created the need for air quality assessment and motivated the first regional-scale studies on anthropogenic pollution in the early 1990s (Fenger, 2009, among others). The first systematic measurements have been implemented by the air quality agencies in the source regions, which often coincided with the most densely populated areas. One of the first targeted pollutants was sulphur dioxide due to its effects on acid rain and forest ecosystems.

As a result of emission reductions enforced in the industrial activity sector, concentrations of sulphur dioxide were greatly reduced in the 1990s. Then the focus was shifted to other gaseous pollutants such as ozone and nitrogen oxides that were shown to have adverse health effects on populations. More recently, particles have become a priority. In parallel, research on biogenic pollution has long been more modest in contrast to anthropogenic sources. Having no possible influence on biogenic pollutants, the research community has perceived these sources, perhaps erroneously, as less intense or less important to study.

Even if air pollution was considered as a local and mostly urban problem, it has been shown that ozone and its precursors may be transported over long distances. Therefore, to study local pollution and represent effects of anthropogenic and biogenic emissions, chemistry and transport on the local pollution budget, models need to integrate processes over large spatial scales. While early models were based on statistical assumptions and could not account for sporadic changes in the atmospheric forcing, the past two decades have seen the development of deterministic and Eulerian models. Some of these models are very complex and dedicated to field or idealised studies of a few days, over specific regions. Others are dedicated to long-range transport only. In addition, some models allow fast simulations and are thus suitable for daily forecast, Monks (2009).

The CHIMERE model has been in development for more than fifteen years and is intended to be a modular framework available for community use. It includes the necessary state-of-the-art parameterisations to simulate reasonable pollutant concentrations, but remains also computationally efficient for forecast applications. CHIMERE is also frequently used for field experiment analysis studies, long-range transport and trend quantification over continental scales. Designed for both the research community and operational agencies, the CHIMERE model needs to be computationally stable and provide robust results. This means that the model needs to be able to estimate pollution peaks at the right time and location, but also to be able to diagnose low pollution conditions and avoid false alerts. As a research tool, the model needs to be modular enough to allow adding new processes or testing specific physico–chemical interactions. In the present paper we describe the parameterisations included in the CHIMERE model and the results of recent studies explaining the rationale of the last model improvements.

This paper represents the reference model description for CHIMERE version 2013. An overview of the CHIMERE model structure is given in Sect. 2. The domains definition and the boundary conditions are described in Sect. 3. The meteorological forcings and their preprocessing are presented in Sect. 4 and the implementation of transport and mixing is discussed in Sect. 5. The emissions taken into account in the model (anthropogenic, biogenic, mineral dust, fires and the local resuspension of particulate matter) are described in Sect. 6. The gaseous and aerosol chemistries are presented in Sect. 7. The dry and wet deposition processes are presented in Sect. 8 and the cloud impacts in Sect. 9. The CHIMERE model results evaluations are discussed in Sect. 10. The hybridation between model and observations (for sensitivity, inverse modelling and data assimilation) are presented in Sect. 11. The experimental and operational forecasts operated with CHIMERE are described in Sect. 12. Finally, a summary and new research directions are presented in Sect. 14.

The main goal of this paper is to describe in detail all the numerical and scientific choices and to explain the main reasons for these choices. In addition, ongoing and planned developments and application studies are presented.

2 CHIMERE model overview

2.1 Main characteristics

CHIMERE is an Eulerian off-line chemistry-transport model (CTM). External forcings are required to run a simulation: meteorological fields, primary pollutant emissions, and chemical boundary conditions. Using these input data, CHIMERE calculates and provides the atmospheric concentrations of tens of gas-phase and aerosol species over local to continental domains (from 1 km to 1 degree resolution). The key processes affecting the chemical concentrations represented in CHIMERE are emissions, transport (advection and mixing), chemistry and deposition, as presented in Fig. 1. Note that forcings have to be on the same grid and time step as the CTM simulation. In this sense, CHIMERE is not only a chemical model but a suite of numerous preprocessing programs able to prepare the simulation. The model is now used for pollution event analysis, scenario studies, operational forecast and more recently for impact studies of pollution on health (Valari and Menut, 2010) and vegetation (Anav et al., 2011).

The first model version was released in 1997 and was a box model covering the Paris area and included only gas-phase chemistry (Honoré and Vautard, 2000; Vautard et al., 2001). In 1998, the model was implemented for its first forecast version (Pollux) during the ESQUIF (Etude et Simulation de la QUalité de l'air en Ile de France) experiment (Menut et al., 2000b), again over the Paris area (Vautard et al., 2000). At the same time, the adjoint model was developed to estimate the sensitivity of concentrations to all parameters (Menut et al., 2000a). In 2001, the geographical domain was extended over Europe with a cartesian mesh (Schmidt et al., 2001) and the new experimental forecast platform (PIONEER) was set up. In 2003, the experimental forecast became operational with the PREV'AIR (French air quality forecasting and mapping system) system operated at INERIS (National Institute for Industrial Environment and Risks) (Honoré et al., 2008; Rouïl et al., 2009). The aerosol module was implemented in 2004 (Bessagnet et al., 2004) with further improvements concerning the dust natural emissions and resuspension over Europe (Vautard et al., 2005, Hodzic et al., 2006a; Bessagnet et al., 2008) and evaluated against long-term and field measurements (Hodzic et al., 2005, 2006b). The development of the mineral dust version started in 2005 (Menut et al., 2005b). Chemistry was not included in that version and a new horizontal domain had to be designed to cover the whole northern Atlantic and Europe, including the Sahara and downwind regions. In 2006, an important step was achieved with the development of the parallel version of the model and its first implementation on a massively parallel computer
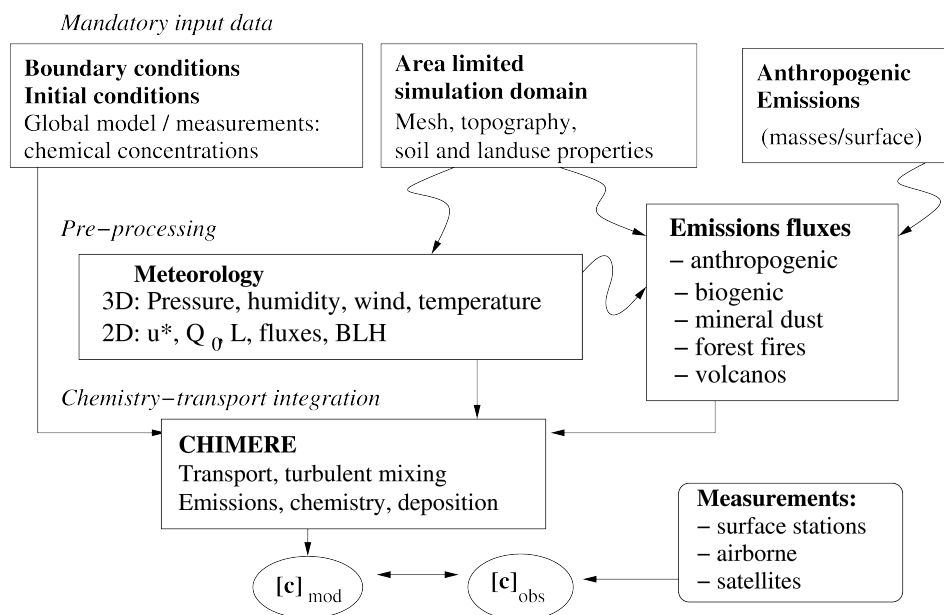
Fig. 1. General principle of a chemistry-transport model such as CHIMERE. In the box "Meteorology", u_* stands for the friction velocity, Q_0 the surface sensible heat flux, L the Monin–Obukhov length and BLH the boundary layer height. c_{mod} and c_{obs} are the modelled and the observed chemical concentrations fields, respectively.

(the ECMWF (European Centre for Medium-Range Weather Forecasts) computer within the framework of the FP6/GEMS (Global and regional Earth-system Monitoring using Satellite and in situ data) project).

The CHIMERE model is now considered a state-of-the-art model. It has been involved in numerous inter-comparison studies focusing mainly on ozone and PM_{10} from the urban scale (Vautard et al., 2007; Van Loon et al., 2007; Schaap et al., 2007) to continental scale (Solazzo et al., 2012b; Zyryanov et al., 2012). The model has been mainly applied over Europe, and more recently over Africa and the North Atlantic for dust simulations, over Central America during the MILAGRO (Megacity Initiative: Local and Global Research Observations) project to study organic aerosols (Hodzic et al., 2009, 2010a,b), and over the US within the AQMEII (Air Quality Model Evaluation International Initiative) project (Solazzo et al., 2012b).

Finally, the development of CHIMERE follows three main rules. First, concentrations of main pollutants are calculated with the best possible accuracy using well evaluated and state-of-the-art parameterisations. Second, a modular framework is maintained to allow updates to the code by developers and also all interested users. Third, the code is kept computationally efficient to allow long-term simulations, climatological studies and operational forecast.

2.2 The CHIMERE software

In order to facilitate software distribution, CHIMERE is protected under the General Public License. This paper presents the latest model version release called CHIMERE 2013. The source code and the associated documentation is available on the website www.lmd.polytechnique.fr/chimere. The documentation is both technical and scientific. It includes a chapter dedicated to the set-up of a test case simulation that allows new users to easily carry out a CHIMERE simulation: model configuration and data (meteorology and emissions files) are provided to simulate the 2003 heatwave in western Europe.

CHIMERE is a National Tool of the French Institut National des Sciences de l'Univers, meaning that support has to be provided to the users of model. Two mailing lists exist for this support: chimere@lmd.polytechnique.fr to send questions to the model developers and chimere-users@lmd.polytechnique.fr to initiate discussions, exchange programs or data between users. In addition, two-day training courses are organised twice a year. Each training course is free of charge for participants and offers complete training to be able to install the code, launch a simulation and change surface emissions or other parameters in the code.

The code is completely written in Fortran90, and running scripts are written in shell (using GNU awk for input datafiles processing). The required software is a Fortran 95 compiler (g95 and gfortran are both free and efficient, but Makefiles with Intel's ifort compiler options are also provided). The required libraries are NetCDF (either 3.6.x or 4.x.x), MPI (see

below), and GRIB API (associated to the use of the ECMWF meteorological datasets). The model includes tools that can help the user to configure the model's Makefiles for the libraries already installed.

The model computation time for one AMDx64 node of 16 CPUs is 1 h 30 min for 1 month of simulation for the Paris area, at 15 km resolution, the domain size being $45 \times 48 \times 8$ with a time step of 360 s on average. CHIMERE uses the distributed memory scheme, and MPI message passing library. It is maintained for Open MPI (recommended) and LAM/MPI, but works, with minor changes in the scripts, with MPICH or other MPI compatible parallel environments. The model parallelism results from a Cartesian division of the main geographical domain into several subdomains, each one being processed by a worker process. Each worker performs the model integration in its geographical sub-domain as well as boundary condition exchanges with its neighbours. In addition a master process performs initialisations and file input/output. To configure the parallel sub-domains, the user has to specify two parameters in the model parameter file: the number of sub-domains for the zonal and meridional directions. The total number of CPUs used is therefore the product of these two numbers, plus one CPU for the master process.

For graphical postprocessing, simple interfaces are available using either the GMT 5 or the GrADS 6 free software. Also, an additional graphical user interface (GUI) software CHIMPLOT is provided. It allows making various 1-D or 2-D plots (e.g. longitude, latitude or time, altitude maps; vertical slices; time series; vertical profiles). One can also overlay multiple fields (e.g. O_3 concentrations, wind vectors, and pressure contours) and perform simple operations such as calculating daily maxima, daily means, vertical or horizontal averaging or integrations.

2.3　The CHIMERE code organisation

Apart from the preprocessing, i.e. the preparation of the forcing, the CHIMERE model is split into two main parts: an initialisation phase and the model integration phase (Fig. 2).

The initialisation phase consists in reading all input parameters as well as the preparation of the initial meteorological and chemical field.

The model integration phase is split into three stages:

– An hourly time step that corresponds to the provision of forcings, i.e. meteorological fields, emission fluxes and chemical boundary conditions.

– A user's defined coarse time step "nphour", corresponding to the time interpolation of "physical" parameters, such as wind, temperature, reactions rates, etc. In parallel, to optimise the time simulation and prevent issues associated to the violation of the Courant–Friedrich–Levy (CFL) criteria, a "physical" time step is dynamically estimated in the meteorological preprocessor,
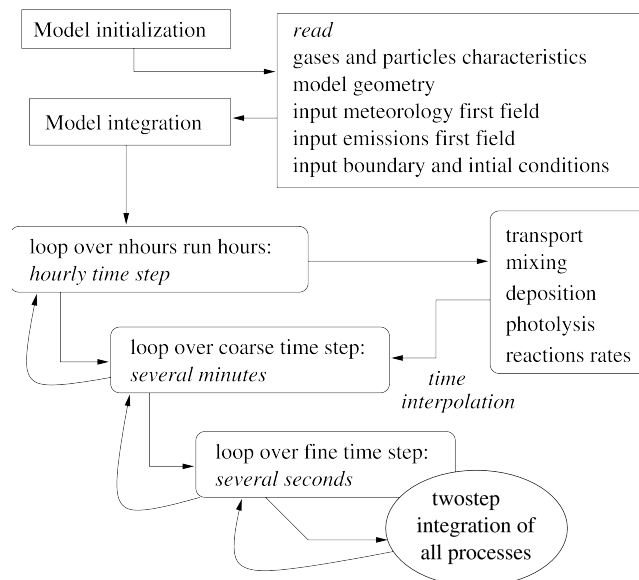

Fig. 2. General CHIMERE structure for time integration of all processes.

taking into account horizontal and vertical winds and deep convective updraft, as presented in Fig. 3. During the run, if the specified time step is longer than the recommended time step, the recommended time step will be used in model integrations. If the user's defined time step is shorter as the recommended one, the user's choice is applied (even if this is not the optimal choice).

– A user's defined fine time step "ichemstep": this corresponds to the integration of the chemical mechanism, including concentration increments due to all processes. This is achieved by the two-step scheme. Due to the stiffness of the chemical system to solve, this time step must be at least 30 s (or less if possible). In practice, for large domains, such as western Europe, a "very quick formulation" with a 10 min physical step and no subchemical steps, i.e. all processes are stepped to 10 min, is realistic. It is possible to select one or two Gauss–Seidel iterations, but the use of two iterations is strongly recommended even if it increases the computer time by two.

The numerical integration of all processes follows a production-loss budget approach, as presented in Fig. 4. This means that all production and loss terms for each chemical species are calculated simultaneously to avoid error propagation generally created with operator-splitting techniques (the concentration evolution being dependent on the several terms order; McRae et al., 1982). Further advantages of the scheme are (1) its stability even for quite long time steps due to the implicitness of the formulation and (2) the simplicity of the
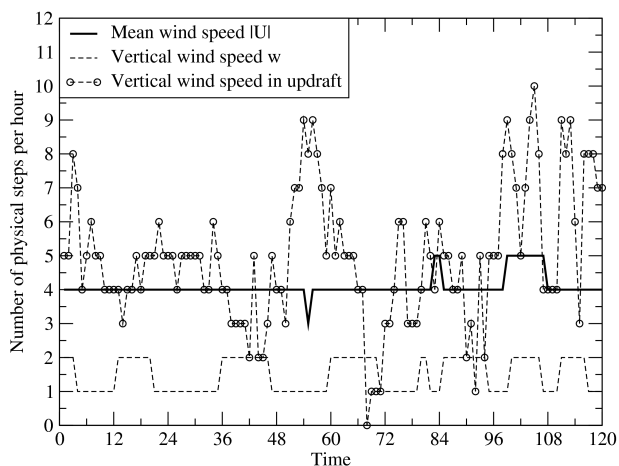
Fig. 3. Calculation of the number of integration steps per hour to respect the Courant–Friedrich–Levy (CFL) number over a complete 120 h simulation. The CFL is estimated using three parameters: the mean wind speed $|U|$, the vertical wind speed in the environment w, and the vertical velocity in the updraft in case of active deep convection.

Fig. 4. Principle of "operator-splitting" versus CHIMERE integration.

code, which facilitates the development of secondary models (adjoint, tangent linear).

The numerical method used to estimate the temporal solution of the stiff system of partial differential equations is adapted from the second-order TWOSTEP algorithm originally proposed by Verwer (1994) for gas-phase chemistry only. It is based on the application of a Gauss–Seidel iteration scheme to the 2-step implicit backward differentiation (BDF2) formula:

$$c^{n+1} = \frac{4}{3}c^n - \frac{1}{3}c^{n-1} + \frac{2}{3}\Delta t R(c^{n+1}) \tag{1}$$

with c^n being the vector of chemical concentrations at time t_n, Δt the time step leading from time t_n to t_{n+1}, and $R(c) = \dot{c} = P(c) - L(c)c$ the temporal evolution of the concentrations due to chemical production and emissions (P) and chemical loss and deposition (**L**). Note that **L** is a diagonal matrix here. After rearranging and introducing the production and loss terms this equation reads

$$c^{n+1} = \left(I + \frac{2}{3}\Delta t L(c^{n+1}) \right)^{-1}$$
$$\times \left(\frac{4}{3}c^n - \frac{1}{3}c^{n-1} + \frac{2}{3}\Delta t P(c^{n+1}) \right) \tag{2}$$

The implicit nonlinear system obtained can be solved pertinently with a Gauss–Seidel method (Verwer, 1994).

In CHIMERE the production and loss terms P and L in Eq. (2) are replaced by the modified terms $\tilde{P} = P + P_h + P_v$ and $\tilde{L} = L + L_h + L_v$, respectively. P_h and P_v denote the temporal evolution of the concentrations due to horizontal
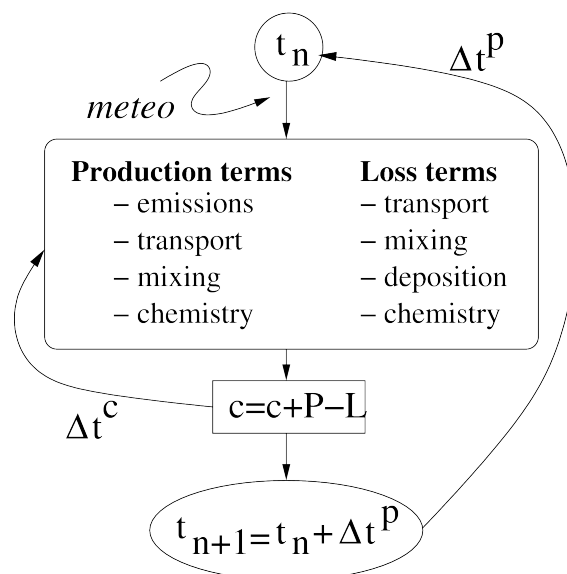
(only advection) and vertical (advection and diffusion) inflow into a given grid box; L_h and L_v give the temporal evolution due to the respective outflow divided by the concentration itself.

3 Domains and boundary conditions

3.1 Domains geometry

Model domains are defined by their grid cell centres. The user controls the model grid through a simple longitude/latitude ASCII file, in decimal degrees. The input meteorological fields are automatically interpolated on the CHIMERE grid. Each pair of coordinates stands for a grid cell centre, described (from the top to the bottom of the file) from west to east then from south to north.

In the definition of a new CHIMERE domain, the user must check carefully whether the domain is quasi-rectangular. Most projections work, including a regular grid in geographic coordinates (longitude, latitude), provided the resolution is not too coarse (more than ≈ 2 degrees). The model grid can be any quasi-rectangular grid with a slowly varying spatial step. In the use of piecewise parabolic method for horizontal transport, the grid size being considered as constant in each direction locally (over 5 consecutive cells), it is recommended to define a rectangular grid. The sphericity effects, although taken into account, are therefore linearised.

The model uses any number of vertical layers described in hybrid sigma–pressure ($\sigma - p$) coordinates. The pressure, p_k, in hPa at the top of each layer k is given by the following formula:

$$p_k = a_k\, p_0 + b_k\, p_{\text{surf}}, \tag{3}$$

where p_{surf} is the surface pressure, and p_0 is a reference state pressure ($p_0 = 1000\,\text{hPa}$). a_k and b_k are the hybrid coefficients and can be provided by the user (to manually force the depth of each model vertical layer) or is calculated by the model. In this latter case, the user has only to provide the number of vertical levels, the pressure values at the top of the first and last layers. The vertical resolution varies upward in a geometric progression.

Table 1 gives examples of domains for which CHIMERE has been run and/or evaluated. These domains range from hemispheric scale for the simulation of long-range dust transport with a horizontal resolution of 50 km to simulations at the urban area scale (Valari et al., 2011; Menut et al., 2013) with a resolution of about 5 km. The most frequently used vertical discretisation consists of 8 vertical levels, from sigma level 0.995 to the 500 hPa pressure level, independently of the horizontal resolution, which is the configuration of the PREV'AIR operational forecast system (Rouïl et al., 2009). For other applications, such as long-range transport of dust or volcano ashes, which require a better representation of the free troposphere, more levels are used (15 levels up to 200 hPa in Menut et al., 2009a, 18 levels up to 200 hPa in Boichu et al., 2013). However, regarding the modelling of anthropogenic pollution, it has been shown that increasing the number of levels from 8 to 20 levels does not modify substantially the modelled concentration at ground levels. The thickness of the first model layer is however a critical parameter, and adding a new vertical layer close to the surface at the sigma-level 0.999 (instead of 0.995) significantly impacts the modelled concentrations, particularly during nighttime in the case of very stable boundary layers (Menut et al., 2013).

3.2 Land use types

Land use types, or categories, are needed by CHIMERE to calculate a number of processes, such as deposition, biogenic emissions, or surface layer momentum and heat transfer. Land use files need to be constructed only once per model domain. There are currently 9 land use categories in CHIMERE. Those categories are calculated from available global land use databases, which can contain different numbers of classes. The source code version comes with land use data and interfaces for two databases: the Global Land Cover Facility (GLCF) and the GlobCover Land Cover (LC).

GLCF is a 1 km × 1 km resolution database from the University of Maryland, following the methodology of Hansen and Reed (2000). This global land cover classification is based on the imagery from the AVHRR satellites analysed to distinguish 14 land cover classes. The GlobCover LC is a global land cover map at 10 arc second (300 m) resolution (Bicheron et al., 2011). It contains 22 global land cover
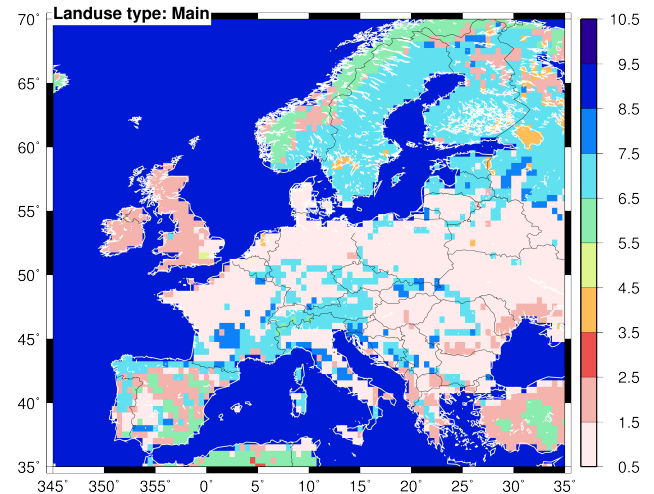

Fig. 5. Example of GLCF land use regridded over a CHIMERE domain: the western European domain used for the GEMS project with a horizontal resolution of 0.5×0.5 degrees. For each cell the dominant land use is shown. The colour code correspond to the land use number (with 1 between 0.5 and 1.5, for example). The codes are: (1) Agricultural land/crops, (2) grassland, (3) barren land, (4) inland water, (5) urban, (6) shrubs, (7) needleleaf forest, (8) broadleaf forest, (9) ocean.

classes defined within the UN Land Cover Classification System (LCCS). GlobCover database is based on the ENVISAT satellite mission's MERIS sensor (Medium Resolution Image Spectrometer) level 1B data acquired in full resolution (FR) mode with a spatial resolution of 300 m. GlobCover LC was derived from an automatic and regionally-tuned classification of a time series of MERIS FR composites covering the period December 2004–June 2006. The global land cover NetCDF files are provided along with the CHIMERE distribution.

The nine CHIMERE land use types are described in Table 2. The correspondence table between the database land use types and the CHIMERE land use types is provided with the model. The user can choose either GLCF or GlobCover by simply selecting a flag; a dedicated sequence of scripts and programs prepares the land use file in the CHIMERE format. An additional class "inland water" has been added to the classifications in both land cover databases to distinguish between sea water and fresh water. This feature was required to avoid model emissions of sea salt over fresh water surfaces. The distinction was performed using a land–sea mask. So instead of the original 14 GLCF and 22 GlobCover classes, the CHIMERE land use preprocessor relies on 15 and 23 classes for GLCF and GlobCover, respectively. An example of CHIMERE regridded land use is displayed in Fig. 5.

Table 1. Examples of some domains for which CHIMERE simulations have been performed, with their horizontal resolution, Δx and Δy, their number of vertical levels, n_v and the domain top, p_{top}, in hPa.

Domain description	Purpose	Domain scale	$\Delta x \times \Delta y$	n_v	p_{top}	Reference
North Atlantic	Dust transport	Hemispheric	$1° \times 1°$	15	200	Menut et al. (2009a)
Europe	Operational forecast	Continental	$0.5° \times 0.5°$	8	500	Rouïl et al. (2009)
Europe	Models comparisons	Continental	$25\,\text{km} \times 25\,\text{km}$	9	200	Solazzo et al. (2012b)
North America	Models comparisons	Continental	$36\,\text{km} \times 36\,\text{km}$	9	200	Solazzo et al. (2012b)
France	Operational forecast	National	$0.15° \times 0.1°$	8	500	Rouïl et al. (2009)
Western Europe	Sensitivity study	Continental	$45\,\text{km} \times 45\,\text{km}$	8, 9, 20	500	Menut et al. (2013)
Northern France	Sensitivity study	Regional	$15\,\text{km} \times 15\,\text{km}$	8, 9, 20	500	Menut et al. (2013)
Ile-de-France region	Sensitivity study	Urban area	$5\,\text{km} \times 5\,\text{km}$	8	500	Valari et al. (2011)

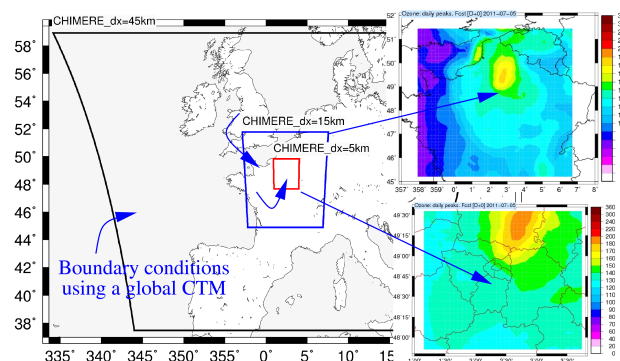**Table 2.** Land use categories used in CHIMERE.

#	Description	#	Description
1	Agricultural land/crops	6	Shrubs
2	Grassland	7	Needleleaf forest
3	Barren land/bare ground	8	Broadleaf forest
4	Inland Water	9	Ocean
5	Urban		

Fig. 6. Example of simulation domains for CHIMERE, and corresponding surface ozone concentrations maps. The largest domain ($dx = 45\,\text{km}$) uses a global model climatology for boundary conditions, and forces itself the medium domain, $dx = 15\,\text{km}$, over the North of France, itself forcing the small domain, $dx = 5\,\text{km}$, over the Paris area.

3.3 Boundary and initial conditions

As a limited area model, CHIMERE requires chemical initial and boundary conditions. The boundary conditions are three-dimensional fields covering the whole simulation period. These fields provide the concentrations of chemical species (gaseous and particulate) at the lateral and upper layers of the CHIMERE simulation domain. Some CTMs use tabulated vertical profiles derived from observational climatologies. Considering that observation-based boundary conditions are too restrictive in terms of available species, i.e. temporal and spatial coverage, CHIMERE gets its boundary conditions from global CTMs. The sensitivity study by Szopa et al. (2009) illustrates the importance of using a domain that is large enough to minimise boundary effects and allow for recirculations within the CHIMERE domain.

To ensure the best possible simulation quality, a common practice is to use the nesting option of CHIMERE, with a coarse domain to provide the most consistent boundary conditions for the smaller nested domains. An example of such a configuration is displayed in Fig. 6 for a specific study in the Paris area with the horizontal resolution $\Delta x = 5\,\text{km}$. The local simulation is nested into a larger domain with $\Delta x = 15\,\text{km}$, which itself is nested into a domain with $\Delta x = 45\,\text{km}$. Only the largest domain makes use of external boundary conditions (Fig. 6).

Szopa et al. (2009) also investigated the sensitivity of the model to the temporal increment of the boundary conditions. They found that using a time-variable large-scale forcing improves the variability at the boundary of the

domain compared to the monthly average, but the magnitude of the sensitivity decreases towards the centre of the domain. Schere et al. (2012) confirmed this finding during the AQMEII inter-comparison exercise. Colette et al. (2011) argued that the selection of the large-scale model had a larger impact than its temporal resolution.

Based on the research projects that have been conducted in the past, preprocessing tools have been implemented to build boundary conditions from a variety of global models. The most widely employed is LMDz-INCA (Folberth et al., 2006), for which a climatology (average monthly fields) is available on the CHIMERE website. Alternatively, the MOZART (Model for OZone And Related chemical Tracers) model was also used, for instance, for the GEMS (Hollingsworth et al., 2008), MACC (Monitoring Atmospheric Composition and Climate) II, and AQMEII (Air Quality Model Evaluation International Initiative)(Rao et al., 2011) projects, and an interface with OsloCTM2 (Sovde et al., 2008) was also developed for the CityZen project. For the specific case of mineral dust, the GOCART (Goddard
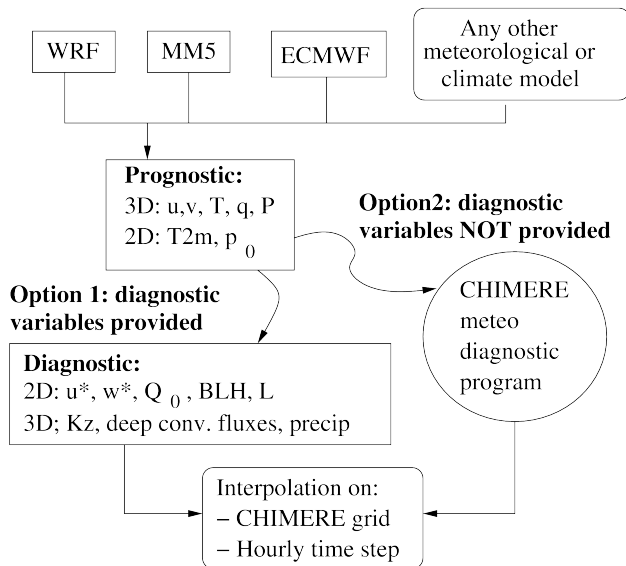
Fig. 7. Treatment of meteorological fields; two options are available: (i) using a meteorological dataset restricted to the mean parameters (u, v, T, q, P, precipitation) and (ii) using a complete meteorological dataset that includes turbulent parameters.

Chemistry Aerosol Radiation and Transport) (Ginoux et al., 2001) monthly average fields are also available. The current version of the model includes in its name list a series of flags in order to define which model is to be used for the following three groups of species: gases, dust aerosols, and non-dust aerosols. For each of them either climatological or time-varying fields can be used.

The initial conditions are included in a three-dimensional field corresponding to the starting date of the simulation. The same global model fields used for boundary conditions can be used to initiate the simulation. If there are no global model fields available, it is also possible to start a simulation with zero concentrations for all species. In this case, the spin-up time of the simulation has to be adjusted to the domain size: from a few days for a local domain to one month for a continental domain (to take into account the long-range transport and possible recirculations).

4   Meteorology

CHIMERE is an off-line chemistry-transport model driven by meteorological fields, e.g. from a weather forecast model, such as WRF or MM5. CHIMERE contains a meteorological preprocessor that prepares standard meteorological variables to be read by the model core.

The input meteorological data are processed in two stages, as presented in Fig. 7. This choice constitutes a strength of the CHIMERE model: the user can use CHIMERE providing only very basic meteorological variables such as wind speed,

temperature, humidity and pressure. In such a case, a complete suite of diagnostic tools for all other mandatory variables (turbulent fluctuations and fluxes) may be used. On the other hand, if the meteorological model provides all the necessary meteorological variables, the meteorological interface only interpolates data on the CHIMERE grid, with an hourly time step. The diagnostic interface may also be used even if turbulent parameters are provided with the meteo model. The user can decide to bypass turbulent parameterisations of the input meteorological model and make use of the CHIMERE diagnostics in order to increase the consistency of the forcing fields across a range of input models.

The meteorological interface first transforms original variables from any input spatial grid and temporal frequency into standard variables on the CHIMERE horizontal grid as hourly values. The operations performed include horizontal and temporal interpolation, wind vector rotation, temporal deaccumulation of precipitations, transformation from perturbation and mean values to full values, etc. The vertical interpolation is performed at a later stage, since a higher vertical resolution might be required for the turbulence and fluxes diagnostics. In the current CHIMERE version 2013, meteorological interfaces are provided for ECMWF (ERA-INTERIM, IFS), WRF (Skamarock et al., 2007) and MM5 models.

If not all required fields are provided, the preprocessor diagnostic model is used. It takes meteorological variables and transforms them into variables necessary for the CHIMERE core. These parameters are (i) the radiation attenuation, (ii) the boundary layer height, (iii) the friction velocity u_*, (iv) the aerodynamical resistance r_a, (v) the sensible heat flux Q_0, (vi) the Monin–Obukhov length L and (vii) the convective velocity w_*.

For the photochemistry, the cloud liquid water content is necessary to estimate the radiative attenuation. If rain water or ice are available, they are added to the cloud water for the attenuation effects. Note that for gaseous species (such as HNO_3) and aerosols calculations, additional parameters related to convective and large-scale precipitation are required for the scavenging.

Finally, and since most large-scale weather models do not include any "urban parameterisation", the possibility of correcting the wind speed in the surface layer (due to increased roughness) in urban areas is offered. This will automatically be balanced by a vertical wind component calculated in the mass balance (see vertical transport below). This correction has however no effect at continental scale where the fraction of urban areas in the model grid cells are limited (see Fig. 5 for example, where the Paris city, an urban site, is not a "dominant" land use for the corresponding cell). This urban parameterisation has however a strong impact on urban versions of the model, mostly for primary pollutants.

4.1 Diagnostic of turbulent parameters

The turbulent parameters may be read from the meteorological driver or diagnosed in CHIMERE, as explained in Fig. 7. In the case of a CHIMERE diagnostic, the following variables are calculated: the friction velocity u_*, the surface sensible heat flux Q_0, the vertical convective velocity w_*, the boundary layer height $\overline{h}$, the bulk Richardson number R_{iB}, the Monin–Obukhov length L, and the vertical diffusivity profile K_z.

The friction velocity u_* is used for the deposition and calculation of diffusivities. It is a particularly sensitive parameter for ozone in summer through the calculation of the aerodynamic resistance r_a. Friction velocity is thus sensitive to the land use type, which is critical to deposition. In large-scale meteorological models, roughness lengths are often too coarse for the implementation of high-resolution deposition. Therefore an update of u_* is proposed following the Louis et al. (1982) formulation, which is particularly robust. We recommend using this alternative formulation, no matter whether u_* is available in the input fields, in order to have a deposition that is consistent with the high-resolution land use.

$$u_* = \sqrt{C_{DN}^2 \, F_m \, |U|^2},$$

(4)

with $|U|$ the mean wind speed at 10 m above ground level, F_m is the Louis et al. (1982) stability function and C_{DN} the momentum transfer coefficient as

$$C_{DN} = \frac{k}{\ln\left(\dfrac{z}{z_{0m}}\right)},$$

(5)

with $k = 0.41$ the Karman constant, z the altitude where the wind speed $|U|$ is known and z_{0m}, the momentum roughness length. The momentum stability function F_m is estimated according to the bulk Richardson number, R_{ib}, value. R_{ib} is estimated at each altitude z as

$$R_{ib}(z) = \frac{g \, z}{\overline{\theta_v(z)}} \frac{\overline{\theta_v(z)} - \overline{\theta_v(z_0)}}{|U(z)|^2},$$

(6)

with $g = 9.81\ \mathrm{m^2\,s^{-2}}$ the gravitational acceleration and θ_v the virtual potential temperature in Kelvin.

– In unstable cases, if $R_{ib} < 0$:

$$F_m = 1 - \frac{2b \, R_{ib}}{1 + 3b \, c \, C_{DN}^2 \cdot \sqrt{\dfrac{z}{z_{0m}}} \sqrt{|R_{ib}|}}.$$

(7)

– In stable cases, if $R_{ib} > 0$:

$$F_m = \frac{1}{1 + \dfrac{2b \, R_{ib}}{\sqrt{1 + d \, R_{ib}}}}$$

(8)

with the constant $b = c = d = 5$. In the neutral case, i.e $R_{ib} = 0$, $F_m = 1$.

The surface sensible heat flux, Q_0, is used to compute w_* and therefore mixing, and the height of the boundary layer. In fact, only the virtual heat flux is required, which can be recomputed from an empirical formula (Priestley, 1949) using temperatures in the first model layers. However, this formula is not very accurate and it is strongly advised to use heat fluxes from the meteorological model, if available. If the surface sensible heat flux Q_0 is provided by the meteorological model, it is directly used for the computation of the convective velocity w_*:

$$w_* = \left(\frac{g \, Q_0 \, \overline{h}}{\rho \, C_p \, \overline{\theta_v}} \right)^{1/3},$$

(9)

where $\overline{h}$ is the convective boundary layer height, C_p the specific heat of air at constant pressure, and $\overline{\theta_v}$ the mean virtual potential temperature in the first model vertical level.

The Monin–Obhukov length is estimated as

$$L = \frac{-\overline{\theta_v} \, u_*^3}{k \, g \, Q_0}.$$

(10)

The boundary layer height ($\overline{h}$) is derived from different formulation, depending on the atmospheric static stability. When stable, i.e when $L > 0$, $\overline{h}$ is estimated as the altitude when the Richardson number reaches a critical number here chosen as $R_{ic} = 0.5$, following Troen and Mahrt (1986).

In unstable situations (i.e. convective), $\overline{h}$ is estimated using a convectively-based boundary layer height calculation. This is based on a simplified and diagnostic version of the approach of Cheinet and Teixeira (2003) which consists in the resolution of the (dry) thermal plume equation with diffusion. The in-plume vertical velocity and buoyancy equations are solved and the boundary layer top is taken as the height where calculated vertical velocity vanishes. Thermals are initiated with a non-zero vertical velocity and potential temperature departure, depending on the turbulence similarity parameters in the surface layer.

Once the depth of the boundary layer is computed, vertical turbulent mixing can be applied by following the K-diffusion framework, which follows the parameterisation of Troen and Mahrt (1986), but without counter-gradient term. In each model column, the diffusivity coefficient profile K_z $(\mathrm{m^2\,s^{-1}})$ is calculated as

$$K_z = k w_s \frac{z}{h} \left(1 - \frac{z}{h} \right)^2$$

(11)

where w_s is a vertical scale given by similar formulas:

– In the stable case (when the surface sensible heat flux is negative)

$$w_s = \frac{u_*}{(1 + 4.7 z / L)}.$$

(12)

– In the unstable case

$$w_s = (u_*^3 + 2.8\,e\,w_*^3)^{1/3} \qquad (13)$$

where $e = \max(0.1, z/\overline{h})$. A minimal K_z is assumed, with a value of $0.01\,\mathrm{m^2\,s^{-1}}$ in the dry boundary layer and $1\,\mathrm{m^2\,s^{-1}}$ in the cloudy boundary layer. K_z is capped to a maximal value of $K_z = 500\,\mathrm{m^2\,s^{-1}}$ to avoid unrealistic mixing. Above the boundary layer, a fixed value of $K_z = 0.1\,\mathrm{m^2\,s^{-1}}$ is prescribed. As for many CTMs considered as numerically diffusive, horizontal turbulent fluxes are not considered.

4.2 Diagnostic of deep convection fluxes

Deep convection occurs when cumulus or cumulonimbus clouds (referred to as convective clouds) are present. These clouds are formed when air masses are unstable, when warm air is at the surface or cold air is transported in upper layers (cold front). High vertical wind speeds are observed, leading to large cloud structures along the vertical direction. On the other hand, when clouds are only due to mechanical forcings (mountains, warm fronts), they are referred to as stratiform clouds and generally exhibit low vertical velocity.

Air masses are quickly mixed in the troposphere when convective instabilities occur under a cloud. To describe this phenomenon, mixing schemes generally consider a cloud (and the whole column including this cloud) and its environment. In the main part of deep convection parameterisations, the hypothesis of a small cloud surface compared to the total studied surface is used.

Under the cloud, updrafts and downdrafts are observed. The updraft originates from air masses lighter than their environment when downdrafts represent the downfall of colder air (often with rain). In the updraft and the downdraft, air may be exchanged between the cloud and its environment. Entrainment refers to the air that flows from the environment into the cloud; detrainment refers to the air that flows from the cloud towards the environment. In order to ensure mass conservation, a compensatory subsidence is observed in the environment.

In CHIMERE, the hourly fluxes of entrainment and detrainment in the updrafts and the downdrafts are estimated during the meteorological diagnostic stage using the Tiedtke scheme (Tiedtke, 1989). This scheme has been implemented in order to compute convective mass fluxes if any convective fluxes are available from the meteorological model coupled with CHIMERE. Work has been done following the study of Olivié et al. (2004) who showed that the fluxes computed offline with this methodology in TM3 give similar fluxes compared to the archived ECMWF ERA40 convective mass fluxes.

The convective mass fluxes are given by

$$
\begin{aligned}
M(z) &= \rho(z)(a_{\mathrm{up}}\,\overline{w_{\mathrm{up}}(z)} + a_{\mathrm{dw}}\,\overline{w_{\mathrm{dw}}(z)}) \\
&= -\rho(z)\,a_{\mathrm{env}}\overline{w_{\mathrm{env}}(z)} \qquad (14)
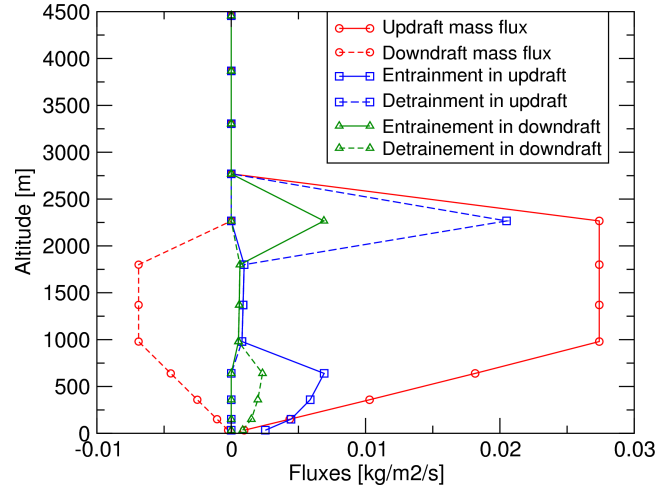\end{aligned}
$$

Fig. 8. Entrainment and detrainment fluxes in the updrafts and downdrafts.

with $\overline{w_{\mathrm{up}}(z)}$, $\overline{w_{\mathrm{dw}}(z)}$ and $\overline{w_{\mathrm{env}}(z)}$ the mean vertical wind speed in the updrafts, downdrafts and environment, respectively. a_{up} and a_{env} are the fractions of coverage area. The vertical gradient of this mass flux is

$$\frac{\partial M(z)}{\partial z}(z) = E(z) - D(z), \qquad (15)$$

with $E(z)$ and $D(z)$ the rates of mass entrained and detrained per unit length ($\mathrm{kg\,m^{-2}\,s^{-1}}$). This equation works both for updrafts and downdrafts; for example, for the updraft

$$
\begin{aligned}
E(z) &= E_{\mathrm{up}}(z) + E_{\mathrm{dw}}(z) \text{ and} \\
D(z) &= D_{\mathrm{up}}(z) + D_{\mathrm{dw}}(z), \qquad (16)
\end{aligned}
$$

Figure 8 shows an example of vertical profile of the convective fluxes, i.e. updraft and downdraft mass fluxes, and entrainment and detrainment fluxes due to the updraft and downdraft mass fluxes. In order to use this convection scheme, new calculations were added to the meteorological preprocessor, providing an estimate of the vertical wind speed (independently of the input from the meteorological model). In the CHIMERE model itself, these fluxes are used to estimate mass fluxes for the pollutant species as follows:

$$
\begin{aligned}
\frac{\partial M_{\mathrm{up}}(z)c_{\mathrm{up}}(z)}{\partial z} &= E_{\mathrm{up}}(z)c_{\mathrm{env}} - D_{\mathrm{up}}(z)c_{\mathrm{up}} \\
\frac{\partial M_{\mathrm{dw}}(z)c_{\mathrm{dw}}(z)}{\partial z} &= E_{\mathrm{dw}}(z)c_{\mathrm{env}} - D_{\mathrm{dw}}(z)c_{\mathrm{dw}} \qquad (17)
\end{aligned}
$$

with the concentrations c_{up}, c_{dw} and c_{env} in the updraft, downdraft and environment, respectively. The calculation is done from surface to the top of the domain in order to ensure mass conservation.

5 Transport and mixing

For a given chemical species with concentration c, the following conservation equation is numerically solved:

$$\partial_t (c\rho) + \partial_i \mathbf{F}^i = 0 \tag{18}$$

with ρ representing the air density and F indicating the mass flux corresponding to velocity $\mathbf{v}$ as

$$\mathbf{F} = \rho c \mathbf{v} \tag{19}$$

As CHIMERE is designed for structured grids where the grid cells are nearly parallelepipedic, this equation can be discretised and solved separately for each of the three orthogonal directions: zonal, meridional and vertical. This strategy is known as operator splitting. Even though the use of operator splitting may generate some numerical problems, this technique is very widely used in weather modelling and chemistry-transport modelling, both because it is more computationally efficient and also sometimes more stable and accurate than a bi- or tri-dimensional approach, particularly when it is applied to high-order models (Byun et al., 1999). Therefore, the tendency c_t in the concentration c is equal to $c_t^{(1)} + c_t^{(2)} + c_t^{(3)}$, where $c_t^{(i)}$ is the time derivative of concentration due to transport in the i-th direction. It is also assumed that the time variations of ρ are much slower than the time variations of c ($|c\rho_t| \ll |\rho c_t|$), so that Eq. (18) becomes

$$\rho c_t^{(i)} = -\partial_i \mathbf{F}^i \tag{20}$$

After time and space discretisation, if we note $\delta^{(i)} c$, the variation of c due to transport in direction i, the discretized transport calculations are the following:

$$\delta^{(i)} c = - \left(\frac{F_{n+\frac{1}{2}}^i(t) - F_{n-\frac{1}{2}}^i(t)}{\Delta x} \right) \Delta t. \tag{21}$$

The concentration increments are calculated successively for each direction from the initial concentration field (parallel strategy). This equation secures mass conservation because the inward and outward fluxes cancel out in each direction. The time integration is of order 1. The key issue in solving this equation is the estimation of the fluxes at the cell interfaces ($F_{n\pm\frac{1}{2}}^i(t)$). The way these fluxes are estimated numerically determines the characteristics of the transport scheme (scheme type and order, diffusivity, numerical stability, etc.).

In chemistry-transport models, various types of numerical schemes have been tested and are proposed to users to solve the advection equations. These numerical schemes range from simple order-1 numerical schemes such as the classical upwind method to higher-order methods such as the piecewise parabolic method (Colella and Woodward, 1984) proposed in CHIMERE and CMAQ, the Yamartino-Blackman cubic scheme proposed in CMAQ (Byun et al., 1999), or the Walcek scheme in BRAMS (Freitas et al., 2011).

5.1 Horizontal transport

In the horizontal directions, it is assumed that the grid cell length does not vary substantially from one grid cell to its neighbours. As in the CHIMERE model, species concentrations and meteorological variables are represented on the same grid, the wind speed at the interfaces is interpolated linearly from the wind speeds at the centres of the two grid cells separated by the interface. The wind speed at the interface will be noted $u_{n\pm\frac{1}{2}}(t)$, and is assumed constant during each coarse time step. In the following we will drop the superscript i to indicate the direction. The definition of the wind speed at the cell interface is independent of the scheme used, so that the definition of the fluxes at the interfaces only depends on the evaluation of the concentration at the interface.

Three horizontal transport schemes are available in the model and described in the next section.

5.1.1 Upwind scheme

In the upwind scheme (Courant et al., 1952), the fluxes at the cell interfaces are defined by the following equations according to the sign of the wind speed at the cell interface:

– If $u_{n+\frac{1}{2}}(t) > 0$

$$F_{n\pm\frac{1}{2}}(t) = c_n \rho_n u_{n+\frac{1}{2}}(t). \tag{22}$$

– If $u_{n+\frac{1}{2}}(t) < 0$

$$F_{n\pm\frac{1}{2}}(t) = c_{n+1} \rho_n u_{n+\frac{1}{2}}(t). \tag{23}$$

The assumption made in this scheme is that the tracer concentration is uniform in each grid cell, so that the mass flux at the interface is the product of the wind at the interface by the tracer concentration in the upwind cell.

5.1.2 Van Leer scheme

The Van Leer scheme used in CHIMERE is commonly called Van Leer I because it is the first one described in the seminal paper of Van Leer (1979). This scheme is of order 2 in space; it assumes that the concentration inside a grid cell is described by a linear slope between the two cell interfaces:

$$c_n(x) = c_n + (x - x_n) \Delta_n \tag{24}$$

where the slope Δ_n is determined according to the following cases. If $c_{n-1} \le c_n \le c_{n+1}$ or $c_{n-1} \ge c_n \ge c_{n+1}$, then

$$\Delta_n = \text{sign}(c_{n+1} - c_{n-1}) \times$$
$$\min \left(\frac{c_{n+1} - c_{n-1}}{2\Delta x}, \frac{c_{n+1} - c_n}{\Delta x}, \frac{c_n - c_{n-1}}{\Delta x} \right) \tag{25}$$

where, in this case, Δ_n is the smallest slope that can be estimated between cell n and its closest neighbours.

Otherwise, c_n is an extremum of concentration and the concentration within cell n is assumed constant ($\Delta_n = 0$), which ensures that the scheme is monotonic.

This scheme, which is recognised in meteorology for its good numerical accuracy and smaller diffusion than the first-order upwind scheme, is also slightly more time-consuming than the first-order upwind scheme. In meteorology, it can be considered as a good compromise solution between numerical accuracy and computational efficiency for long-range transport (Hourdin and Armengaud, 1999).

5.1.3 The piecewise parabolic method scheme

Another scheme that is proposed in CHIMERE for horizontal transport is the 3rd order piecewise parabolic method (PPM) scheme, with slope-limiting and monotonicity-preserving conditions, such as presented in Colella and Woodward (1984). This scheme is applied for each dimension separately, which formally limits the model to 2nd order accuracy in solving the two-dimensional transport problem because the cross derivative $\partial c^2 / \partial x \partial y$ is not taken into account. However, since the scheme is symmetric, it can be considered that the errors due the neglect of cross-derivatives approximately compensate (Ullrich et al., 2010). Therefore, since the treatment of transport in each horizontal dimension has 3rd order accuracy, the PPM scheme as implemented in CHIMERE is much less diffusive than the simple 2nd order Van Leer scheme (see, e.g. Vuolo et al., 2009b).

5.1.4 Comparison between the three available transport schemes

Vuolo et al. (2009b) have performed a comparison between the three horizontal transport schemes presented above in the context of an event of long-range transport of saharian dust over Europe. They found that the choice of one or another of these transport schemes has a strong impact on modelled dust concentrations. As can be expected from the well-known numerical behaviour of these schemes, simulated peak values of the dust plume are reduced by 32 % (upwind) or 17 % (Van Leer) compared to the less diffusive PPM scheme, while the plume area, defined as the surface around the peak where dust concentration exceeds 40 % of the peak value, is increased by 48 % (upwind) or 25 % (Van Leer) compared to the PPM scheme. Horizontal transport schemes also have an indirect impact on vertical transport and diffusion, and the most diffusive horizontal schemes tending to increase dust transport towards the lowest layers, increasing there domain-averaged surface concentrations and decreasing domain-averaged concentrations in and above the boundary layer. The authors conclude that the modelling uncertainty due to the choice of one or another numerical transport scheme is among the limiting factors for the use of dust-transport models for operational air-quality monitoring over Europe.

5.2 Vertical transport

5.2.1 Explicit vertical transport

In the vertical direction, unless otherwise specified by the user, the thickness of the layers increases quasi-exponentially with altitude in order to provide a better vertical resolution in the lower model levels. The value of the thickness ratio between two neighbouring layers is typically close to 1.5. Therefore the hypothesis of constant length for the grid cells cannot be made for vertical transport in CHIMERE, and other numerical schemes have to be used.

First, vertical mass fluxes are calculated to secure zero flux divergence at each grid cell. The vertical mass flux at the lower boundary of the lowest layer is zero, and the vertical mass flux at the top of each grid cell is computed successively, from the lowest layer to the highest.

Once these mass fluxes are known, the vertical transport scheme can be applied. As the number of vertical layers in CHIMERE is much lower than the horizontal size of the domain (typically 8–15 vertical layers), and horizontal domains have typically at least 40×40 grid cells, it is not clear whether using high-order transport schemes relying on the concentration values of several neighbouring cells is useful for vertical transport. Therefore, historically, only the classical upwind scheme was used for vertical transport in CHIMERE, with the same formulation as presented above for horizontal transport.

However, more recent applications concern long-range transport of species having long lifetimes (e.g. mineral dust, volcanic ashes, particulate matter from forest fires) which also can occur above the boundary layer. Therefore, it seems important to reduce numerical diffusion also in the vertical direction. This is particularly important since numerical diffusion reduces the ability of the model to adequately represent dense plumes that are located in thin vertical layers such as mineral dust or volcanic ashes. Therefore, a current development in CHIMERE is to include the Van Leer I transport scheme, which is less diffusive than the upwind scheme, in a version adapted to grid cells with nonuniform thickness. This scheme has been tested with encouraging results in terms of preserving sharp concentration gradients and higher peak values than the upwind scheme during long-range transport and shall therefore be proposed to the community in the next distributed version of CHIMERE.

5.2.2 Turbulent mixing

At each interface between layers k and $k + 1$, an equivalent turbulent vertical velocity w_k is calculated:

$$w_k = \frac{K_z}{\frac{1}{2}(h_k + h_{k+1})}. \tag{26}$$

This allows the net incoming flux at the upper interface of cell k to be diagnosed as

$$F_i = \frac{w_k \left(c_{k+1} \frac{\rho_k}{\rho_{k+1}} - c_k \right)}{h_k}, \tag{27}$$

where c_k is the concentration at the k-th layer, ρ_k the air density, and h_k the thickness of the k-th layer.

The profiles of K_z and w_k are computed in the meteorological diagnostic code at each coarse time step, while the flux for each species, depending on its concentration, is computed at each fine time step (see Sect. 4.1).

6 Emissions

Emissions of pollutants have different origins and include a number of different gaseous and aerosol species, chemically inert or not. The sources can be located at the surface (traffic, biogenic) or along vertical profiles (industrial emissions, biomass burning). These emissions are split into several families representing their origin:

– The anthropogenic emissions include all human activities (traffic, industries, agriculture, among others). They may be very specific and emissions inventories are often dedicated to local scale simulation domain. When operated in the Paris area, CHIMERE uses the AIRPARIF air quality network inventory (Valari and Menut, 2008, 2010). For European studies, the EMEP (European Monitoring and Evaluation Programme) inventory is usually used (Menut et al., 2012), but the TNO (Dutch Organisation for Applied Scientific Research) inventory has also been used (Kuenen et al., 2011). In studies over North America, the model is also used with the US EPA (Environmental Protection Agency) inventory (Solazzo et al., 2012b). Finally, the EDGAR (Emissions Database for Global Atmospheric Research) global emissions inventory was recently added to CHIMERE and comparisons with the EMEP inventory over Europe are ongoing.

– The biogenic emissions represent activities related to the vegetation. These emissions are computed using the global MEGAN (Model of Emissions of Gases and Aerosols from Nature) model (Guenther et al., 2006).

– The mineral dust emissions represent the other part of "natural" emissions, but for non-reactive particle mainly generated by the surface layer dynamics (Menut et al., 2009a). They are specific to several regions (western Africa, Sahel and Saudi Arabia) but are described globally. Some other sources exist in Europe but are not yet implemented and this specific physics (cases of resuspension) is an on-going project in CHIMERE. Such cases are parameterised following the Loosmore and Cederwall, 2004 scheme.
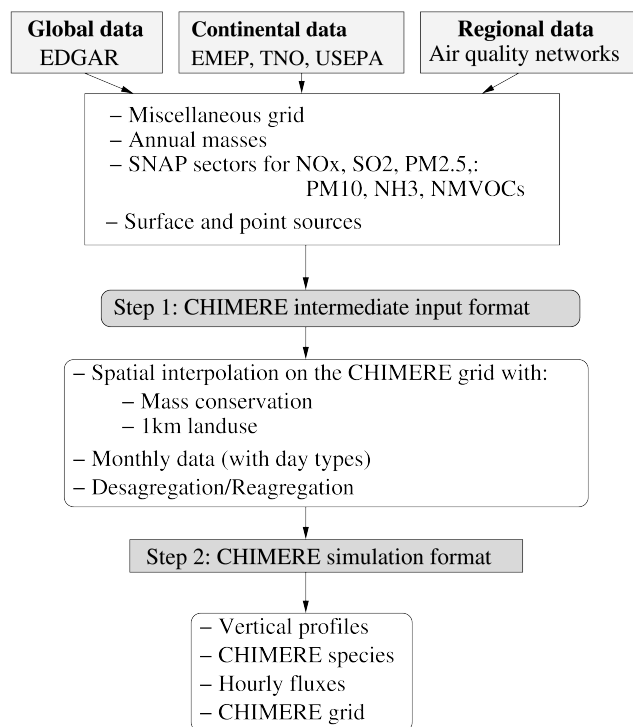

Fig. 9. General principle of the CHIMERE anthropogenic emissions procedure.

– The fire emissions are more sporadic and require numerous and very different data: satellite to estimate the burned area each day, and a vegetation model to estimate the emitted amount for each chemical species (gas and particles). These emissions are also a specific development project in CHIMERE.

6.1 Anthropogenic emissions

Anthropogenic emissions are key in pollution management, since they are the only sources we can reduce. Contrarily to dust and biogenic emissions (only dependent on the surface types and the meteorology), anthropogenic emissions have to be prepared in a bottom-up way, using a number of input data and information to build up an inventory of fluxes of chemical species. These various pieces of input information are generally given for a reduced number of classes of chemical species and are often provided within an activity sectors classification, e.g. following the "Selected Nomenclature for Air Pollutants" (SNAP) nomenclature, which consists of yearly masses per surfaces for various domains and resolutions.

For a realistic simulation, these emissions must be provided every hour for the specific species of the chemical mechanism used and projected over the gridded domain, regardless of the original data projection. From the raw data to the data required for a specific simulation, a sequence of preprocessing actions is necessary, including a temporal

disaggregation, the application of VOC, NO$_x$ and PM shares and the final species lumping into model species. A standard procedure is proposed but preprocessing actions can be bypassed by directly providing hourly anthropogenic emissions. For the standard procedure, it is proposed to prepare these data following two distinct stages, as displayed in Fig. 9:

– Step 1: Create an annual total gridded database per activity sector adapted to the horizontal simulation grid. This then enables creation of monthly masses of emitted model species, already projected onto the horizontal simulation grid, using seasonal factors (provided only for Europe). This step is performed only once each time a new domain is used. The complete suite of programs is provided to the user only for the EMEP format, but can be adapted to other formats.

– Step 2: Disaggregate the monthly emissions into hourly emissions by applying daily and weekly factors, and then produce hourly emission time series for each species adapted to the specific simulation period (real days) and the model vertical grid. This step is performed for each simulation. The complete suite performing this second step is provided to the user and does not need to be modified.

Instead of going through Step 1, the user can also provide monthly anthropogenic emissions files built by other means. Soil NO does not have to be provided for these files, being it is considered as biogenic emissions (even if agricultural activities are anthropogenic). This leads to monthly files for each species and for a typical year. For the MELCHIOR chemical mechanism implemented by default in CHIMERE, emitted species are listed in Table 3.

Depending on the spatial domain, CHIMERE has been used with several anthropogenic emissions datasets. The largest number of studies was over western Europe and two datasets were used: (i) the EMEP database (Vestreng, 2003) and, more recently, the TNO database during the GEMS and MACC projects (Kuenen et al., 2011). These data are spatially interpolated to the model grid. This is performed using an intermediate fine grid with a 1 km resolution (GLCF dataset, Hansen and Reed, 2000). Soil types described on the fine grid allow for a better apportionment of the emissions according to urban, rural, forest, crops and maritime areas. This preprocessing is provided with the model distribution to all users.

The way in which these emissions are estimated could have a strong impact on modelled concentrations. In Menut et al. (2012), a sensitivity study was done to quantify the impact of the temporal profile used to disaggregate emissions mass fluxes. More recently, continental scale modelling was done over the United States and the model used the US EPA inventory to model air quality during the AQMEII project (Rao et al., 2011; Schere et al., 2012; Solazzo et al., 2012b).

Table 3. List of MELCHIOR anthropogenic emitted species.

Model species	Name
NO	Nitrogen monoxide
NO2	Nitrogen dioxide
HONO	Nitrous acid
SO2	Sulphur dioxide
NH3	Ammoniac
CO	Carbon monoxide
CH4	Methane
C2H6	Ethane
NC4H10	n-Butane
C2H4	Ethene
C2H6	Ethane
C3H6	Propene
C5H8	Isoprene
OXYL	o-Xylene
HCHO	Formaldehyde
CH3CHO	Acetaldehyde
CH3COE	Methyl ethyl Ketone
APINEN	α-pinene
PPM_fin	Primary particulate matter
PPM_coa	Primary particulate matter
PPM_big	Primary particulate matter
H2SO4_fin	Primary sulphuric acid
OCAR_fin	Primary organic carbon
BCAR_fin	Primary black carbon (or elemental carbon)

Several other applications were also performed over Mexico City within the framework of the MILAGRO project, (Hodzic et al., 2009).

At a finer scale, CHIMERE is used with more specific anthropogenic emission inventories. This is the case for all studies done over the Paris area using the AIRPARIF air quality network data (from Menut et al., 2000a to Valari et al., 2011). A sensitivity study was presented in Valari and Menut (2008) showing the impact of the emissions horizontal resolution on the modelled concentrations: (i) the effect of spatially "averaged" areas may lead to large changes in the emission fluxes and therefore concentrations; and (ii) due to nonlinearity in chemical regimes, the modelled concentrations do not vary linearly with the NO$_x$ and VOCs emission fluxes changes. As one of the strongest "air pollution hotspots" in Europe, the model is also used to simulate the Po Valley pollution with a specific inventory, as described in de Meij et al. (2009), among others.

Whatever the database and its resolution, the species NO$_x$ and NMVOCs (non-methane volatile organic compounds) have to be distributed in the chemical mechanism species. Annual emissions of NO$_x$ are first speciated as 9.2 % of NO$_2$, 0.8 % of HONO and 90 % of NO, following GENEMIS recommendations (Friedrich, 2000; Kurtenbach et al., 2001; Aumont et al., 2003). Emissions of SO$_x$ are speciated as 99 % of SO$_2$ and 1 % of H$_2$SO$_4$. The GENEMIS NMVOC speciation is used for the same districts and for 6 types of emission

activity sectors: traffic, solvents, industry (except solvents), energy extraction/production, residential (except solvents), and agriculture. For each activity, a speciation is obtained over 32 NMVOC NAPAP (National Acid Precipitation Assessment Program) classes (Middleton et al., 1990). Once the disagregation step is performed, an aggregation step for the lumping of NMVOCs into model species is achieved following Middleton et al. (1990).

For the anthropogenic emissions of primary particles, H_2SO_4, PPM, OCAR, BCAR are split over three modes:

- XXX_fin for diameters $D_p < 2.5\,\mu m$

- XXX_coa for $2.5 < D_p < 10\,\mu m$

- XXX_big for $D_p > 10\,\mu m$.

PPM_fin refers to $PM_{2.5}$, PPM_coa to PM_{10}–$PM_{2.5} \cdot H_2SO_4$, and OCAR, BCAR are assumed to be in the fine mode. In rural areas, NO emissions from ammonium used in fertilizer application, followed by microbiological processes, may be significant. Since these emissions strongly depend on temperature, they are processed in the model as "biogenic" emissions and we refer to them as "biogenic NO emissions". CHIMERE uses a European inventory of soil NO emissions from Stohl et al. (1996). This inventory estimates the soil emission to be of the order of 20 % of the emissions from combustion on a European average, during the summer months, but with large difference between the countries. In the model, these NO emissions are only considered during the months of May to August.

6.2 Biogenic emissions

Emissions of six CHIMERE species – isoprene, α-pinene, β-pinene, limonene, ocimene, and NO – are calculated using the MEGAN model data and parameterisations. The MEGAN model (Guenther et al., 2006, v.2.04) exploits most recent measurements in a gridded and canopy scale approach, which is more appropriate for use in CTMs since it estimates the effective burden of gases that mix and react in the boundary layer. Estimates of biogenic VOCs from vegetation and NO emissions are calculated as

$$ER_i = EF_i \times \gamma_i(T, PPFD, LAI) \times \rho_i, \tag{28}$$

where ER_i ($\mu g\,m^{-2}\,h^{-1}$) is the emission rate of species i, EF_i ($\mu g\,m^{-2}\,h^{-1}$) is an emission factor at canopy standard conditions, γ_i (unitless) is an emission activity factor that accounts for deviations from canopy standard conditions, and ρ_i is a factor that accounts for production/loss within canopy.

As a first step, canopy standard conditions are set as follows: air temperature (T) of 303 K; photosynthetic photon flux density (PPFD) of $1500\,\mu mol\,m^{-2}\,s^{-1}$ at the top of the canopy; leaf area index (LAI) of $5\,m^2\,m^{-2}$; and a canopy with 80 % mature, 10 % growing and 10 % old foliage.

The MEGAN model parameterises the bulk effect of changing environmental conditions using three time-dependent input variables specified at top of the canopy: temperature (T), radiation (PPFD), and foliage density (LAI). The production/loss term within canopy is assumed to be unity ($\rho = 1$). The equation can then be expanded as:

$$ER_i = EF_i \times \gamma_{T,i} \times \gamma_{PPFD} \times \gamma_{LAI}. \tag{29}$$

The MEGAN model provides input EF and LAI data over a global grid, hereafter projected on the CHIMERE model grid. The current available choice for EFs is restricted to following species: isoprene, α-pinene, β-pinene, myrcene, sabinene, limonene, δ^3-carene, ocimene, and nitrogen oxide. NO biogenic emissions include contribution from both forest and agricultural (fertilizers) soils. EFs are static and refer to years 2000–2001. They are obtained summing up over several plant functional types (e.g. broadleaf and needle trees, shrubs, etc. . .). LAI database is given as a monthly mean product derived from MODIS observations, referred to base year 2000. Hourly emissions are calculated using 2 m temperature and short-wave radiation from a meteorological model output. Terpene and humulene emissions are not calculated in this model version and are set to zero.

For European studies with CHIMERE, a comparison of the simulated formaldehyde column was presented in Curci et al. (2010). Formaldehyde concentrations variability is primarily driven by the oxidation of biogenic isoprene over Europe. By comparison to satellite based observations (Aura/OMI), it was shown that MEGAN isoprene emissions might be 40 % and 20 % too high over the Balkans and Southern Germany, respectively, and 20 % too low over Iberian Peninsula, Greece and Italy (Curci et al., 2010).

6.3 Sea salt emissions

In the same way as biogenic emissions, the sea salt emissions calculations need to know the meteorological parameters at an hourly time step and over the whole simulated period and domain. They are calculated by Monahan (1986):

$$\frac{dF}{dr} = 1.373 U_{10}^{3.41} r^{-3} (1 + 0.057 r^{1.05}) 10^{1.19 e^{-B^2}} \tag{30}$$

$$B = \frac{0.38 - \log(r)}{0.65} \tag{31}$$

F is the flux of sea salt particle number expressed in particles $m^{-2}\,s^{-1}\,\mu m^{-1}$, r the particle radius in μm, and U_{10} is the wind speed at 10 m in $m\,s^{-1}$.

6.4 Mineral particles emissions

In this model version, CHIMERE is able to make calculations on regional areas anywhere on Earth. The most important source of particulate matter is mineral dust. In the Northern Hemisphere, mineral dust is mainly emitted in Africa (Sahara and Sahel), when some emissions are also observed
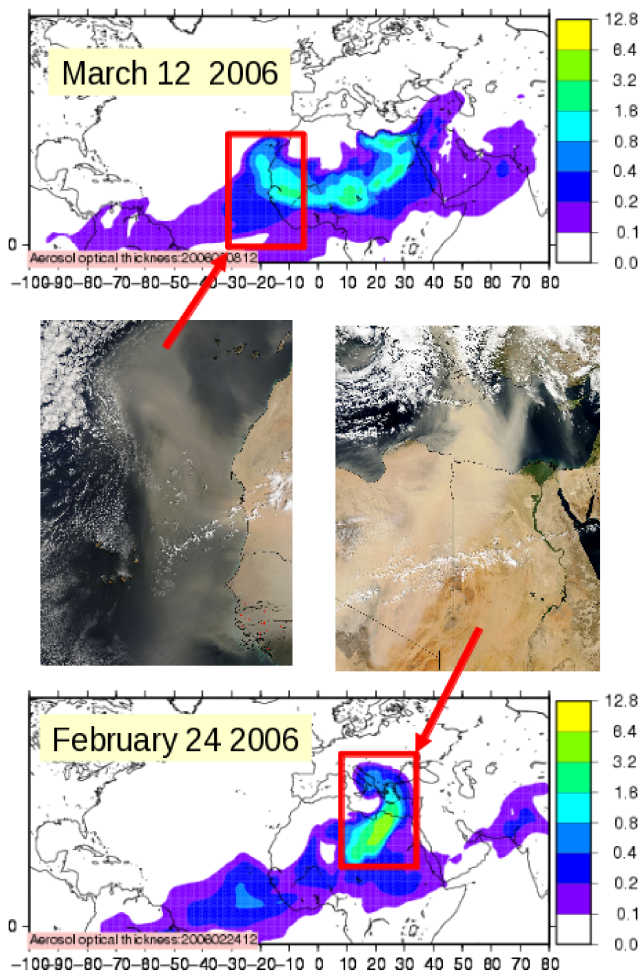
The dust emission fluxes are calculated using the parameterisation of Marticorena and Bergametti (1995) for saltation and the dust production model (DPM) proposed by Alfaro and Gomes (2001) for sandblasting. In order to have a better accuracy and a lower computational cost, the DPM is optimised as presented in Menut et al. (2005b). Before calculating the fluxes, the threshold friction velocity is estimated following the Shao and Lu (2000) scheme. A complete description of the dust calculation is presented in Menut et al. (2007).

For long-range transport simulations, the modelled domain is very large and must include at the same time Africa (for emissions) and Europe (for the long-range transport and deposition). This leads to a coarse horizontal resolution of $1° \times 1°$ in many studies. In order to take into account the sub-grid scale variability of observed winds, the dust emissions are thus estimated using a Weibull distribution for the wind speed, following Cakmur et al. (2004) and Pryor et al. (2005).

An extension of the African dust emission scheme was done for Europe to model a huge dust event in Ukraine (Bessagnet et al., 2008). This shows that it is possible to model local European erosion and retrieve an extreme event of particles, such as those observed in north-western Europe (Netherlands, Belgium).

In Menut (2008), the impact of the meteorological forcing (NCEP or ECMWF) on the dust emission fluxes was quantified. During the studied period, two major dust events were observed. It was shown that the meteorological models are able to diagnose wind speed values high enough to provoke dust saltation for one observed event, and not the other – each model diagnosing one of the two observed events but not the same. This highlights the huge sensitivity of dust emissions to the surface meteorology used. In Vuolo et al. (2009a), the model results were compared to CALIOP lidar data and the vertical diffusion was quantified. In Menut et al. (2009a), an intensive observation period of the AMMA (African Monsoon Multidisciplinary Analysis) program was modelled in forecast mode to study the variability of the predictability of modelled surface dust concentrations. It was shown that the sum of all model uncertainties (emissions, transport, deposition) and of the spread of the forecasted meteorology induces a variability in surface concentrations still higher than the required precision for European air quality forecast. A sensitivity study was presented in Menut et al. (2009b) and it was shown that a very small area in the Sahara (around the position of the former French nuclear tests site during the 60s) may explain the sporadic (but low) radionuclides concentrations measured sometimes in the South of France. Finally, the dust emissions are only calculated using a bottom-up approach and future interesting developments could be to merge these calculations with satellite data to improve the calculated emitted dust flux (as in Huneeus et al., 2012 at the global scale).

Fig. 10. Example of dust plumes observed and simulated for the 24 February and 8 March 2006 with CHIMERE. Satellite images are from NASA/MODIS.

over land such as Europe. These emissions are sporadic but intense. In order to correctly model the total budget of particulate matter, mineral dust emissions are diagnosed in the model. The goal of the mineral dust modelling is twofold: improve our understanding of this physical problem (emissions, transported thin layers) and, after long-range transport, estimate the relative part of mineral dust in the total budget of aerosols near the surface (and thus accounted for air quality in Europe, for example), as displayed for example in Fig. 10.

The calculation of mineral dust emissions is split into two parts: (i) over the western Africa, and (ii) over Europe.

Over western Africa, the analysis and forecast of mineral dust was primarily done in a different branch of CHIMERE called CHIMERE-dust. The developments of the dust emissions and transport are still ongoing but the development of CHIMERE-dust was frozen in 2010 and all dust calculations are now integrated into the current CHIMERE model, ensuring more homogeneous developments.

Over western Europe, the erosion process is less important than over Africa but has to be taken into account for the local budget of air quality. Saltation is not the only natural aerosol upward entrainment process; close to the surface, turbulence induces resuspension of freshly deposited small particles. The extraction results from the imbalance between adhesive and lifting forces. Such particles can originate from the atmosphere or the biosphere, and are particularly easy to extract shortly after deposition (Loosmore and Cederwall, 2004). In order to represent these processes, we use a bulk formulation based on the simple resuspension rate empirical formula of Loosmore and Cederwall, 2004, which was shown to provide a very good fit to the available resuspension measurement data. The particles are first deposited then resuspended. In reality, deposition and resuspension are simultaneous, and the available dust concentration on the ground is governed by resuspension, washout by runoff and absorption by soil water, and production by deposition and other biological or mechanical processes. The detail of all these processes is essentially unknown, and we assume here that the available concentration of dust only depends on the wetness of the surface, as fully described in Vautard et al. (2005). In this empirical view, the resuspension flux is governed by

$$F = P f(w) u_*^{1.43} \tag{32}$$

where $f(w)$ is the soil moisture factor, given by

$$\begin{cases} w < w_t : f_w = 1 \\ w > w_t : f_w = \sqrt{1 + 1.21(100(w - w_t))^{0.68}}, \end{cases}$$

with w the gravimetric soil moisture ($\mathrm{kg\,kg^{-1}}$) and w_t ($\mathrm{kg\,kg^{-1}}$) a threshold gravimetric soil moisture. A uniform value of $0.1\,\mathrm{kg\,kg^{-1}}$ is used, corresponding to a large clay fraction. P is a constant tuned in order to approximately close the PM_{10} mass budget, and the u_* dependency follows the Loosmore and Cederwall (2004) formulation. In absence of any dedicated measurements, the re-entrained PM_{10} particle mass is distributed in a standard atmospheric size distribution: 2/3 of the mass as $PM_{2.5}$ and 1/3 as coarse PM_{10}–$PM_{2.5}$. Within $PM_{2.5}$, particles are distributed in the same three modes as for the anthropogenic emissions.

6.5 Fire emissions

Fires are now recognised to be a major source of emissions of aerosols and trace gases. Depending on the area studied, the species of interest and the time period analysed, it may be necessary to account for this additional contribution in the model simulations. Several studies have used CHIMERE to evaluate the impact of large fire events on air quality at regional scale, for example Hodzic et al. (2007) for fires in Portugal in 2003 or Konovalov et al. (2011) for fires in Russia in 2010. A new emission preprocessor is currently being developed in order to allow the evaluation of emissions either from pre-existing emission inventories (e.g. van der Werf et al.,
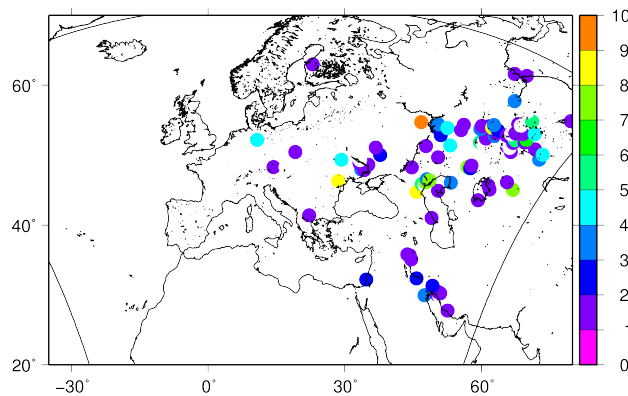

Fig. 11. Example of area burned ($\mathrm{km^2}$) calculated using the fire emissions preprocessor for 8 May 2012 over western Europe.

2010; Wiedinmyer et al., 2011), or from the fire location points and estimated area burned directly. The latter allows the construction of an emission inventory for the CHIMERE grid and time period chosen by the user. It is adaptable to near real-time observations for forecasting purposes.

This inventory is based on the general formulation of Seiler and Crutzen (1980). For each model species i, the emission associated to a specific fire E_i (kg species) is estimated by multiplying the area burned in the corresponding vegetation type A_{veg} ($\mathrm{m^2}$) by the fuel load $\mathrm{FL_{veg}}$ (kg dry matter (DM) $\mathrm{m^{-2}}$) and the specific emission factor $\mathrm{EF}_{i,veg}$ (g (kg DM)$^{-1}$), as summarised in Eq. (33):

$$E_i = \sum_{v=1}^{nveg} \left(A_{veg} \mathrm{FL_{veg}} \mathrm{EF}_{i,veg} \right). \tag{33}$$

The emissions are then binned into the specified model grid. The temporal and horizontal resolutions of the fire emissions depend on the resolution of the different parameters. The area burned parameter is estimated from the global observations of fire activity and areas burned at a daily and 1 km resolution from the MODIS instrument (Giglio et al., 2010), coupled to the SEVIRI/METEOSAT observations (Roberts and Wooster, 2008) for the regions covered (Europe and Africa) to allow the evaluation of a diurnal cycle. An example is presented in Fig. 11 for 8 May 2012. Depending on the fire location, a specific vegetation burned is attributed using the USGS (US Geological Survey) land use database (at 1 km resolution) and the corresponding fuel load (or carbon content) is evaluated from simulations by the ORCHIDEE (Organising Carbon and Hydrology in Dynamic Ecosystems) vegetation and carbon cycle model (Krinner et al., 2005).

Finally, the emissions are converted from carbon (or DM, considering that it is 45 % carbon, as shown in van der Werf et al., 2010) to each species using emission factors from the Akagi et al. (2011) review. Any species may be included in the inventory provided that emission factors are

available. For a full description of each step of the calculation, the reader is referred to Turquety (2012).

In addition to the amount of trace gases and aerosols, the injection altitude is a critical parameter. Indeed, fires can release enough energy to trigger or reinforce convection (Freitas et al., 2007; Rio et al., 2010). These events will be accounted for by using a parameterisation of pyroconvection – still being implemented – to evaluate emission profiles based on the fire intensity and the meteorological conditions (e.g. WRF (Weather Research and Forecasting) simulations used for the CHIMERE simulations). A database including all CHIMERE species will be made available to users via the ECCAD portal (ECCAD, 2013) and the near real-time evaluation of the emissions is on-going at LMD (COSY, 2013). Updates on the availability of the fire emission module will be available from the CHIMERE website.

7 Chemistry

7.1 Chemical preprocessor

The complete chemical mechanism used by CHIMERE is built using a suit of scripts and programs called chemprep. CHIMERE offers the option to include different gas-phase and aerosol chemical mechanisms. The originality in CHIMERE is that these chemical mechanisms are written in ASCII format, and, thus, do not need to be compiled. The user can easily change some reactions or add new ones. When the model is launched, the availability of chemistry input files corresponding to the specific simulation is checked. If the data already exist, the run continues. If not, a preprocessor script will create the data directory. The strength of this approach is that the user may easily create very particular chemical schemes. All chemical parts being independent, the user may choose to have gas chemistry or not, aerosols chemistry or not (and the number of bins), sea salt, dust, secondary organic aerosols, persistent organic pollutants, tracers or not. The nomenclature was defined to be easily understandable and the user can build chemistry sensitivity studies by changing reactions rates, photo dissociation rates, etc. The list of active species may also be changed and chemical families may be defined (e.g. $NO_x = NO + NO_2$), so that they can be dignosed as other tracers.

7.2 Gas-phase chemistry

By default, there exist one aerosol scheme and two versions of the gas-phase scheme. The complete scheme, which is the original scheme of Lattuati (1997), hereafter called MELCHIOR1, describes more than 300 reactions of 80 gaseous species. The hydrocarbon degradation is derived from that of the EMEP gas-phase mechanism (Simpson, 1992), with modifications in particular for low NO_x conditions and NO_x-nitrate chemistry. All rate constants are taken from Atkinson et al. (1997) and De Moore et al. (1994). The photochemical
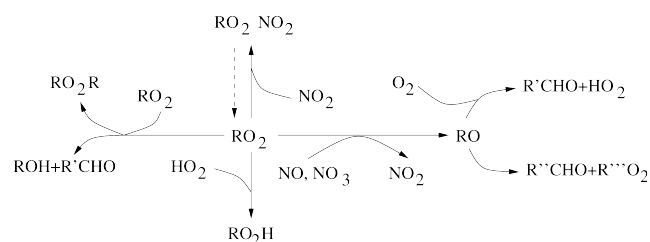
Fig. 12. Reaction pathways of the RO_2 radical in MELCHIOR 1.

reaction rates are regularly updated and the last version follows the Sander et al. (2006) data. Heterogeneous formation of HONO from deposition of NO_2 on wet surfaces is considered, using the formulation of Aumont et al. (2003). For other heterogeneous reactions, see also Sect. 7.3.3.

Inorganic chemistry (42 reactions) is treated in a classical way, similarly to the original EMEP mechanism, including the relevant chemistry of the tropospheric ozone-NO_x-VOC system. Organic chemistry is based on the simplified degradation of 8 hydrocarbons and two alcohols. These compounds represent either individual species, generally for the smallest molecules of a class (methane, ethane, ethene, isoprene and methanol), or families of compounds (*n*-butane for alkanes, propene for alkenes, o-xylene for aromatics, α-pinene for terpenes and ethanol for alcohols). These VOCs undergo oxidation reactions with OH, NO_3, and ozone (the latter only for the unsaturated compounds) leading to the formation of peroxy (RO_2) radicals. All major reaction pathways of the 25 RO_2 radicals (including those formed by the oxidation of carbonyl compounds or nitrates, see below) are represented in the mechanism (Fig. 12):

- Reactions with NO leading to the formation of carbonyl compounds (including, when significant, the fragmentation pathway)

- For some RO_2 + NO reactions, a second pathway yielding nitrates is taken into account

- RO_2 reactions with NO_3, important during night-time, and resulting in the same VOC species than the RO_2 + NO reaction

- RO_2 reactions with NO_2, resulting in the formation of peroxynitrates (including PAN)

- Reaction with HO_2, yielding hydroperoxides. Individual hydroperoxides (15) are taken into account. Their oxidation with OH or by photolysis is treated and yields the carbonyls that also results from the RO_2 + NO reaction.

- Recombination reactions of RO_2 radicals. A full treatment would require the treatment of $1/2(N^2 + N)$ reactions (i.e. 325 for $N = 25$) and would be too time-consuming. This mechanism is simplified by taking

into account only the RO_2 reaction with itself, with the most abundant (CH_3O_2) and the most reactive (CH_3COO_2)RO_2 species. Both the radical terminating and non-terminating recombination pathways are included (101 reactions).

Secondary VOC species formed from these reactions are carbonyl compounds (9), hydroperoxides (15), nitrates (9) and peroxynitrates (4). As the primary VOCs, they can undergo reactions with OH, NO_3 and O_3 in addition to photolysis (only for oxidised VOCs). A 0-D study conducted by Dufour et al. (2009) under low and high NO_x conditions allowed the comparison of formaldehyde yields from 10 organic compounds, simulated by MELCHIOR1 and three reference mechanisms (Master Chemical Mechanism from Saunders et al., 2003, the SAPRC99 (Statewide Air Pollution Research Center) scheme developed by Carter, 2000 and the fully explicit self-generated chemical scheme SGMM (Self Generating Master Mechanism) of Aumont et al., 2005). The results show that MELCHIOR1 simulated yields agree within 20 % with the reference mechanisms. This agreement increases to 5 % in high NO_x conditions for C_2H_6, C_3H_6, CH_3CHO, n-C_4H_{10} and CH_3OH oxidation.

In order to reduce the computing time, a reduced mechanism with somewhat more than 40 species and about 120 reactions is derived from MELCHIOR1 (Derognat et al., 2003). This scheme (MELCHIOR2) is optimised for polluted conditions. The concept of "chemical operators" (Carter, 1990) has been introduced, where RO_2 radicals are treated as virtual species independently of their organic rest R. VOC degradation results in secondary compounds as if the corresponding RO_2 radical reacted with NO. In our scheme, some individual RO_2 radicals are explicitly taken into account (CH_3O_2, $CH_3CO(O_2)$, $C_5H_8(OH)O_2$). As a further reduction step, minor reaction pathways under polluted conditions are neglected. Under polluted and moderately polluted conditions ($NO_x > 100$ ppt), differences between the reduced and the complete mechanism are below 5 % for ozone, below 10 % for NO_x and HO_x, and below 20 % for OH. The full list of species and reactions of MELCHIOR2 are given in Appendix A.

Photolysis rates are calculated under clear sky conditions as a function of height using the Tropospheric Ultraviolet and Visible (TUV) radiation model (Madronich et al., 1998). Clouds are taken into account in a highly parameterised fashion, where clear sky photolysis rates are multiplied throughout model columns by an attenuation coefficient A, depending on the total cloud optical depth (COD). Three options for the calculation of COD are available in CHIMERE, thus allowing a fit to several meteorological forcings. A future version of CHIMERE will include an online version of TUV to take into account hourly variations of aerosols concentrations and their impact of photolysis rates.

A comparison of MECHIOR2 and SAPRC07 (Carter, 2010) for the production of secondary organic gaseous

Table 4. Averaged values, with their standard deviation of the correlation coefficient, the root mean square error and the bias, calculated for the comparison of simulated ozone with EEA AirBase data over Europe for summer 2005, using MELCHIOR2 (left) and SAPRC07 (right).

	MELCHIOR2	SAPRC07
R	0.71 ± 0.08	0.71 ± 0.08
RMSE (ppbv)	13.69 ± 2.14	13.18 ± 2.03
Bias (ppbv)	9.29 ± 2.65	8.19 ± 2.65

species within CHIMERE was recently conducted for Europe over a whole summer season in year 2005, with a resolution of 0.16°. For this purpose, SAPRC07 was implemented in CHIMERE, together with a new aggregation table for anthropogenic emitted species and a specific preprocessing of boundary conditions in order to fit the SAPRC lumped species. Also, an up-to-date photolysis rate table, using recent data from Sander et al. (2006) and IUPAC (2006, http://www.iupac.org/), was provided for both schemes using the most recent version of the TUV model. The results for ozone show quite comparable correlation coefficients, RMSE and bias (see Table 4) with a slight tendency for SAPRC07 to reduce the averaged overestimation of ozone, compared with a set of 1300 EEA (European Economic Area) AirBase measurement stations. A latitude-height cross section of a city plume also showed that the two mechanisms produce similar quantities of HO_x radicals (albeit somewhat lower with SAPRC due to reduced ozone production), the main difference being the speciation of organic nitrogen (approximately 25 % of oxidised NO_x species in both schemes), which is more in favour of PAN species when using MELCHIOR2, while SAPRC produces a larger amount of organic nitrates RNO3 (10 % against 5 % with MELCHIOR2). This may impact the geographical extent of ozone production. The possibility to select either SAPRC07 or MELCHIOR will be offered in the next version of CHIMERE.

7.3 Aerosol module

7.3.1 Aerosols size distribution

CHIMERE contains a sectional aerosol module which includes emitted total primary particulate matter (TPPM), secondary species such as nitrate, sulphate, ammonium, or secondary organic aerosol. In addition, natural dust can be simulated, as well as sea salt aerosols either as passive tracers or as interactive species that are in equilibrium with other ions. The organic matter and elemental carbon can be speciated if their emission inventory is available. In this case, the total primary particulate matter is composed of OCAR + BCAR + PPM, where PPM represents the remaining unspecified part of primary species.

Sulphate is formed by SO_2 oxidation through both gaseous and aqueous phase pathways. Nitric acid is produced in the gas phase by NO_x oxidation. N_2O_5 is converted to nitric acid via heterogeneous pathways by oxidation on aqueous aerosols. Ammonia is a primary emitted base converted to ammonium in the aerosol phase by neutralisation of nitric and sulphuric acids. Ammonia, ammonium, nitrate and sulphate exist in aqueous, gaseous and particulate phases in the model. As an example, in the particulate phase the model species pNH$_3$ represents an equivalent ammonium as the sum of NH_4^+ ion, NH_3 liquid, NH_4NO_3 solid, and other salts consistently with the ISORROPIA thermodynamic equilibrium model (Nenes et al., 1998, see below).

Atmospheric aerosols are represented by their size distributions and chemical compositions (Bessagnet et al., 2005). The sectional representation described by Gelbard and Seinfeld (1980) has been used for the density distribution function. The sectional approach is quite useful for solving the governing equation for multicomponent aerosols. It discretises the density distribution function in a finite number of size sections (Warren, 1986) so that all particles in section l have the same composition and are characterised by their mass-median diameter D_p.

The discretisation of the density distribution function q for a given aerosol component follows Eq. (34):

$$q(x) = \frac{dQ}{dx},$$ (34)

where x is the logarithm of the mass m of the particle ($x = \ln(m)$) and Q is the mass concentration function.

Q_l^k (μg m^{-3}) is the mass concentration of the k-th aerosol component within the size section l. The total mass concentration in the size section l is given by Eq. (35):

$$Q_l = \int_{x_{l-1}}^{x_l} q(x)dx = \sum_k Q_l^k.$$ (35)

The range of the discretised size distribution and the number of size sections (n_b) are both user defined. The default range of the distribution is set to 40 nm–10 μm. A good compromise between numerical accuracy and computational time is $n_b = 8$, as used in the PREV'AIR system, Rouïl et al. (2009), with the following mass-median diameter intervals: $D_p = 0.039, 0.078, 0.156, 0.312, 0.625, 1.25, 2.5, 5, 10\,\mu$m.

7.3.2 Aerosols dynamics

Coagulation

Coagulation is modelled following the classical theory described in Gelbard and Seinfeld (1980). Considering that Q_l^k is the mass concentration of component k in size section l, the mass balance equation for coagulation follows Eq. (36):

$$\left[\frac{dQ_l^k}{dt}\right]_{\mathrm{coag}} = \frac{1}{2}\sum_{i=1}^{l-1}\sum_{j=1}^{l-1}\left[{}^{1a}\beta_{i,j,l}Q_j^k Q_i + {}^{1b}\beta_{i,j,l}Q_i^k Q_j\right]$$
$$\quad - \sum_{i=1}^{l-1}\left[{}^{2a}\beta_{i,l}Q_i Q_l^k - {}^{2b}\beta_{i,l}Q_l Q_i^k\right]$$ (36)
$$\quad - \frac{1}{2}{}^{3}\beta_{l,l}Q_l Q_l^k - Q_l^k\sum_{i=l+1}^{m}{}^{4}\beta_{i,l}Q_i.$$

The sectional coagulation coefficients ${}^{1a}\beta, {}^{1b}\beta, {}^{2a}\beta, {}^{2b}\beta, {}^{3}\beta$ and ${}^{4}\beta$ depend on particle characteristics and meteorological data such as temperature, pressure and turbulence parameters (Fuchs, 1964). For submicronic particles, coagulation is essentially driven by Brownian motions. The four terms on the right-hand side of Eq. (36) represent, respectively: the gain in section l due to coagulation of particles in sections lower than l, the loss in section l due to coagulation of particles in section l with those in sections lower than l, the loss by intrasectional coagulation in section l, and the loss due to coagulation of particles in section l with those in sections higher than l.

Gas–particle conversion

The implementation of the absorption process in CHIMERE is based on Bowman et al. (1997). The absorption flux J (μg m^{-3} s^{-1}) of species onto a monodisperse aerosol is

$$J = \frac{1}{\tau}(G - G_{\mathrm{eq}}),$$ (37)

with G and G_{eq} (μg m^{-3}) the gas phase and equilibrium concentrations, respectively. The characteristic time τ is

$$\tau = \frac{1 + \dfrac{8\lambda}{\alpha D_p}}{2\pi\lambda c D_p N},$$ (38)

with λ (m) the mean free path of air molecules, D_p (m) the diameter of the particles, N (particles m^{-3}) the number concentration, α the accommodation coefficient of the transferred species, and c (m s^{-1}) the mean molecular velocity. For a semi-volatile species k, a mean absorption coefficient H_l^k (s^{-1}) is defined at section l as

$$\left[\frac{dQ_l^k}{dl}\right]_{\mathrm{abso}} = H_l^k Q_l$$ (39)

$$H_l^k = \frac{12\lambda c_k}{\rho_p D_p^2(1 + (8\lambda/\alpha_k D_p))}(G^k - G_{l,\mathrm{eq}}^k)$$ (40)

where ρ_p is the particle density (fixed at 1.5 g cm^{-3} here).

Different absorption modules are implemented in CHIMERE for the inorganic and organic aerosols. For inorganic species (sulphate, nitrate, ammonium), the

equilibrium concentration G_{eq} is calculated using the thermodynamic module ISORROPIA (Nenes et al., 1998). This model also determines the water content of particles. Chloride and sodium can be optionally included but with a significant increase in computational time. The model calculates the thermodynamical equilibrium of the sulphate/nitrate/ammonium/sodium/chloride/water system at a given temperature and relative humidity. The possible species for each phase are the following:

– Gas phase: NH_3, HNO_3, HCl, H_2O.

– Liquid phase: NH_4^+, Na^+, H^+, Cl^-, NO_3^-, SO_4^{2-}, HSO_4^-, OH^-, H_2O, $HNO_{3(aq)}$, $HCl_{(aq)}$, $NH_{3(aq)}$, $H_2SO_{4(aq)}$.

– Solid phase: $(NH_4)_2SO_4$, NH_4HSO_4, $(NH_4)_3H(SO_4)_2$, NH_4NO_3, NH_4Cl, $NaCl$, $NaNO_3$, $NaHSO_4$, Na_2SO_4.

Due to its low vapour pressure, sulphuric acid is assumed to reside completely in the condensed phase. Sodium is always in the liquid or solid phases. The solid–liquid phase transition is solved with ISORROPIA by computing the deliquescence relative humidities (relative humidity at the transition point between the two phases).

Two ways are possible:

– Case 1: Reading a look-up table already prepared using ISORROPIA (and provided with the model input data files).

– Case 2: Using the implemented online coupling of ISORROPIA in CHIMERE.

In Case 1, the calculation can be done by interpolating a pre-calculated look-up table (Table 5). The partitioning coefficient for nitrates, ammonium and the aerosol water content has been calculated for a range of temperatures from 260 to 312 K, relative humidities from 3 % to 99 % and concentration ranges from 10^{-2} to $65\,\mu g\,m^{-3}$. Because of numerical limitations, sodium and chloride are not accounted for in this table. In the case of the active "sea salt" option, the model automatically switches to Case 2.

The use of the look-up table allows for running the model faster, at the expense of accuracy around each deliquescent point. Comparisons with online coupling was done and presented in Hodzic (2005), finding that the use of an online coupling leads to a weak decrease of the mean concentrations (13 % for the nitrates, and no more than 2 % for the sulphates). Ammonium concentrations are slightly increased (1 to 5 %). In absolute values, the differences never exceed $0.5\,\mu g\,m^{-3}$ in average for the nitrates and $0.1\,\mu g\,m^{-3}$ for the sulphates and ammonium. The aerosol water content is slightly decreased (3 to 13 %, 0.1 to $2.8\,\mu g\,m^{-3}$).

For semi-volatile organic species, the equilibrium concentration of the aerosol component k at the size section l ($G_{l,eq}^k$) is related to the particle concentration Q_l^k through a

Table 5. Look-up table used for the calculation of the thermodynamic equilibrium with ISORROPIA. The minimum and maximum values represent the range of the values calculated. Their values are defined to cover a large range of possible meteorological situations. In the case of temperature, relative humidity or concentrations less than the minimum or up to the maximum, the thermodynamic equilibrium is chosen as the value corresponding to the last defined value (minimum or maximum). The increment is defined to ensure a realistic linearity between two consecutive values and for the interpolation. It may be an additive (+) or a multiplicative (×) increment.

Variable	Value		Increment
	Min.	Max.	
Temperature (K)	260	312	+ 2.5
Relative humidity	0.3	0.99	+ 0.05
H_2SO_4, HNO_3, NH_3 ($\mu g\,m^{-3}$)	10^{-2}	65	× 1.5

temperature dependent partition coefficient K^p (in $m^3\,\mu g^{-1}$) (Pankow, 1994):

$$G_{l,eq}^k = \frac{Q_l^k}{OM_l K_k^p} \qquad (41)$$

with OM ($\mu g\,m^{-3}$) the concentration of the absorptive organic material. Considering the thermodynamic equilibrium between the gas and particulate phases, this coefficient is given by

$$K_k^p = \frac{10^{-6}\,RT}{MW_{om}\zeta_k p_k^0} \qquad (42)$$

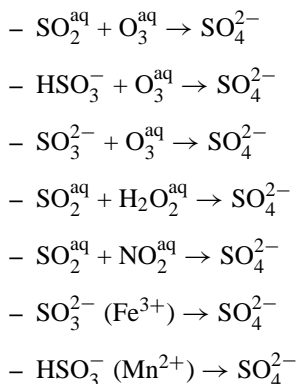with R the ideal gas constant ($8.206 \times 10^{-5}\,m\,atm\,mol^{-1}\,K^{-1}$), T the temperature (K), MW_{om} the mean molecular weight ($g\,mol^{-1}$), p_i^0 the vapour pressure of product i as a pure liquid (atm) and ζ the activity coefficient of species in the bulk aerosol phase. The coefficient ζ is difficult to calculate and is assumed constant and equal to one.

For the nucleation process of sulphuric acid, the parameterisation of Kulmala et al. (1998) is used. This process, favoured by cold humid atmospheric conditions, affects the number of ultrafine particles. The nucleated flux is added to the smallest bin in the sectional distribution. Nucleation of condensable organic species has been clearly identified in many experimental studies (Kavouras et al., 1998; however there is no available parameterisation. Since the sulphuric acid nucleation process competes with absorption processes, the nucleation is expected to occur in low particle polluted conditions.
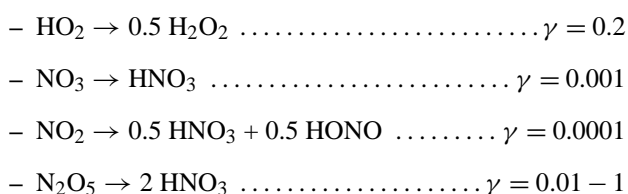
7.3.3 Aerosols chemistry

Multiphase chemistry

Sulphate production in the aqueous phase occurs from the following reactions (Berge, 1993; Hoffmann and Calvert, 1985; Lee and Schwartz, 1983):

– $SO_2^{aq} + O_3^{aq} \rightarrow SO_4^{2-}$

– $HSO_3^- + O_3^{aq} \rightarrow SO_4^{2-}$

– $SO_3^{2-} + O_3^{aq} \rightarrow SO_4^{2-}$

– $SO_2^{aq} + H_2O_2^{aq} \rightarrow SO_4^{2-}$

– $SO_2^{aq} + NO_2^{aq} \rightarrow SO_4^{2-}$

– $SO_3^{2-} (Fe^{3+}) \rightarrow SO_4^{2-}$

– $HSO_3^- (Mn^{2+}) \rightarrow SO_4^{2-}$

SO_2, H_2O_2 and O_3 in the aqueous phase are in equilibrium with the concentrations in the gas phase. Moreover, aqueous SO_2 is dissociated into HSO_3^- and SO_3^{2-}. Catalysed oxidation reactions of sulphur dioxide in aqueous droplets with iron and manganese are considered, following Hoffmann and Calvert (1985), among others. Henry's law coefficient and other aqueous equilibrium constants are used (Seinfeld and Pandis, 1997). Sulphur chemistry is very pH sensitive. The pH is calculated by solving the charge balance equation in the aqueous phase, as described in Bessagnet et al. (2004). To avoid large uncontrolled variations, the pH may vary only between 4.5 and 6.0.

A few heterogeneous reactions are also considered. Nitric acid is produced on existing particles and fog droplets. Although aerosol particles and cloud droplets represent a small fraction of the atmosphere, it is well established that reactions involving gas species on their surfaces may significantly contribute to atmospheric chemistry cycles. For ozone modelling, Jacob (2000) recommends including the following minimal set of reactions:

– $HO_2 \rightarrow 0.5\,H_2O_2$ . . . . $\gamma = 0.2$

– $NO_3 \rightarrow HNO_3$ . . . . $\gamma = 0.001$

– $NO_2 \rightarrow 0.5\,HNO_3 + 0.5\,HONO$ . . . . $\gamma = 0.0001$

– $N_2O_5 \rightarrow 2\,HNO_3$ . . . . $\gamma = 0.01 - 1$

with γ the associated uptake coefficients are provided in Harrison and Kito (1990), and other references in Jacob (2000).

The first-order rate constant k for heterogeneous loss of gases onto particles is given by

$$k = \sum_l \left(\frac{D_p(l)}{2D_g} + \frac{4}{\nu\gamma} \right)^{-1} A_l \qquad (43)$$

with D_p the particle diameter (m), D_g the reacting gas molecular diffusivity ($m^2\,s^{-1}$), ν the mean molecular velocity ($m\,s^{-1}$), A_l the total surface area in the particle bin l, and γ the uptake coefficient of reactive species. The uptake coefficient for N_2O_5 is assumed to be temperature-dependent in the range 0.01–1 (De Moore et al., 1994) with increasing values for decreasing temperatures. Aumont et al. (2003) suggest that NO_2 reactions on wet surfaces could be an important source for HONO production during wintertime smog episodes, which is included in CHIMERE (also present in the gas-phase mechanism; see above).

Secondary organic aerosol chemistry

The complete chemical scheme for SOA formation implemented in CHIMERE includes biogenic and anthropogenic precursors (Table 6), as described in Bessagnet et al. (2009). Biogenic precursors include API (α-pinene and sabinene), BPI (β-pinene and δ^3-carene), LIM (limonene), OCI (myrcene and ocimene) and ISO (isoprene). Anthropogenic precursors include TOL (benzene, toluene and other mono-substituted aromatics), TMB (trimethylbenzene and other poly-substituted aromatics), and NC_4H_{10} (higher alkanes). SOA formation is represented according to a single-step oxidation of the relevant precursors and gas–particle partitioning of the condensable oxidation products. The gas–particle partitioning formulation has been described in detail by Pun et al. (2006). The overall approach consists in differentiating between hydrophilic SOA that are most likely to dissolve into aqueous inorganic particles and hydrophobic SOA that are most likely to absorb into organic particles. The dissolution of hydrophilic SOA is governed by Henry's law whereas the absorption of hydrophobic particles is governed by Raoult's law. The large number of condensable organic compounds is represented by a set of surrogate compounds that cover the range of physico-chemical properties relevant for aerosol formation, i.e. water solubility and acid dissociation for hydrophilic compounds and saturation vapour pressure for hydrophobic compounds. These surrogate compounds were selected by grouping identified particulate-phase molecular products with similar properties. The molecular weight of each surrogate compound is determined based on its structure and functional groups. The Henry's law constant or the saturation vapour pressure of the surrogate species is derived from the average properties of the group. Other properties are estimated using the structure of each surrogate compound. Enthalpy of vaporisation are given in brackets ($kJ\,mol^{-1}$) for each SOA coumpounds: AnA0D (88), AnA1D(88), AnA2D(88), BiA0D(88), BiA1D(88), BiA2D(109), AnBmP(88), AnBlP(88), BiBmP(175). The full name of compounds are explicated in Table 6 caption.

The base SOA module was tested against the smog chamber data of Odum et al. (1997) for anthropogenic compounds and those of Griffin et al. (1999) for biogenic compounds,
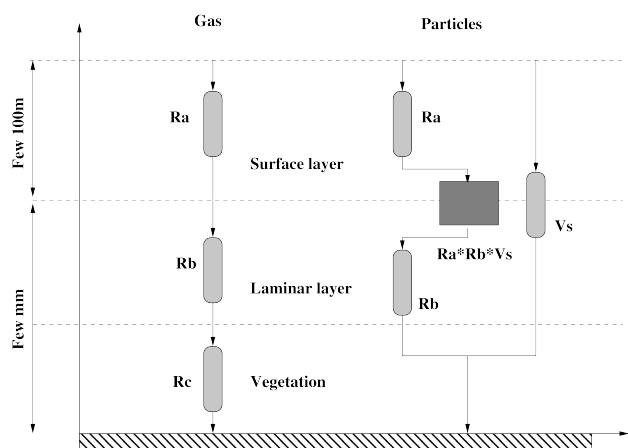
Fig. 13. Main principle of dry deposition for gas and particles. For each model species, three resistances have to be estimated; the deposition is finally done if the sum of all these resistances is low. For particles, the settling velocity is added.

and was shown to satisfactorily reproduce SOA formation for those compounds, (Pun et al., 2006). Higher gaseous alkanes and isoprene were added to the original chemical mechanism of Pun et al. (2006). The formation of SOA from higher alkanes follows the formulation of Zhang et al. (2007) for the stoichiometric SOA yield and it is assumed that the SOA species can be represented by a hydrophobic surrogate compound with a moderate saturation vapour pressure. The formation of SOA from the oxidation of isoprene by hydroxyl radicals is represented with two surrogate products and follows the formulation of Kroll et al. (2006) and zhang2007.

The base SOA module described here was compared with the aerosol mass spectrometer measurements in Mexico City during the MILAGRO-2006 field project (Hodzic et al., 2009), showing a tendency to underpredict the results by 2–8 times the observed levels of SOA in the city as well as at the regional scale downwind of the city. The model has been updated to include the SOA formation from primary organic vapours that has been proposed as an additional and important source of SOA (Robinson et al., 2007), and that has allowed for significant improvement of the comparison with measurements in Mexico City (Hodzic et al., 2010b). Additional constraints from measurements have been included through the calculation of the oxygen to carbon ratios, or non-fossil to fossil carbon amounts (Hodzic et al., 2010a). The code is available upon request.

8 Dry deposition

The dry deposition process is commonly described through a resistance analogy (Wesely, 1989). These resistances are not expressed in the same way considering gas or particles, as displayed in Fig. 13.

The deposition process is a sink and only acts on a concentration c along the vertical:

$$\Delta c = \frac{\partial}{\partial z}(V_d c) \tag{44}$$

with V_d the dry deposition velocity. For each gaseous species or particles, the deposition is due to three different processes. First, the turbulent diffusivity is needed to estimate the aerodynamical resistance r_a. Second, the diffusivity near the ground, in the "laminar" layer, is needed to estimate the surface resistance r_b. Third, for gaseous species only, the species water solubility is needed to estimate the canopy resistance r_c. For particles, there is no solubility; the particle is subject to gravity, falling with a settling velocity v_s. The dry deposition velocity (in $cm\,s^{-1}$) for gaseous species is expressed as

$$v_d = \frac{1}{r_a + r_b + r_c} \tag{45}$$

and for particles as

$$v_d = v_s + \frac{1}{r_a + r_b + r_a r_b v_s} \tag{46}$$

8.1 The resistances

The aerodynamical resistance r_a depends on several turbulent parameters such as L the Monin–Obukhov length, the friction velocity u_*, and the dynamical roughness length z_{0m}.

$$r_a = \frac{1}{k u_*}\left[\ln\left(\frac{z}{z_0}\right) - \Psi_M\left(\frac{z}{L}\right)\right], \tag{47}$$

where Ψ_M is the similarity function accounting for surface layer stability, as defined in Zhang et al. (2001).

The quasi-laminar boundary layer resistance r_b factor is estimated as

$$r_b = \frac{2\nu}{k \times DH_2O_w Pr} DH_2O_g^{2/3}, \tag{48}$$

with k the Karman number (here $k = 0.41$); DH_2O_w and DH_2O_g the molecular diffusivity of water and gaseous species, respectively; and Pr the Prandl number. For gaseous species, the molecular diffusivity is expressed as:

$$DH_2O_g = \sqrt{\frac{dMx}{18}}, \tag{49}$$

with dMx the molar mass of the model species (Table 7). The main land/seasonal parameters follow seasonal variations of resistances. Most land parameters are taken from Wesely (1989), but LAI are drawn from the NASA/EOSDIS Oak Ridge National Laboratory using average LAI field measurements for summer. The molar masses used in CHIMERE are displayed in Table 7.

Table 6. Gas-phase chemical scheme for SOA formation in CHIMERE. The surrogate SOA compounds consist of six hydrophilic species that include an anthropogenic non-dissociative species (AnA0D), an anthropogenic once-dissociative species (AnA1D), an anthropogenic twice-dissociative species (AnA2D), a biogenic non dissociative species (BiA0D), a biogenic once-dissociative species (BiA1D) and a biogenic twice-dissociative species (BiA2D); three hydrophobic species that include an anthropogenic species with moderate saturation vapour pressure (AnBmP), an anthropogenic species with low saturation vapour pressure (AnBlP) and a biogenic species with moderate saturation vapour pressure (BiBmP); and two surrogate compounds for the isoprene oxidation products.

Reactions	kinetic rates (molec $cm^{-3} s^{-1}$)
TOL+OH $\rightarrow 0.004 \times$ AnA0D $+ 0.001 \times$ AnA1D $+ 0.084 \times$ AnBmP $+ 0.013 \times$ AnBlP	$1.81 \times 10^{-12} exp(355/T)$
TMB+OH $\rightarrow 0.002 \times$ AnA0D $+ 0.002 \times$ AnA1D $+ 0.001 \times$ AnA2D $+ 0.088 \times$ AnBmP $+ 0.006 \times$ AnBlP	$9.80 \times 10^{-9}/T$
NC4H10+OH $\rightarrow 0.07 \times$ AnBmP	$1.36 \times 10^{-12} exp(190/T)^{-2}$
API+OH $\rightarrow 0.30 \times$ BiA0D $+ 0.17 \times$ BiA1D $+ 0.10 \times$ BiA2D	$1.21 \times 10^{-11} exp(444/T)$
API+O3 $\rightarrow 0.18 \times$ BiA0D $+ 0.16 \times$ BiA1D $+ 0.05 \times$ BiA2D	$1.01 \times 10^{-15} exp(-732/T)$
API+NO3 $\rightarrow 0.80 \times$ BiBmP	$1.19 \times 10^{-12} exp(490/T)$
BPI+OH $\rightarrow 0.07 \times$ BiA0D $+ 0.08 \times$ BiA1D $+ 0.06 \times$ BiA2D	$2.38 \times 10^{-11} exp(357/T)$
BPI+O3 $\rightarrow 0.09 \times$ BiA0D $+ 0.13 \times$ BiA1D $+ 0.04 \times$ BiA2D	1.50×10^{-17}
BPI+NO3 $\rightarrow 0.80 \times$ BiBmP	2.51×10^{-12}
LIM+OH $\rightarrow 0.20 \times$ BiA0D $+ 0.25 \times$ BiA1D $+ 0.005 \times$ BiA2D	1.71×10^{-10}
LIM+O3 $\rightarrow 0.09 \times$ BiA0D $+ 0.10 \times$ BiA1D	2×10^{-16}
OCI+OH $\rightarrow 0.70 \times$ BiA0D $+ 0.075 \times$ BiA1D	$5.10 \times ^{-8}/T$
OCI+O3 $\rightarrow 0.50 \times$ BiA0D $+ 0.055 \times$ BiA1D	$7.50 \times 10^{-14}/T$
OCI+NO3 $\rightarrow 0.70 \times$ BiA0D $+ 0.075 \times$ BiA1D	$4.30 \times 10^{-9}/T$
ISO+OH $\rightarrow 0.232 \times$ ISOPA1 $+ 0.0288 \times$ ISOPA2	$2.55 \times 10^{-11} exp(410/T)$

Table 7. The main characteristics of the dry deposited species with their names: dMx the molar mass of the model species, dHx the effective Henry's law constant (M atm^{-1}) for the gas, and df0 the normalised (0 to 1) reactivity factor for the dissolved gas.

Species	dMx	dHx	df0
O_3	48	0.01	1
SO_2	64	1×10^5	0
NO_2	46	0.01	0.1
NO	30	2×10^{-3}	0
NH_3	17	1×10^5	0

The formulation of the surface resistance r_c follows Erisman et al. (1994). It uses a number of different other resistances accounting mainly for stomatal and surface processes, which are again dependent on the land use type and season. Necessary chemical parameters for the calculation of r_c are also taken from Erisman et al. (1994) except for carbonyls (Sander et al., 1999; Baer and Nester, 1992) and peroxide species (Hall et al., 1999); dHx and df0, presented in Table 7, are used for the mesophyllic resistance value, as described in Seinfeld and Pandis, 1997). The mesophyllic resistance r_m is calculated for each deposited species as

$$r_m = \frac{1}{dHx \times 3.310^{-4} + df0 \times 10^2} \quad (50)$$

with dHx the effective Henry's law constant (M atm^{-1}) for the gas and df0 the normalised (0 to 1) reactivity factor for the dissolved gas (values are displayed in Table 7). For vegetal canopies, corrections have been implemented according to Zhang et al. (2001), Giorgi (1986) and Peters and Eiden (1992).

8.2 Settling velocity v_s

The settling velocity represents the effect of gravity on particles. This velocity is expressed as

$$v_s = \frac{1}{18} \frac{D_p^2 \rho_p g C_c}{\mu} \quad (51)$$

with ρ_p the particle density (chosen as $\rho_p = 2.65$ g cm^{-3} for mineral dust), D_p the mean mass median diameter of particles, and C_c a slip correction factor accounting for the non-continuum effects when D_p becomes smaller and of the same order of magnitude than the mean free path of air λ, (Seinfeld and Pandis, 1997). g is the gravitational acceleration with $g = 9.81$ m s^{-2}, μ the dynamic viscosity (here the air dynamic viscosity is set to $\mu_{air} = 1.8 \times 10^{-5}$ kg $m^{-1} s^{-1}$). The slip correction factor C_c is estimated as

$$C_c = 1 + \frac{2\lambda}{D_p}\left[1.257 + 0.4 \exp\left(-\frac{1.1 D_p}{2\lambda}\right)\right] \quad (52)$$

with λ the mean free path of air, estimated as

$$\lambda = \frac{2\mu_{air}}{p\sqrt{\frac{8 M_{air}}{\pi R T}}} \quad (53)$$

where M_{air} the molecular mass of dry air (here 28.8 g mol^{-1}), T the temperature (K), p the pressure (Pa), μ the air dynamic viscosity and R the universal gas constant.

9 Impact of clouds

The clouds may impact the photolysis, the chemistry via dissolution of gases in precipitating drops and wet scavenging.

9.1 Impact of clouds on photolysis

In this model version and only for the photolysis attenuation, clouds are assumed to lie above the model top, so that there is no cloud albedo effect within the model domain depth. For all photolysed species, clear sky photolysis rates $J_c(z)$ are multiplied throughout model columns by an attenuation coefficient $A(d)$ depending on the total cloud optical depth (COD) d. Using the TUV model, and a large set of CODs for clouds at various altitudes, the attenuation relative to the clear-sky case has been fitted as a function of COD with the formula

$$A(d) = e^{-0.11 d^{2/3}} \tag{54}$$

Several options are offered in order to calculate the COD. Total COD, d, is the sum of partial CODs from three cloud layers: low clouds d_l, medium clouds d_m, and high clouds d_h. The limits between these clouds are user-chosen, but depend on the meteorological model. For WRF or MM5, limits of 2000 m and 6000 m are proposed. At the end, the model uses the COD estimated for the related model vertical level. For each cloud layer, three options are possible for the calculation of the partial cloud optical depth. If the liquid and ice water content are available in the input meteorological fields, we recommend to use the first option.

- Calculation as a function of liquid/ice water content in the column; assuming sphericity, equivalent droplet size of 6 microns and hexagonal shape for ice particles, the formula for cloud optical depth is 180 C_w + 67 C_i, where C_w and C_i are respectively the liquid water column (in kg m^{-2}) and ice column for this cloud layer.

- Another choice is a parameterisation using relative humidity only. It consists in parameterising the COD as a function of the integral **R**, over the cloud depth, of the relative humidity above 75 %. It is assumed that small cloud formation (in particular cumulus clouds) starts at 75 % relative humidity. Normalisation of **R** leads to the formulation (for instance, for low clouds) $d_l = aR/dz$, where $a = 0.02$ is chosen such that a 1000 m thick layer has an optical cloud depth of 20.

- An even simpler parameterisation can be achieved by making the COD simply proportional to the cloud fraction (if available) for each cloud layer. Coefficient tuning led to proportionality coefficients of 50 for low-clouds, 10 for medium clouds and 2 for high clouds.

This means, for instance, that a sky covered with 100 % of high clouds has an optical depth of 2. Tuning was performed with ECMWF cloud fraction data and should change with the meteorological model.

9.2 Wet scavenging

Scavenging for gas/aerosols in clouds or rain droplets is taken into account as follows:

- For gases in clouds: nitric acid and ammonia in the gas phase are scavenged by cloud droplets and this process is assumed to be reversible. During cloud dissipation, and for a non-precipitating cloud, dissolved gases may reappear in the gas phase (Bessagnet et al., 2004). For a gas denoted A and the processes between gas and aqueous phases, there are two simultaneous reactions occurring:

$$A^g \rightarrow^{k+} A^{aq}; A^g \leftarrow^{k-} A^{aq} \tag{55}$$
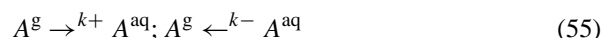
The constants k^- and k^+ (s^{-1}) are estimated following the relations

$$k^- = \frac{6 w_l \rho_a}{\rho_e D} \left(\frac{D}{2 D_A^g} + \frac{4}{c_A \alpha_A} \right)^{-1} \tag{56}$$

$$k^+ = \frac{600}{R H_A T} \left(\frac{D}{2 D_A^g} + \frac{4}{c_A \alpha_A} \right)^{-1}, \tag{57}$$

with ρ_e and ρ_a the water and air densities, respectively, in kg m^{-3}, w_l the liquid water content (kg kg^{-1}), D the droplet mean diameter (m), c_A the mean molecular velocity of the gas A (m s^{-1}), D^g the molecular diffusion of the gas A in air (in m^2 s^{-1}) and α_A the gas A accomodation coefficient. H is the Henry's constant (M atm^{-1}), T the air temperature (K) and R the molar gas constant.

- For gases in rain droplets below the clouds: dissolution of gases in precipitating drops is assumed to be irreversible, both for HNO$_3$ and NH$_3$. The scavenging coefficient is expressed as

$$\Gamma = \frac{p D_g}{6.10^5 u_g D^2} (2 + 0.6 R_e^{1/2} S_c^{1/3}), \tag{58}$$

p being the precipitation rate (mm h^{-1}), D_g the molecular diffusion coefficient (m^2 s^{-1}), u_g the raindrop velocity (m s^{-1}), and Re and Sc respectively the Reynolds and Schmidt numbers of drops. Mircea and Stefan (1998) and references therein give relationships between u_g and hydrometeor diameter for various types of precipitation.

– For particles in clouds: particles can be scavenged either by coagulation with cloud droplets or by precipitating drops. Particles also act as cloud condensation nuclei to form new droplets. This latter process of nucleation is the most efficient one in clouds. According to Tsyro (2002) and Guelle et al. (1998), the deposition flux, Q, is written as

$$\left[\frac{\mathrm{d}Q_l^k}{\mathrm{d}t}\right] = -\frac{\epsilon_l P_{\mathrm{r}}}{w_l h} Q_l^k, \qquad (59)$$

where P_{r} is the precipitation rate released in the grid cell ($\mathrm{g\,cm^{-2}\,s^{-1}}$); w_l the liquid water content ($\mathrm{g\,cm^{-3}}$); h the cell thickness (cm); and ϵ an empirical uptake coefficient (in the range 0–1), depending on particle composition. l and k are respectively the bin and composition subscripts.

– For particles in rain droplets below the clouds: particles are scavenged by raining drops, the deposition flux of particles being

$$\left[\frac{\mathrm{d}Q_l^k}{\mathrm{d}t}\right] = -\frac{\alpha p E_l}{u_g} Q_l^k, \qquad (60)$$

with α is an empirical coefficient, p the precipitation rate in the grid cell ($\mathrm{g\,cm^{-2}\,s^{-1}}$), E a collision efficiency coefficient between particles and raining drops (Slinn, 1983 and u_g the falling drop velocity ($\mathrm{cm\,s^{-1}}$)). Assuming a constant drop diameter (2 mm), this parameterisation is an approximation of equations described in Seinfeld and Pandis (1997) and Jung et al. (2002).

10   Model results evaluation

CHIMERE integrates a large set of complex processes and delivers chemical concentrations. These chemical concentrations have to be compared to available measurements in order to (i) understand complex and non-linear processes and investigate geophysical hypotheses, (ii) validate the model for specific chemical species and location against measurements and therefore estimate the realism of the parameterisations in the model, and (iii) make sensitivity and scenario studies in order to quantify changes in emissions or meteorology under climate change, etc.

For all these reasons, the comparisons between modelled concentrations and measurements were always carefully performed during the various stages of the model developments. These comparisons were carried out with three different options:

– Improve the processes
The comparisons to field campaigns measurements allow for an assessment of the model's ability to reproduce specific air quality episodes using a wide range of available measurements;

– Dynamic evaluation
Long-term simulations can be used to evaluate the sensitivity of the model to changing situations (i.e. monthly variability, seasonal cycles, long-term trends in emissions);

– Compare to other numerical tools
Model inter-comparison exercises allow for comparing the performances of the model with respect to other state-of-the-art models and developing ensemble approaches.

10.1   International projects

Table 8 summarises some of the international projects where CHIMERE has been involved. Some of them include large-scale field campaigns, with data measurements during intensive observations periods used to understand pollution events for the model's development and its validation. Many other national projects (French, Spanish, Italian, etc.) were conducted during the last years and are not listed here.

Some of these projects include field campaigns comprised of a wide range of measurements during selected pollution events. The measurements are limited in space (a region) and time (several days) but they include a larger set of physical and chemical parameters than basic monitoring networks.

The first field campaign using CHIMERE was ESQUIF during the summers 1998 and 1999. In this first version, the model was a box model: five boxes with a central one representing the city Paris and only two vertical levels (the surface and the boundary layer) (Menut et al., 2000a). Even though that model version was very simple, the model was used in forecast mode and was of great help in choosing the best periods to launch the intensive observation periods (IOPs), more particularly for airborne measurements, (Menut et al., 2000b; Vautard et al., 2003). During ESQUIF, the relative part of local ozone production and long-range transport was quantified and it was shown that Paris pollution episodes cannot be above the legal limits with local production only. For the first time, the predicted aerosol chemical and optical properties were evaluated against chemically speciated aerosol data and lidar measurements (Hodzic et al., 2006b). In 2001, CHIMERE was also used for forecast and analysis during the ESCOMPTE campaign that was also devoted to photo-oxidant pollution (ozone) but in the Marseille area in southern France (Menut et al., 2005a). Between ESQUIF and ESCOMPTE, the horizontal grid became cartesian (Schmidt et al., 2001) and covered the lower troposphere with 8 levels.

For the GEMS project, the model was spatially extended to the whole of western Europe, switching the anthropogenic source to the EMEP emissions. These emissions have been changed for the MACC project and the TNO inventory was implemented (Zyryanov et al., 2012).

In 2006, mineral dust emissions and transport were added to the model and used during the AMMA campaign. The model was used in forecast mode and the predictability of

mineral dust emissions was quantified, (Menut et al., 2009a). The model version with gaseous and aerosols species was used during several projects, such as MILAGRO over the Mexico area (Hodzic et al., 2009, 2010b,a; Hodzic and Jimenez, 2011); MEGAPOLI over the Paris area (Royer et al., 2011), EC4MACS for the climate and air pollution mitigation strategies in Europe, and AQMEII for model inter-comparisons between the United States and Europe (Pirovano et al., 2012). More recently, two European projects have had new developments: the CIRCE project where the first online coupling between chemistry and vegetation was done between CHIMERE and ORCHIDEE, and ATOPICA for the development of a new module for the pollen modelling.

10.2 Evaluation in extreme events

Air quality simulations are particularly relevant during extreme events in order to anticipate potentially detrimental situations. CHIMERE was used to simulate air quality in several such events. It was shown to accurately reproduce observed ozone concentrations during the 2003 European heatwave (Vautard et al., 2005) and transport of aerosol smoke plumes (Hodzic et al., 2007) across Europe during this 2003 heatwave. The extreme particulate matter episode that took place in Germany earlier in 2003 was also simulated but with less success by CHIMERE as well as other models (Stern et al., 2008).

In 2008, an unexpected event of high particulate matter concentrations at the surface was observed in Belgium and Netherlands. First thought to be long-range transport of mineral dust from Africa, these huge concentrations were finally identified as coming from Ukraine. This assessment was achieved by including a new dust mineral source representing the erodible Chernozemic soil. The validation was done with surface (AirBase) and space-borne lidar (Caliop) measurements, (Bessagnet et al., 2008).

CHIMERE was used to simulate the transport of the plume of the extreme fire incident that occurred in the Buncefield oil depot in late 2005 (Vautard et al., 2007). It was shown in particular that the lack of major air quality degradation was due to the dispersion and transport of the enormous plume of particulate matter above the boundary layer. More recently, the dispersion of the Eyjafjallajökull volcanic plume in April 2010 was modelled by adding a volcanic source in Iceland. This source was roughly estimated to deliver a near real-time assessment of the ash plume dispersion, which was validated against monitoring stations and lidar remote sensing (Colette et al., 2011a).

10.3 Long-term evaluation

The long-term evaluation of a model is probably the oldest way to estimate its accuracy during pollution events; not only should the model be able to simulate specific and huge pollution events, it also has to accurately calculate low concentrations in absence of pollution.

For a CTM, the air quality networks are able to continuously deliver hourly concentrations of O_3, NO_2 and particulate matter over the past decades. Depending on the model domain and resolution, CHIMERE results have been compared to surface data. Enjoying the increase of computational capabilities, these comparisons have evolved from a few surface dataset to complete hourly validation over several years. The first comparisons were done for a few days and over a limited region in the Paris area (Menut et al., 2000b) to a full year (Hodzic et al., 2004, 2005), then a few months and over larger domains: for example, in Spain (Vivanco et al., 2008) and western Europe (Colette et al., 2011b; Wilson et al., 2012). In Europe, the AirBase network is used in many studies to compare CHIMERE results to surface observations of O_3, NO_2, SO_2, PM_{10}, $PM_{2.5}$. To extend the comparison to vertical profiles, several data types were used: for ozone, vertical profiles of sondes and ozone analyser aboard commercial aircraft (MOZAIC/IAGOS) were compared to model outputs, (Coman et al., 2012; Zyryanov et al., 2012).

Satellite data have also been used for long-term evaluation studies, as listed in Table 9. CHIMERE has been compared to NO_2 satellite observations (tropospheric columns) from SCIAMACHY (Blond et al., 2007), OMI (Huijnen et al., 2010) and GOME (Konovalov et al., 2005). CHIMERE has also been evaluated against AOD measurements from MODIS and POLDER satellites (Hodzic et al., 2006c, 2007).

Satellite ozone observations from satellite and AQ models can now be used synergistically either to evaluate models, to interpret satellite observations or to constrain models through assimilation. In this way, Konovalov et al. (2006) used SCIAMACHY NO_2 columns to optimise NO_x surface emissions. Zyryanov et al. (2012) have evaluated CHIMERE and MACC AQ models against IASI 0–6 km ozone columns over one summer. Coman et al. (2012) have recently shown it is possible to use IASI observations to correct the CHIMERE model using an assimilation approach. Dufour et al. (2009) and Curci et al. (2010) applied inverse modelling of formaldehyde columns (SCIAMACHY and OMI, respectively) to estimate and validate biogenic VOC emissions at the European scale.

10.4 Models inter-comparisons and ensembles

CHIMERE has been involved and tested in a number of inter-comparison studies with other air pollution models. In order to evaluate the sensitivity of air quality to emission control scenarios and their uncertainty, several models were evaluated over a reference year and then used with emission scenarios. This work was conducted within the framework of the Clean Air For Europe program (Cuvelier et al., 2007; Thunis et al., 2007) over four European cities. The evaluation part of the project (Vautard et al., 2007) showed the large spread of model simulations for ozone close to the sources

Table 8. International projects involving CHIMERE (in chronological order). Names with an * correspond to field campaigns for which meteorological and chemical data were used to validate CHIMERE.

Project	Main goals (+references)	Model improvement
ESQUIF*	Regional photochemistry (Paris area, France) – Menut et al. (2000b), Vautard et al. (2003), Hodzic et al. (2006c)	Regional modelling of aerosol and gaseous pollutants, and aerosol optical properties
ESCOMPTE*	Regional photochemistry (Marseille area, France) – Menut et al. (2005a)	Regional cartesian mesh model, for gaseous pollutants only
GEMS, MACC	Monitoring Atmospheric composition and climate – Hollingsworth et al. (2008)	European cartesian mesh model
AMMA*	Mineral dust (western Africa) – Menut et al. (2009a)	Mineral dust addition
MILAGRO*	Regional pollution (Mexico City) – Hodzic et al. (2010b), Hodzic and Jimenez (2011)	Secondary organic aerosols
CIRCE	Climate change and impact research: The Mediterranean Environment – Curci et al. (2009), Bessagnet et al. (2008)	Feedbacks between ozone and vegetation. Implementation of MEGAN.
GEOMON	Global Earth Observation and Monitoring	Pollution trends over Europe
MEGAPOLI*	Regional pollution (Paris area) – Royer et al. (2011)	Fast chemistry and aerosols over the Paris area
EC4MACS	European Consortium for Modelling Air Pollution and Climate Strategies – www.ec4macs.eu	Emissions reduction scenarios
AQMEII	Models inter-comparisons over Europe and United-States – Pirovano et al. (2012), Solazzo et al. (2012b)	US domain
CITYZEN	Impact of megacities on air pollution, trends analysis Colette et al. (2011b)	Emission mapping
ATOPICA	Atopic diseases in changing climate, land use and air quality	Pollens addition in the model

Table 9. Satellite data used for model/data comparisons and analysis.

Satellite	Parameter	Goal
SCIAMACHY, OMI, GOME	NO_2, HCHO	Improve total column and biogenic emissions
MODIS, POLDER	Surface properties	Fires emissions calculation. Improve aerosol emissions and transport
IASI	O_3, CO	Improve the tropospheric columns and vertical distribution
CALIOP	Dust, aerosols	Improve the vertical transport

due to combined effects of titration and poor representation of lower-layer mixing in stable boundary layers. This spread gave rise to a spread of response to emission control scenarios (Thunis et al., 2007). At continental scale, this spread was less marked (Van Loon et al., 2007). In this inter-comparison over Europe, CHIMERE was found to have among the best skills for ozone daily maxima but to overestimate night-time ozone concentration, leading to a general positive bias not generally shared by other models. This bias is thought to be due in large part to overestimation of mixing in stable conditions. For particulate matter, CHIMERE was shown to exhibit a negative bias, shared by other models, at least over several high wintertime episodes in Germany (Stern et al., 2008). Such biases were also found in a more recent and extensive inter-comparison over two continents and a full evaluation year (Rao et al., 2011; Solazzo et al., 2012a,b). In this unprecedented exercise, models used in Europe and in North America were considered. CHIMERE also participated to the first multi-model decadal air quality assessment in the CityZen project (Colette et al., 2011b) and proved to be in-line with other state-of-the-art tools. The same biases as previously reported (positive for mean ozone and negative for particulate matter) where obtained by the majority of the models. As far as CHIMERE was concerned, the usual strength in capturing ozone variability through a good temporal correlation was found.

In these inter-comparison studies, the potential to use these ensemble of models to (i) improve the simulation of air pollutant concentrations by a proper averaging of results and (ii) to estimate the uncertainty in the simulations was evaluated (Solazzo et al., 2012b). It was shown in particular that the average of model results outperformed each individual model result (Van Loon et al., 2007), and that for most pollutants the spread of models was representative of their uncertainty and skill (Vautard et al., 2009).
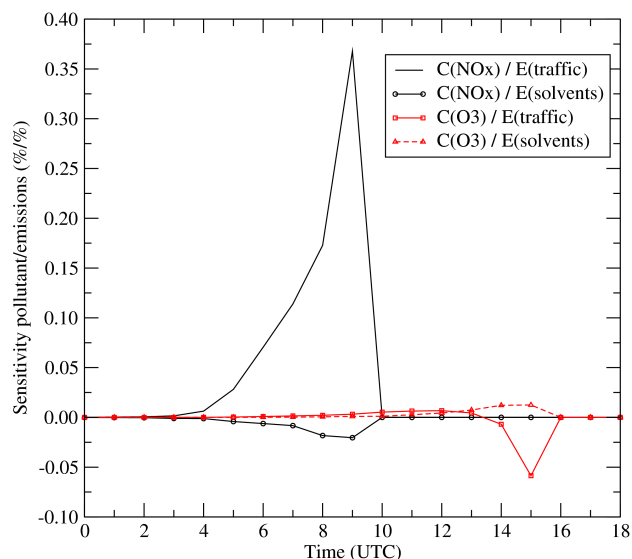
Fig. 14. Time series of the sensitivity of pollutants (NO_x and O_3) to anthropogenic surface emissions (from "traffic" and "solvents" activity sectors).
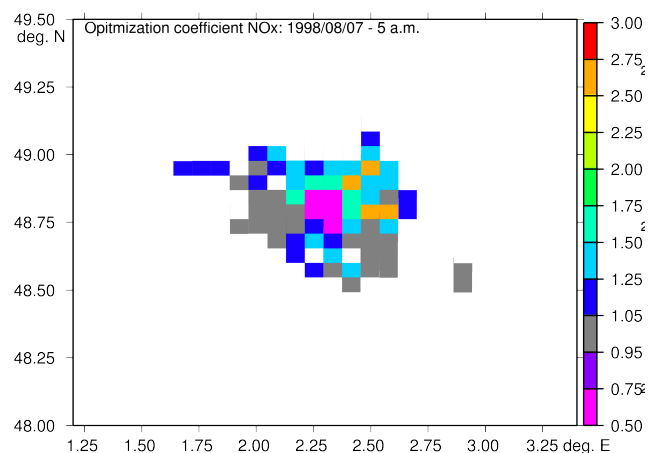

Fig. 15. Inverse modelling of the NO emissions in the Paris area for 7 August 1998 (ESQUIF campaign). The results are multiplicative factors to apply to the emissions flux hour by hour. A value of 1 means there is no change to apply to the fluxes, when, for example, a value of 0.5 means it is needed to divide by two the NO emissions fluxes to reduce the differences between the measured and modelled surface concentrations of NO_x.

11 Data assimilation

The forward chemistry-transport model uses meteorology and emissions as forcings to calculate pollutant concentrations fields. The hybridisation consists in assimilating observations during a simulation in order to (i) optimise one of the forcing parameter (inverse modelling) and (ii) build more realistic concentrations fields (data assimilation analysis).

11.1 Sensitivity studies

For several of the mentionned applications, the adjoint model is a powerful tool and may be used for sensitivity studies and inverse modelling. The first adjoint of CHIMERE was developed in 1998 and used to optimise the boundary conditions of the box-model version (Vautard et al., 2000; Menut et al., 2000a). An updated version was developed when CHIMERE was modified to use a cartesian mesh (Menut, 2003). With CHIMERE being updated every year, the adjoint model should have followed the same evolution; unfortunately, the last adjoint version was the one developed for the gaseous species. When the aerosols were added (Bessagnet et al., 2004), the adjoint part was not upgraded. Currently, a new branch of the model's adjoint is under development: the version applied to regional CO_2 fluxes inversion over western Europe (Broquet et al., 2011) is being parallelised.

The adjoint model was used to quantify to which input parameter the modelled concentrations are sensitive (Menut, 2003). The studies done with CHIMERE were for pollution in the Paris area; the calculations were performed to calculate the sensitivity of O_3, O_x and NO_x to various meteorological parameters and surface emissions fluxes (per activity sectors). An example of synthesised results is presented in Fig. 14. For one specific concentration (here NO_x at 09:00 UTC and O_3 at 15:00 UTC in the Paris centre grid cell), the adjoint model enables calculation of sensitivity to the whole domain of traffic and solvents emissions calculated. This shows that NO_x is more sensitive to emissions than O_3, quantifying the direct effect of modelling primary and secondary species. The sensitivity may be positive (a direct addition of NO_x by traffic emissions will increase instantaneously NO concentrations) or negative (O_3 titration by NO_2). This kind of study allowed for us to classify the most important parameters in a chemistry-transport model, depending on the modelled pollutants, the location and the time.

Another way to conduct sensitivity studies is to use Monte Carlo modelling. The same pollution events were studied over the Paris area. The results allowed for us to quantify the variability of pollutants and thus to refine the uncertainty of the modelled concentrations as a function of the uncertainties of the input parameters (Deguillaume et al., 2008).

11.2 Inverse modelling of emission fluxes

Over the Paris area, the inversion of anthropogenic emissions was done for specific pollution events and seasonal simulations. These studies were an opportunity to develop a new approach. The surface measurements used are less numerous than the grid points to invert; this weak-constrained problem is often circumvented at the global scale by inverting the emissions of the same species as the measured one and considering large areas and long timescale. For regional studies

and photo-oxidant pollution, the time and spatial variability is large. A methodology of dynamical areas was therefore developed and applied (Pison et al., 2006, 2007). For the Paris area, the results enabled us to optimise the diurnal profiles of the emissions and show that the city centre emissions were over-estimated in emission inventories whereas the suburban emissions were often underestimated. An example of optimised coefficients is displayed in Fig. 15 for NO emissions at 05:00 UTC, when traffic becomes an important factor.

11.3 Analysis of concentration fields

Following the approach developed in meteorology and oceanography, data assimilation has been applied to air quality since the beginning of this century. In the case of ozone, ground-based observations from air quality networks have been used to correct regional CTMs (Hanea et al., 2004; Wu et al., 2008). In the case of the CHIMERE model, Blond et al. (2003) and Blond and Vautard (2004) have developed an optimal interpolation method where they used an anisotropic statistical interpolation approach to determine a climatological background covariance matrix (Blond et al., 2003). This matrix allows them to give weights to innovations (differences between model and observations) and to propagate this information where no observations are directly available. Over a European domain they improve RMSE by about 30 %. As already stated by Elbern and Schmidt (2001), forecasts using these analyses as initial conditions were only slightly improved in few particular cases. The work of Blond and Vautard (2004) has been implemented in the PREV'AIR platform that produces operationally ozone analysis (Honoré et al., 2008). Such analyses are also produced within the framework of the FP7/MACC-II project as well as PM$_{10}$ analysis derived from a similar approach (http://www.gmes-atmosphere.eu/services/raq/).

Since 2006, an ensemble Kalman filter (EnKF; Evensen, 1994) has been coupled to the CHIMERE model. It is also a sequential assimilation method but it allows calculating a time-evolutive background covariance matrix that takes into account the variability of model errors with time and space. It is based on a Monte Carlo approach using an ensemble of forward simulations to calculate the background covariance matrix. To do so, we have followed the precursor work of Hanea et al. (2004) that coupled an EnKF to the LOTOS-EUROS model. One of our goals was to assimilate satellite data that would complement surface observations. Indeed, since 2006, the IASI instrument on board the METOP platform (Clerbaux et al., 2009) allows for us to observe ozone concentrations in the lower atmosphere (0–6 km partial columns) with good accuracy (Eremenko et al., 2008; Dufour et al., 2012). Coman et al. (2012) have shown that assimilating IASI 0–6 km columns in the CHIMERE model allows correcting significantly tropospheric ozone fields; see Fig. 16. Corrections were higher at about 3–4 km height where the instrument and retrieval method exhibit maximum sensitivity. In spite of a
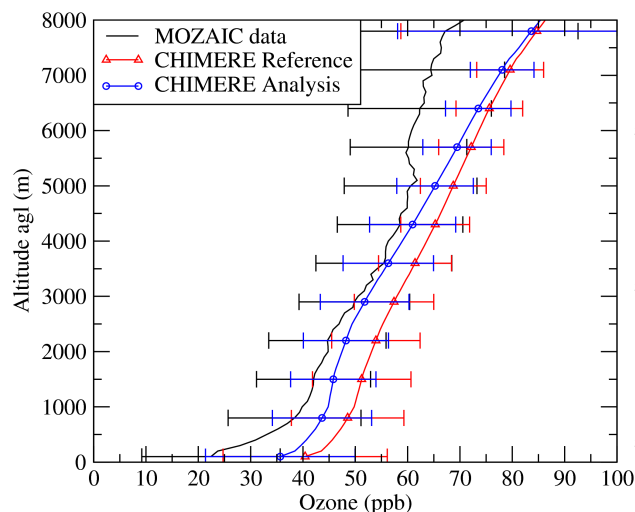
Fig. 16. Assimilation with CHIMERE of ozone profiles recorded by the IASI instrument and comparisons of the obtained gain with MOZAIC data (Data courtesy of A. Coman).

reduced sensitivity of the instrument in the planetary boundary layer, Coman et al. (2012) also showed that surface ozone fields were systematically improved.

In the near future, it is planned to produce analyses by assimilating simultaneously surface and satellite measurements of ozone. Such a product could be of great interest to study tropospheric ozone variability and trends, especially in regions where in situ observations are scarce such as the Mediterranean basin. This CHIMERE-EnKF software will be tested operationally during the FP7/MACC-II project. Moreover, assimilation of other species such as NO$_2$ and CO (from satellite) is planned within the framework of the same MACC-II project.

12 Forecasts

Air quality forecasting is a main goal of chemistry-transport modelling, and also a specific way to improve and to validate models (Menut and Bessagnet, 2010). Indeed, forecasting makes it possible to quantify day by day the model accuracy and to measure its sensitivity to the various parameters and parameterisations.

12.1 Experimental forecasts

Since its early developments, CHIMERE has been used both for analysis and forecasting. For the release of every new model version, the development priorities were driven by the results of test case analyses and daily experimental forecasts. A recent example of this is the COSY project which aims at producing systematic comparisons between observations and a set of CHIMERE forecasts and making them available on a website (www.lmd.polytechnique.fr/cosy/). This project
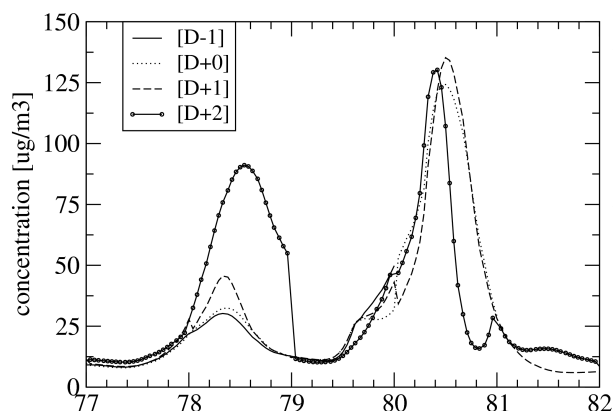
Fig. 17. Time series of dust forecast for the period of 17 to 23 March 2006. The results are for dust surface concentrations in Rome, Italy.

has provided sensitivity analyses of modelled concentration fields when using the different land surface schemes of the WRF meteorological driver (Khvorostyanov et al., 2010); this leads to a better understanding of the impact of land surface models (LSM) on modelled surface concentrations and thus quantifying the concentration biases only due to meteorological surface fluxes. Another example comes from dust modelling. Figure 17 presents modelled dust surface concentrations over Rome, Italy, for several leads of the same period (Menut et al., 2009a). The variability of the meteorological forecast directly impacts the emissions and, ultimately, the remote surface concentrations; the daily forecasted maxima may show differences up to a factor of 2. Unfortunately, this variability is of the same order of magnitude as the background particle concentrations often recorded in Europe and thus clearly shows that the forecast of mineral dust transport over Europe remains a challenging scientific problem.

12.2 Operational forecasts

CHIMERE is implemented on several air quality platforms which provide daily forecasts up to 3 days ahead for a set of regulatory pollutants (e.g. O_3, NO_2, PM_{10}, $PM_{2.5}$). Initially developed as experimental platforms, such tools (www.prevair.org; Rouïl et al., 2009; Menut and Bessagnet, 2010) became operational in France after the 2003 summer heatwave (Vautard et al., 2005) and are foreseen to be operational throughout western Europe at the end of the FP7 project MACCII in 2014. Forecasts of pollution above accepted threshold levels are essential for public health information.

Moreover, air quality models offer two essential functionalities. They can help to identify the reasons why pollutant concentrations increase (giving for instance PM speciation), and the results of operational runs conducted with emission control scenarios allow selecting the most efficient measures.

As a consequence, these modelling tools provide support to national authorities on air quality management, and they assist the selection of regulatory measures that may be efficient in limiting the intensity of pollution episodes. In this context, CHIMERE is now involved in the prototype toolbox dedicated to air quality episode management in the MACC-II project.

Another contribution of such platforms to air quality issues is the provision of daily assessments of the model's ability to predict pollutant concentrations. Daily scores are indeed an important parameter, which gives insights into the research efforts that need to be made to improve the model behaviour. Current research efforts are thus focusing on the implementation of dynamical input data such as biomass burning emissions (Kaiser et al., 2012) or emissions from agricultural activities (Hamaoui-Laguel et al., 2012). In both cases, the starting date of emissions is crucial for forecasting their impacts in time, place and magnitude on pollutant concentrations. The wintertime PM episodes forecasts are also improved by taken into account the variability of climatic conditions when calculating the wood burning emissions from residential heating.

Finally, in the MACC-II project, it was shown that import of pollutants due to cross-Atlantic ozone plumes or African dust plumes could contribute significantly to the European pollutant levels computed with CHIMERE (Menut et al., 2009b), and that the implementation in CHIMERE of near real-time boundary conditions delivered by global models provided reliable pollutant background concentrations to the European regional domains. Currently, CHIMERE forecasts are used by more than 50 local agencies in Europe, either to refine the PREV'AIR forecasts using their own modelling platform or to produce a local air quality index value (such as the CITEAIR index, http://www.airqualitynow.eu).

13 Specific applications

13.1 Chemistry in fire plumes

Quantifying the impact of fires on air quality requires not only accurate emissions but also a realistic representation of the chemical processes occurring inside the plumes.

Fire plumes, besides having high spatial variability, consist of large amounts of trace gases (including the main ozone precursors) and aerosols.

The corresponding emissions are included in the emission inventory. However, these dense plumes will induce a significant modification of the UV light reaching the surface, and thereby the photolysis rates for photochemical reactions. For example, Alvarado and Prinn (2009) estimate that, if this effect is accounted for, the ozone levels in plumes from savanna fires in South Africa decrease by 10–20 %, and Hodzic et al. (2007) estimate a 10–30 % decrease for Portuguese forest fires.
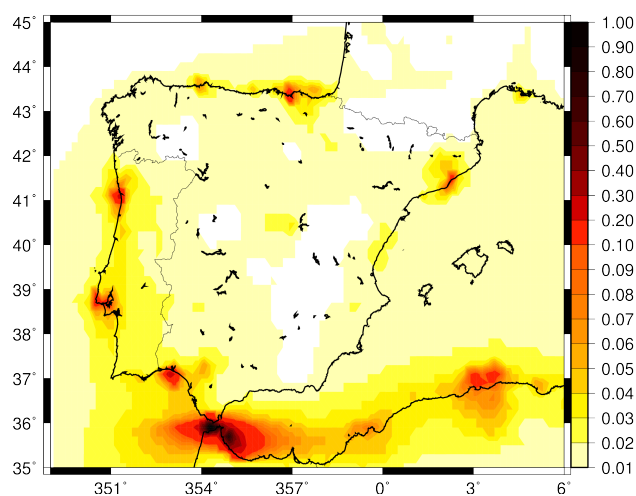
Fig. 18. Mean annual concentrations of lead ($\mu g\,m^{-3}$) for 2009 over Spain and Portugal.

CHIMERE currently uses tabulated photolysis rates pre-calculated using the Troposphere Ultraviolet and Visible (TUV) model (Madronich et al., 1998 for different cloud cover situations. In order to account for the impact of dense plumes (critical for fires but also dust and anthropogenic sources), the photolysis rates need to be re-evaluated depending on the evolution of the aerosol optical depth (AOD) at different vertical levels and locations. Several approaches have been used for CHIMERE. A simplified parameterisation based on satellite observations of the AOD has been used by Hodzic et al. (2007), and Konovalov et al. (2011) have refined this approach by recalculating the photolysis rates online with the TUV model using the observed AOD as a constraint. More recently, an online calculation of the aerosol properties has been implemented and coupled to the TUV model (Péré et al., 2011). It is currently being integrated into the standard version of CHIMERE, with a numerical optimisation of the calculation of aerosol optical properties to maintain computational efficiency. Large variations in ozone production are also observed, depending on PAN formation, heterogeneous chemistry or oxygenated volatile organic compounds amounts for different fire situations (Jaffe and Wigder, 2012; Konovalov et al., 2012), which are still not well represented by CTMs. Once the effect of aerosols on radiation is included, further analysis will be undertaken on the chemical evolution in fire plumes simulated by CHIMERE.

13.2 Heavy metals

Metals are considered as important pollutants that can be responsible for a range of human health effects. Diseases such as cancer, neurotoxicity, immunotoxicity, cardiotoxicity, reproductive toxicity, teratogenesis and genotoxicity can be related with the presence of metal particles in the air

(HEI, 1998; EPA, 1999). Organisms can assimilate the particles via inhalation (because particles settle into bronchial regions of the lungs) or ingestion (because the particles are deposited on and accumulated within soils or water, and this accumulation produces an increase of risk of future exposure through food). In Europe, Directive 2008/50/CE sets an annual limit value of $500\,ng\,m^{-3}$ for Pb. Annual target levels for As, Cd and Ni are regulated by Directive 2004/107/CE ($6\,ng\,m^{-3}$ for As, $5\,ng\,m^{-3}$ for Cd, $20\,ng\,m^{-3}$ for Ni). For other metals (with the exception of mercury), no normative is available.

In the atmosphere, metals are attached to particles, especially those in the fine fraction (Milford and Davidson, 1985; Allen et al., 2001; Molnar et al., 1995; Kuloglu and Tuncel, 2005). A preliminary description of heavy metals (Pb, Cd, As, Ni, Cu, Zn, Cr and Se) air concentration has been implemented in a dedicated version of the CHIMERE model. At this stage, these metals are treated as inert fine particles. According to Finlayson-Pitts and Pitts (2000), the aerodynamic mass median diameters for Pb, Cd, As, Ni, Cu, Zn, Cr and Se are 0.55, 0.84, 1.11, 0.98, 1.29,1.13, 1.11 and 4.39 μm, respectively. As in this approach all the metals are considered as fine particles, more refinement could be necessary for Se. Physical processes such as anthropogenic emissions, transport, mixing and deposition are considered. For some of these metals, such as Pb and Cd, the inert status consideration is generally adopted. They are believed to be transported in the atmosphere with no change in their chemical and aggregate state (Ryaboshapko et al., 1999). For other metals this approach must be reconsidered and reactions in the aqueous phase could be required. In the case of Cr, Seigneur and Constantinou (1995) have highlighted the importance of the reactions converting Cr(III) to Cr(VI) and vice-versa associated to particle and droplet chemistry. For Ni, aqueous phase chemistry could also be important. Regarding arsenic, airborne particulate matter has been shown to contain both inorganic and organic arsenic compounds (Johnson and Braman, 1975; Attrep and Anirudhan, 1977).

A preliminary study applying this heavy metal CHIMERE version has been presented in Vivanco et al. (2011), where the model performance was evaluated for Spain. Figure 18 presents the mean annual concentrations of lead for 2009. This preliminary version has also recently been applied for a European domain at a horizontal resolution of 0.2° for 2008 (González et al., 2012). Important limitations were set for metal emissions. Only anthropogenic sources have been considered, although some metals can be released into the environment by both natural sources and human activities. Moreover, only Cd and Pb emissions are available in the EMEP expert database for 2008 (Vestreng et al., 2009); for the other metals, emissions were taken from TNO totals estimated for 2000 (Van der Gon et al., 2005), except in the Spanish part of the domain where emissions were provided by the Spanish Ministry of Environment and Rural and Marine Affairs for 2006. Original emissions were spatially and temporally
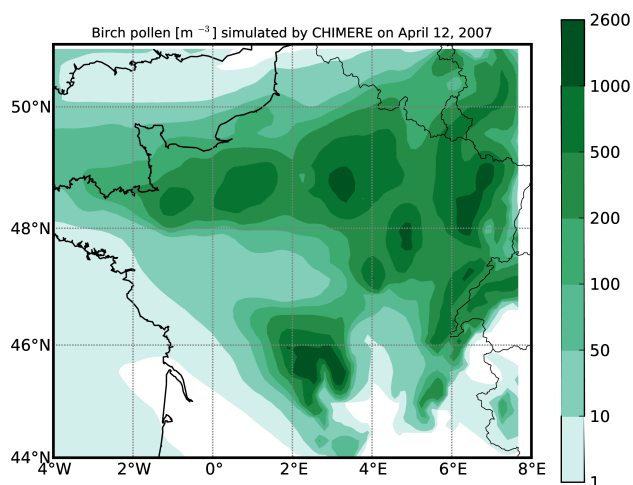
Fig. 19. Birch pollen concentrations (grains m^{-3}) simulated with CHIMERE for 12 April 2007.

disaggregated and adapted to the simulated domain by taking into account the land use information of GLCF (Global Land Cover Facility, http://change.gsfc.nasa.gov/create.html). In the case of TNO emissions, only the total amount for each EMEP grid cell was available. The temporal disaggregation of these totals is normally performed in the CHIMERE emission processor considering the SNAP activity. As we did not have this information for the metals coming from the TNO database, we used a SNAP disaggregation similar to PM$_{2.5}$ particles for those species. We also used a temporal profile similar to PM fine particles. Better knowledge of the temporal behaviour of metal emissions for each SNAP activity would reduce the input errors. Other aspects, such as boundary conditions, should also be considered in order to improve model results. At this stage, no boundary conditions were applied, as no information on many of these metals is available from global models.

13.3 Pollens

A new research direction involving CHIMERE is modelling the dispersion of pollen grains in the atmosphere. The prevalence of pollen allergy in European countries is estimated between 12 to more than 35 % (Burney et al., 1996). The quantity of some highly allergenic pollens, such as ragweed, is increasing and seems to correlate with allergic diseases (Rybnicek and Jaeger, 2001). Conclusions from a number of European and international climate research projects suggest that future climate change and variability may strongly affect pollen emission and dispersal in Europe (Christensen et al., 2007), thereby influencing the prevalence of atopic diseases.

The European (FP7) project Atopica aims to evaluate, using numerical modelling, statistical data analysis and laboratory experiments, the influence of changes in climate, air

quality, land use, and the subsequent distribution of invasive allergenic plant species and allergic pollen distribution on human health. Modelling of ragweed and birch pollen emission and dispersion in the atmosphere using CHIMERE plays a key role in this project.

Pollen grains are about 5–50 times larger in size than conventional atmospheric aerosols. The scale analysis (Sofiev et al., 2006) shows that the assumption of pollen grains being transported together with air masses following the airflow, including small turbulent eddies, still applies. Pollens are implemented in CHIMERE as a special aerosol type having a single size distribution bin of 20–22 µm, depending on the pollen type. The density is prescribed for a particular pollen species and varies between 800 and 1050 kg m^{-3}, which yields the sedimentation velocity of 1.2–1.3 cm s^{-1}. Gravitational settling is the main deposition process for pollens and the only one considered in the model. The simulated pollen grains are transported by the atmospheric circulation and turbulent mixing, settled by gravity, and washed out by rains and clouds, following the parameterisations already implemented for other CHIMERE aerosols.

The main challenge for state-of-the art pollen dispersion modelling is accurate description of pollen emissions. This requires a fair knowledge of plant distribution, phenology, and adequate assumptions regarding the sensitivity to meteorological factors, such as humidity, temperature, wind and turbulence. Unlike industrial pollutants or mineral aerosols, pollen emissions depend not only on the instantaneous meteorological conditions but also on the conditions during the pollen maturation within the plants before the pollination starts. Additional factors such as the CO$_2$ and O$_3$ concentrations can influence pollen production and emissions (Rogers et al., 2006; Darbah et al., 2008).

Pollen episodes have been simulated with CHIMERE for ragweed (Chaxel et al., 2012) and for birch, the latter using the emission methodology developed by Sofiev et al. (2013). Figure 19 shows daily mean birch pollen concentration simulated with CHIMERE for 12 April 2007, during the seasonal concentration maximum in Paris. CHIMERE was forced by the WRF model in the forecast mode without nudging at 15 km resolution for the North of France. The model concentration in Paris that year peaks at 390 grains m^{-3} on 12 April, while the RNSA observations show the peak of 965 grains m^{-3} on 14 April. The model underestimation can be related to the birch distribution map used for pollen emission calculation: its French contribution is mostly based on the satellite data prone to large uncertainties (Sofiev et al., 2006).

13.4 Sub-grid scale exposure modelling for health impact assessment

Air quality models, by integrating different emission scenarios, are valuable tools for the evaluation of alternative mitigation policies and possible adaptation strategies with

respect to public health and climate change. The CHIMERE model is involved in two different projects on the evaluation of the health impact of air quality under changing conditions (ACHIA and ACCEPTED). This ongoing research requires several model developments in order to account for the variability of exposure at the intra-urban scale. A sub-grid scale module has been added to the classical computation of the grid-averaged pollutant concentration based on the Reynolds-average approach. Since grid cell surfaces cover generally a few square kilometres in meso-scale models, the large heterogeneities in emissions over urban areas cannot be represented, although this may result in concentrations near sources that are very different from the grid averaged levels. From a health outcome perspective, it is important to know how much local concentrations deviate from grid-averaged values due to the proximity to emission sources (e.g. near roads, in residential zones, industrial parks, etc.).

To address the issue of sub-grid scale emission heterogeneity, an emission scheme has been developed and implemented in the CHIMERE model (Valari and Menut, 2010). Instead of adding together emissions from all sources and all activity sectors at each model grid cell, we split them into four different categories: traffic, residential, outdoor activities (entertainment) and all other sources (including point sources). Grid area fractions corresponding to each type of emission are calculated based on high resolution land use data (CORINE land cover at 100 m resolution). Thus, instead of a mean single emission for each model grid cell, four different emission scenarios are used, each one corresponding to a sub-surface of the grid cell. At each model time step, and for the grid cells where we are interested in applying the sub-grid scale calculation, instead of the single "grid-averaged" scenario, concentrations are calculated following all four sub-grid scale scenarios. At the end of the time step, weighted averages of the four estimates for all model species are propagated to the next time step.

In Fig. 20, modelled NO_2 concentrations are compared to surface measurements of the Ile-de-France air-quality network AIRPARIF. Model resolution is $3 km \times 3 km$ and results are shown for a model grid cell within which two AIRPARIF sites lay: a traffic monitor (red circles) and a background monitor (blue crosses). The black line corresponds to the standard model grid-averaged concentrations, whereas coloured lines stand for the results of the sub-grid scale scheme (red for the traffic sector and blue for the residential sector). The added value of the sub-grid implementation is that instead of a single grid-averaged concentration we now have two additional estimates for what pollutant levels are near a road or inside a residential block inside the grid area. This information is especially useful when air-quality model outputs are used to estimate population exposure levels. Sub-grid model concentrations weighted with activity data on the time people spend at home, at the office or in transit give an estimate of personal exposure. This method has been applied to the Paris area in Valari et al. (2011).
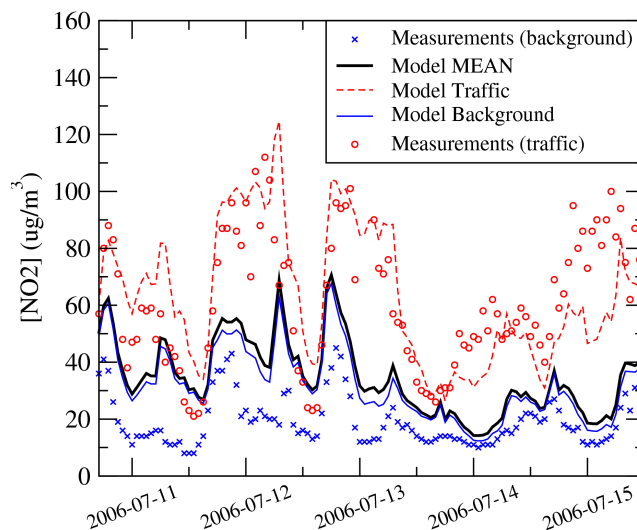

Fig. 20. Surface concentrations of NO_2 time series using the sub-grid scale variability module. The symbols represent AIRPARIF measurements of two stations, one background and one traffic, located in the same CHIMERE cell in Paris, with a horizontal resolution of $3 km \times 3 km$. The plain lines represent the corresponding modelled surface concentrations and show the sub-grid scheme is able to reproduce the large variability of NO_2 depending on the sources in an urban environment. After Valari and Menut (2010).

14 Conclusions and perspectives

This paper presents the complete schemes and parameterisations implemented in CHIMERE (v.2013), a regional chemistry-transport model dedicated to atmospheric composition studies. The model is continuously under development and this article represents the reference model description.

CHIMERE was initially developed for regional and short-term (a few days) pollution episodes. During the last years, new projects and demands have given rise to several needs for model developments, leading to changes in (i) the spatial domain resolution and size, (ii) the simulations duration and (iii) the processes and parameters covered. Spatially, the model domains have been extended to near semi-hemispheric scales for concentration plumes due to mineral dust, forest fires and volcanic emissions. At the same time, urban versions have been developed to better understand and quantify the impact of air pollution on health.

As for its perspectives, the model will continue to evolve by refining the schemes and parameterisations used. In addition, the next version will calculate meteorology online. Indeed, historically, and for computational reasons, many CTMs such as CHIMERE have been essentially used offline, i.e. they are forced with precalculated meteorological fields and surface state. In order to consider the numerous feedbacks between atmospheric, radiative and chemical processes, the development of platforms coupling online

meteorology, chemistry and vegetation has been identified as a priority for both research and forecast applications. One next big step in CHIMERE development will be to build an online-coupled platform putting together a meteorological model (WRF), a coupled ground–vegetation–hydrology model (ORCHIDEE) and a CTM (CHIMERE). This coupling will be done through the OASIS coupler, which will offer greater flexibility and computational advantages compared to a direct hard-coded implementation of a supermodel that includes all three models. The resulting modelling platform will be used for fundamental research purposes, for assessing the importance of the feedback between meteorology, vegetation and chemistry, and it will be available for research and forecast applications.

Appendix A

MELCHIOR2 chemical mechanism

This appendix presents the MELCHIOR2 gas-phase chemical mechanism and all related model species used in CHIMERE. In Table A1, the notes correspond to the following:

a. Hydrocarbon model species (except for CH_4 and C_2H_4) represent groups of hydrocarbons with similar reactivity. As a "definition", a typical representative of this group is given. This is also true for the degradation products.

b. For the concept of "chemical operators; see Carter (1990) and Aumont et al. (2003).

The numbers in the Tables correspond to the following references:

1. Atkinson et al. (1997),

2. Donahue et al. (1997),

3. De Moore et al. (1994),

4. Mentel et al. (1996),

5. Atkinson (1990),

6. Paulson and Seinfeld (1992),

7. LeBras et al. (1997)

8. Atkinson (1994),

9. DeMore et al. (1990)

10. Canosa-Mas et al. (1996),

11. Johnston et al. (1996),

12. Martinez et al. (1992),

13. Jenkin et al. (1997),

14. Plum et al. (1983),

15. Bierbach et al. (1994),

16. Lightfoot and Cox (1992),

17. Kirchner and Stockwell (1996),

18. Aumont et al. (2003)

The notes for the reactions correspond to the following remarks:

– n1: Rate constants containing a density dependent term in a minor reaction channel have been simplified by putting an average boundary layer molecular density of 2.5×10^{19} molecules cm^{-3}.

– n2: For operator reactions with OH, oROOH is interpreted as 2-butyl hydrogen peroxide, obioH as a peroxide from isoprene degradation, and PANH represents unsaturated organic peroxides; due to lack of data, the rate constants of these compounds and of peroxy acetyl acid have been estimated using structure reactivity relationships in Kwok and Atkinson (1995).

– n3: The rate constant of the operator reaction oRO_2+NO has been set to that of the i-C_3H7O_2+NO reaction given in Lightfoot and Cox (1992); that of oPAN+NO to that of CH_3COO_2+NO [1], the rate constant for oRO_2NO+NO, is taken from that of ISNIR (nitrate peroxy radicals from isoprene degradation) + NO, (Paulson and Seinfeld, 1992).

– n4: The rate constants for the operator reactions oRO_2, obio, RO_2NI+HO_2 have been set to that of the reaction C_2H5O_2+HO_2 and oPAN+HO_2 has been taken from CH_3COO_2+HO_2, as in Atkinson et al. (1997).

– n5: Radical conserving and terminating pathways are combined to single reactions; rate constants in operator reactions are affected by interpreting oRO_2 as 2-butyl peroxy radical (Lightfoot and Cox, 1992), obio as a peroxy radical from isoprene degradation (Paulson and Seinfeld, 1992) and oPAN as CH_3COO_2.

– n6: Reaction rates of the operators oPAN and toPAN have been set to those of the peroxy acetyl radical and PAN, respectively.

– n7: The reactions O_3+h$\nu \rightarrow$ O(1D), O(1D)+$H_2O \rightarrow$ 2OH, O(1D)+M $\rightarrow$ O(3P)+M and O(3P)+O_2+M $\rightarrow$ O_3+M have been combined to reaction O_3+h$\nu\rightarrow$ O(1D) by taking into account H_2O and M concentrations in order to adjust the photolysis frequency.

– n8: Due to lack of data, photolysis frequencies of higher organic peroxides are taken as that of CH_3OOH.

Table A1. Species list of the reduced MELCHIOR2 gas-phase chemical mechanism.

Symbol	Full name
Inorganic compounds	
O_3	ozone
H_2O_2	hydrogen peroxide
OH	hydroxyl radical
HO_2	hydroperoxyl radical
NO	nitrogen oxide
NO_2	nitrogen dioxide
NO_3	nitrogen trioxide
N_2O_5	dinitrogen pentoxide
HONO	nitrous acid
HNO_3	nitric acid
CO	carbon monoxide
SO_2	sulphur dioxide
Hydrocarbon species[a]	
CH_4	methane
C_2H_6	ethane
NC_4H_{10}	n-butane
C_2H_4	ethene
C_3H_6	propene
OXYL	o-xylene
C_5H_8	isoprene
APINEN	α-pinene
BPINEN	β-pinene
LIMONE	limonene
TERPEN	terpenes
HUMULE	humulene
OCIMEN	ocimene
Carbonyls	
HCHO	formaldehyde
CH_3CHO	acetaldehyde
CH_3COE	methyl ethyl ketone
GLYOX	glyoxal
MGLYOX	methyl glyoxal
CH_3COY	dimethyl glyoxal
MEMALD	unsaturated dicarbonyls, reacting like 4-oxo-2-pentenal
MVK	methyl vinyl ketone
MAC	methacrolein
Organic nitrates	
PAN	peroxyacetyl nitrate
CARNIT	nitrate carbonyl taken as α-nitrooxy acetone
ISNI	unsaturated nitrate from isoprene degradation
Organic peroxides	
CH_3O_2H	methyl hydroperoxide
PAA	Peroxyacetic acid
Peroxy radicals	
CH_3O_2	methyl peroxy radical
CH_3COO	peroxy acetyl radical
Operators[b]	
oRO_2	representing peroxy radicals from OH attack to C_2H_6, NC_4H_{10}, C_2H_4, C_3H_6, OXYL, CH_3COE, MEMALD, and MVK
oROOH	representing organic peroxides from oRO_2+HO_2 reactions
obio	representing peroxy radicals produced by C_5H_8 and APINEN + OH reaction
obioH	representing biogenic organic peroxides from obio+HO_2 and obio+obio reactions
oPAN	representing PAN homologue compounds (except PAN)
PANH	representing results from oPAN+HO_2 reaction
toPAN	representing results from oPAN+NO_2 reaction
oRN1	representing organic nitrate peroxy radicals from NO_3 attack to C_2H_4, C_3H_6, C_5H_8, APINEN, BPINEN, LIMONE, TERPEN, OCIMEN, HUMULE and OH attack to ISNI

Table A2. Reaction list of the reduced MELCHIOR2 chemical mechanism

Reactions	Kinetic constants	Ref.
$O_3+NO \rightarrow NO_2$	$Ae^{-B/T}$, $A = 1.8 \times 10^{-12}$, $B = 1370$	[1]
$O_3+NO_2 \rightarrow NO_3$	$Ae^{-B/T}$, $A = 1.2 \times 10^{-13}$, $B = 2450$	[1]
$O_3+OH \rightarrow HO_2$	$Ae^{-B/T}$, $A = 1.9 \times 10^{-12}$, $B = 1000$	[1]
$O_3+HO_2 \rightarrow OH$	$Ae^{-B/T}$, $A = 1.4 \times 10^{-14}$, $B = 600$	[1]
$NO+HO_2 \rightarrow OH+NO_2$	$Ae^{-B/T}$, $A = 3.7 \times 10^{-12}$, $B = -240$	[1]
$NO_2+OH+M \rightarrow HNO_3$	troe(3.4×10^{-3}0, 0, 3.2, 4.77×10^{-11}, 0, 1.4, 0.30)	[2], n9
$HO_2+OH \rightarrow H_2O$	$Ae^{-B/T}$, $A = 4.8 \times 10^{-11}$, $B = -250$	[1]
$H_2O_2+OH \rightarrow HO_2$	$Ae^{-B/T}$, $A = 2.9 \times 10^{-12}$, $B = 160$	[1]
$HNO_3+OH \rightarrow NO_3$	$Ae^{-B/T}$, $A = 5.5 \times 10^{-15}$, $B = -985$	[3], n1
$CO+OH \rightarrow HO_2+CO_2$	$Ae^{-B/T}(300/T)^N$, $A = 2 \times 10^{-13}$, $B = 0$, $N = 1$	[3], n1
$HO_2+HO_2 \rightarrow H_2O_2$	$Ae^{-B/T}$, $A = 2.2 \times 10^{-13}$, $B = -740$	[1], n1
$HO_2+HO_2+H_2O \rightarrow H_2O_2$	$Ae^{-B/T}$, $A = 4.52 \times 10^{-3}4$, $B = -2827$	[1], n1
$NO_3+HO_2 \rightarrow NO_2+OH$	4×10^{-12}	[1]
$NO_3+H_2O_2 \rightarrow HNO_3+HO_2$	2×10^{-15}	[3]
$NO_3+NO \rightarrow 2*NO_2$	$Ae^{-B/T}$, $A = 1.8 \times 10^{-11}$, $B = -110$	[1]
$NO_2+NO_3 \rightarrow NO+NO_2$	$Ae^{-B/T}$, $A = 4.5 \times 10^{-14}$, $B = 1260$	[3]
$NO_2+NO_3+M \rightarrow N_2O_5$	troe(2.7×10^{-3}0, 0, 3.4, 2×10^{-12}, 0, -0.2, 0.33)	[1], n9
$N_2O_5+M \rightarrow NO_3+NO_2$	troe(1×10^{-3}, 11 000, 3.5, 9.7×10^{14}, 11080, -0.1, 0.33)	[1], n9
$N_2O_5+H_2O \rightarrow 2*HNO_3$	2.6×10^{-22}	[4]
$N_2O_5+H_2O+H_2O \rightarrow 2*HNO_3$	$2 \times 10^{-3}9$	[4]
$NO+OH+M \rightarrow HONO$	troe($7. \times 10^{-3}$1, 0, 2.6, 1.5×10^{-11}, 0, 0.5, 0.6)	[1], n9
$HONO+OH \rightarrow NO_2$	$Ae^{-B/T}$, $A = 1.8 \times 10^{-11}$, $B = 390$	[1]
$NO+NO+O_2 \rightarrow 2*NO_2$	$Ae^{-B/T}$, $A = 3.30 \times 10^{-39}$, $B = -530.0$	[1]
$NO_2 \rightarrow HONO$	$0.5*depo(NO_2)$	[18]
$SO_2+CH_3O_2 \rightarrow H_2SO_4+HCHO+HO_2$	$4e{-}17$	[3]
$SO_2+OH+M \rightarrow H_2SO_4+HO_2$	troe(4×10^{-3}1, 0, 3.3, 2×10^{-12}, 0, 0, 0.45)	[3], n9
$CH_4+OH \rightarrow CH_3O_2$	$Ae^{-B/T}$, $A = 2.3 \times 10^{-12}$, $B = 1765$	[1]
$C_2H_6+OH \rightarrow CH_3CHO+oRO_2$	$Ae^{-B/T}$, $A = 7.9 \times 10^{-12}$, $B = 1030$	[1]
$NC_4H_{10}+OH \rightarrow 0.9*CH_3COE +0.1*CH_3CHO$ $+0.1*CH_3COO +0.9*oRO_2$	$Ae^{-B/T}(300/T)^N$, $A = 1.36 \times 10^{-12}$, $B = -190$, $N = -2$	[5]
$C_2H_4+OH+M \rightarrow 2*HCHO+oRO_2$	troe(7×10^{-29}, 0, 3.1, 9×10^{-12}, 0, 0, 0.7)	[1], n9
$C_3H_6+OH+M \rightarrow HCHO+CH_3CHO+oRO_2$	troe($8e{-}27$, 0, 3.5, 3×10^{-11}, 0, 0, 0.5)	[1], n9
$OXYL+OH \rightarrow MEMALD+MGLYOX+oRO_2$	1.37×10^{-11}	[5]
$C_5H_8+OH \rightarrow 0.32*MAC +0.42*MVK +0.74*HCHO +obio$	$Ae^{-B/T}$, $A = 2.55 \times 10^{-11}$, $B = -410$	[1]
$APINEN+OH \rightarrow 0.8*CH_3CHO+0.8*CH_3COE+obio$	$Ae^{-B/T}$, $A = 1.21 \times 10^{-11}$, $B = -444$	[17]
$BPINEN+OH \rightarrow 0.8*CH_3CHO+0.8*CH_3COE+obio$	$Ae^{-B/T}$, $A = 1.21 \times 10^{-11}$, $B = -444$	[17]
$LIMONE+OH \rightarrow 0.8*CH_3CHO+0.8*CH_3COE+obio$	$Ae^{-B/T}$, $A = 1.21 \times 10^{-11}$, $B = -444$	[17]
$HUMULE+OH \rightarrow 0.8*CH_3CHO+0.8*CH_3COE+obio$	$Ae^{-B/T}$, $A = 1.21 \times 10^{-11}$, $B = -444$	[17]
$OCIMEN+OH \rightarrow 0.8*CH_3CHO+0.8*CH_3COE+obio$	$Ae^{-B/T}$, $A = 1.21 \times 10^{-11}$, $B = -444$	[17]
$TERPEN+OH \rightarrow 0.8*CH_3CHO+0.8*CH_3COE+obio$	$Ae^{-B/T}$, $A = 1.21 \times 10^{-11}$, $B = -444$	[17]
$HCHO+OH \rightarrow CO+HO_2$	$Ae^{-B/T}$, $A = 8.6 \times 10^{-12}$, $B = -20$	[1]
$CH_3CHO+OH \rightarrow CH_3COO$	$Ae^{-B/T}$, $A = 5.6 \times 10^{-12}$, $B = -310$	[1]
$MEMALD+OH \rightarrow GLYOX+MGLYOX+oRO_2$	5.6×10^{-11}	[1]
$CH_3COE+OH \rightarrow CH_3COY+oRO_2$	$Ae^{-B/T}(300/T)^N$, $A = 2.92 \times 10^{-13}$, $B = -414$, $N = -2$	[1]
$GLYOX+OH \rightarrow 2*CO+HO_2$	1.1×10^{-11}	[1]
$MGLYOX+OH \rightarrow CH_3COO+CO$	1.5×10^{-11}	[1]
$MVK+OH \rightarrow$ $0.266*MGLYOX$ $+0.266*HCHO$ $+0.684*CH_3CHO +0.684*CH_3COO +0.05*ISNI +0.95*oRO_2$	$Ae^{-B/T}$, $A = 4.1 \times 10^{-12}$, $B = -453$	[6]
$MAC+OH \rightarrow 0.5*CH_3COE+0.5*CO_2+0.5*oPAN$	$Ae^{-B/T}$, $A = 1.86 \times 10^{-11}$, $B = -175$	[6]
$CH_3O_2H+OH \rightarrow CH_3O_2$	$Ae^{-B/T}$, $A = 1.9 \times 10^{-12}$, $B = -190$	[1]
$PPA+OH \rightarrow CH_3COO$	$Ae^{-B/T}$, $A = 1.9 \times 10^{-12}$, $B = -190$	n2
$CH_3O_2H+OH \rightarrow HCHO+OH$	$Ae^{-B/T}$, $A = 1. \times 10^{-12}$, $B = -190$	[1]
$oROOH+OH \rightarrow 0.8*OH+0.2*oRO_2$	$Ae^{-B/T}$, $A = 4.35 \times 10^{-12}$, $B = -455$	n2
$obioH+OH \rightarrow OH$	8×10^{-11}	n2
$PANH+OH \rightarrow 0.2*oPAN$	1.64×10^{-11}	n2
$CARNIT+OH \rightarrow CH_3CHO+CO+NO_2$	$k(T)=Ae^{-B/T}$, $A = 5.6 \times 10^{-12}$, $B = -310$	

Table A2. Continued.

Reactions	Kinetic constants	Ref.
$C_2H_4+NO_3 \rightarrow$ 0.5*CARNIT+HCHO+oRN1	2×10^{-16} [1]	
$C_3H_6+NO_3 \rightarrow$ 0.5*CARNIT +1.5*HCHO +0.5*CH_3CHO +0.5*HO_2 +oRN1	9.45×10^{-15}	[1]
APINEN+$NO_3 \rightarrow$ CH_3CHO+CH_3COE+oRN1	$Ae^{-B/T}$, $A = 14.19 \times 10^{-12}$, $B = 490$	[8]
BPINEN+$NO_3 \rightarrow$ CH_3CHO+CH_3COE+oRN1	$Ae^{-B/T}$, $A = 1.19 \times 10^{-12}$, $B = 490$	[8]
LIMONE+$NO_3 \rightarrow$ CH_3CHO+CH_3COE+oRN1	$Ae^{-B/T}$, $A = 1.19 \times 10^{-12}$, $B = 490$	[8]
OCIMEN+$NO_3 \rightarrow$ CH_3CHO+CH_3COE+oRN1	$Ae^{-B/T}$, $A = 1.19 \times 10^{-12}$, $B = 490$	[8]
HUMULE+$NO_3 \rightarrow$ CH_3CHO+CH_3COE+oRN1	$Ae^{-B/T}$, $A = 1.19 \times 10^{-12}$, $B = 490$	[8]
TERPEN+$NO_3 \rightarrow$ CH_3CHO+CH_3COE+oRN1	$Ae^{-B/T}$, $A = 1.19 \times 10^{-12}$, $B = 490$	[8]
$C_5H_8+NO_3 \rightarrow$ 0.85*ISNI +0.1*MAC +0.05*MVK +0.15*HCHO +0.8*HO_2 +oRN1	7.8×10^{-13}	[6]
HCHO+$NO_3 \rightarrow$ CO+HNO_3+HO_2	5.8×10^{-16}	[1]
CH_3CHO+$NO_3 \rightarrow$ CH_3COO+HNO_3	2.8×10^{-15}	[9]
CH_3O_2+$NO_3 \rightarrow$ HCHO+HO_2+NO_2	1.2×10^{-12}	[10]
CH_3COO+$NO_3 \rightarrow$ CH_3O_2+NO_2+CO_2	4×10^{-12}	[10]
oRO_2+$NO_3 \rightarrow$ NO_2+HO_2	1.2×10^{-12}	[10]
obio+$NO_3 \rightarrow$ NO_2+HO_2	1.2×10^{-12}	[10]
oPAN+$NO_3 \rightarrow$ NO_2+HO_2	4×10^{-12}	[10]
oRN1+$NO_3 \rightarrow$ 1.5*NO_2	1.2×10^{-12}	[10]
$C_2H_4+O_3 \rightarrow$ HCHO+0.12*HO_2+0.13*H_2+0.44*CO	$Ae^{-B/T}$, $A = 9.1 \times 10^{-15}$, $B = 2580$	[1]
$C_3H_6+O_3 \rightarrow$ 0.53*HCHO +0.5*CH_3CHO +0.31*CH_3O_2 +0.28*HO_2 +0.15*OH +0.065*H_2 +0.4*CO +0.7*CH_4	$Ae^{-B/T}$, $A = 5.5 \times 10^{-15}$, $B = 1880$	[1]
$C5H8+O_3 \rightarrow$ 0.67*MAC +0.26*MVK +0.55*OH +0.07*C_3H_6 +0.8*HCHO +0.06*HO_2 +0.05*CO +0.3*O_3	$Ae^{-B/T}$, $A = 1.2 \times 10^{-14}$, $B = 2013$	[6]
MAC+$O_3 \rightarrow$ 0.8*MGLYOX +0.7*HCHO +0.215*OH +0.275*HO_2 +0.2*CO +0.2*O_3	$Ae^{-B/T}$, $A = 5.3 \times 10^{-15}$, $B = 2520$	[6]
MVK+$O_3 \rightarrow$ 0.82*MGLYOX +0.8*HCHO +0.04*CH_3CHO +0.08*OH +0.06*HO_2 +0.05*CO +0.2*O_3	$Ae^{-B/T}$, $A = 4.3 \times 10^{-15}$, $B = 2016$	[6]
APINEN+$O_3 \rightarrow$ 1.27*CH_3CHO +0.53*CH_3COE +0.14*CO +0.62*oRO_2 +0.42*HCHO +0.85*OH +0.1*HO_2	$Ae^{-B/T}$, $A = 1.0 \times 10^{-15}$, $B = 736$	[8]
BPINEN+$O_3 \rightarrow$ 1.27*CH_3CHO +0.53*CH_3COE +0.14*CO +0.62*oRO_2 +0.42*HCHO +0.85*OH +0.1*HO_2	$Ae^{-B/T}$, $A = 1.0 \times 10^{-15}$, $B = 736$	[8]
LIMONE+$O_3 \rightarrow$ 1.27*CH_3CHO +0.53*CH_3COE +0.14*CO +0.62*oRO_2 +0.42*HCHO +0.85*OH +0.1*HO_2	$Ae^{-B/T}$, $A = 1.0 \times 10^{-15}$, $B = 736$	[8]
TERPEN+$O_3 \rightarrow$ 1.27*CH_3CHO +0.53*CH_3COE +0.14*CO +0.62*oRO_2 +0.42*HCHO +0.85*OH +0.1*HO_2	$Ae^{-B/T}$, $A = 1.0 \times 10^{-15}$, $B = 736$	[8]
OCIMEN+$O_3 \rightarrow$ 1.27*CH_3CHO +0.53*CH_3COE +0.14*CO +0.62*oRO_2 +0.42*HCHO +0.85*OH +0.1*HO_2	$Ae^{-B/T}$, $A = 1.0 \times 10^{-15}$, $B = 736$	[8]
HUMULE+$O_3 \rightarrow$ 1.27*CH_3CHO +0.53*CH_3COE +0.14*CO +0.62*oRO_2 +0.42*HCHO +0.85*OH +0.1*HO_2	$Ae^{-B/T}$, $A = 1.0 \times 10^{-15}$, $B = 736$	[8]
CH_3O_2+NO $\rightarrow$ HCHO+NO_2+HO_2	$Ae^{-B/T}$, $A = 4.2 \times 10^{-12}$, $B = -180$	[1]
CH_3COO+NO $\rightarrow$ CH_3O_2+NO_2+CO_2	2×10^{-11}	[1]
oRO_2+NO $\rightarrow$ NO_2+HO_2	4×10^{-12}	n3
obio+NO $\rightarrow$ 0.86*NO_2+0.78*HO_2+0.14*ISNI	$Ae^{-B/T}$, $A = 1.4 \times 10^{-11}$, $B = 180$	[6]
oPAN+NO $\rightarrow$ NO_2+HO_2	1.4×10^{-11}	n3
oRN1+NO $\rightarrow$ 1.5*NO_2	4×10^{-11}	n3

Table A2. Continued.

Reactions	Kinetic constants	Ref.
$CH_3O_2+HO_2 \rightarrow CH_3O_2H$	$Ae^{-B/T}$, $A = 4.1 \times 10^{-13}$, $B = -790$	[1]
$CH_3COO+HO_2 \rightarrow 0.67*PPA+0.33*O_3$	$Ae^{-B/T}$, $A = 4.3 \times 10^{-13}$, $B = -1040$	[1]
$oRO_2+HO_2 \rightarrow oROOH$	$Ae^{-B/T}$, $A = 2.7 \times 10^{-13}$, $B = -1000$	n4
$obio+HO_2 \rightarrow obioH$	$Ae^{-B/T}$, $A = 2.7 \times 10^{-13}$, $B = -1000$	n4
$oPAN+HO_2 \rightarrow PANH$	$Ae^{-B/T}$, $A = 2.7 \times 10^{-13}$, $B = -1000$	n4
$oRN1+HO_2 \rightarrow X$	$Ae^{-B/T}$, $A = 2.7 \times 10^{-13}$, $B = -1000$	n4
$CH_3O_2+CH_3O_2 \rightarrow 1.35*HCHO+0.7*HO_2$	$Ae^{-B/T}$, $A = 1.13 \times 10^{-13}$, $B = -356$	[1], n5
$CH_3COO+CH_3O_2 \rightarrow 0.5*CH_3O_2+0.5*CO_2+HCHO+0.5*HO_2$	$Ae^{-B/T}$, $A = 3.34 \times 10^{-12}$, $B = -400$	[1], n5
$oRO_2+CH_3O_2 \rightarrow 0.65*HCHO+0.8*HO_2+0.35*CH_3OH$	$Ae^{-B/T}$, $A = 1.5 \times 10^{-13}$, $B = -220$	n5
$obio+CH_3O_2 \rightarrow 0.8*HO_2+0.5*HCHO$	$Ae^{-B/T}$, $A = 2.44 \times 10^{-11}$, $B = 223$	n5
$oPAN+CH_3O_2 \rightarrow HCHO+0.5*HO_2$	$Ae^{-B/T}$, $A = 7.9 \times 10^{-12}$, $B = -140$	n5
$CH_3COO+CH_3COO \rightarrow 2.*CH_3O_2+2.*CO_2$	$Ae^{-B/T}$, $A = 2.8 \times 10^{-12}$, $B = -530$	[1], n5
$oRO_2+CH_3COO \rightarrow 0.8*CH_3O_2+0.8*CO_2+0.8*HO_2$	$Ae^{-B/T}$, $A = 8.6 \times 10^{-13}$, $B = -260$	n5
$obio+CH_3COO \rightarrow 0.5*HCHO+1.5*HO_2+0.7*CO_2$	$Ae^{-B/T}$, $A = 1.18 \times 10^{-11}$, $B = 127$	n5
$oPAN+CH_3COO \rightarrow CH_3O_2+CO_2+HO_2$	$Ae^{-B/T}$, $A = 3.34 \times 10^{-12}$, $B = -400$	n5
$oRO_2+oRO_2 \rightarrow 1.3*HO_2$	6.4×10^{-14}	n5
$CH_3COO+NO_2+M \rightarrow PAN$	troe(2.7×10^{-28}, 0, 7.1, 1.2×10^{-11}, 0, 0.9, 0.3)	[1], n9
$oPAN+NO_2+M \rightarrow toPAN$	troe(2.7×10^{-28}, 0, 7.1, 1.2×10^{-11}, 0, 0.9, 0.3)	n6, n9
$PAN+M \rightarrow CH_3COO+NO_2$	troe(4.9×10^{-3}, 12100, 0, 5.4×10^{16}, 13830, 0, 0.3)	[1], n9
$toPAN+M \rightarrow oPAN+NO_2$	troe(4.9×10^{-3}, 12100, 0, 5.4×10^{16}, 13830, 0, 0.3)	n6, n9
$PAN+OH \rightarrow HCHO+NO_3+CO_2$	$Ae^{-B/T}$, $A = 9.5 \times 10^{-13}$, $B = 650$	[1]
$toPAN+OH \rightarrow NO_3+CO_2$	$Ae^{-B/T}$, $A = 3.25 \times 10^{-13}$, $B = -500$	n6
$ISNI+OH \rightarrow 0.95*CH_3CHO +0.475*CH_3COE +0.475*MG-LYOX +0.05*ISNI +0.05*HO_2 + oRN1$	3.4×10^{-11}	[6]
$O_3 \rightarrow 2*OH$	photorate (for calculation, see Sect. 7.2)	[3], n7
$NO_2 \rightarrow NO+O_3$	photorate	[3]
$NO_3 \rightarrow NO_2+O_3$	photorate	[3], [11]
$NO_3 \rightarrow NO$	photorate	[3], [11]
$N_2O_5 \rightarrow NO_2+NO_3$	photorate	[3]
$H_2O_2 \rightarrow 2*OH$	photorate	[3]
$HNO_3 \rightarrow NO_2+OH$	photorate	[3]
$HONO \rightarrow NO+OH$	photorate	[3]
$HCHO \rightarrow CO+2*HO_2$	photorate	[3]
$HCHO \rightarrow CO+H_2$	photorate	[3]
$CH_3CHO \rightarrow CH_3O_2+HO_2+CO$	photorate	[1]
$CH_3COE \rightarrow CH_3COO+CH_3CHO+oRO_2$	photorate	[11], [12]
$CH_3COY \rightarrow 2*CH_3COO$	photorate	[13], [14]
$MGLYOX \rightarrow CH_3COO+HO_2+CO$	photorate	[1]
$GLYOX \rightarrow 0.6*HO_2+2*CO+0.7*H_2$	photorate	[13], [14]
$MEMALD \rightarrow 0.5*MVK +0.5*MALEIC +0.5*oPAN +0.5*HCHO +0.5*HO_2$	photorate	[15]
$CH_3O_2H \rightarrow HCHO+OH+HO_2$	photorate	[3]
$PPA \rightarrow CH_3O_2+CO_2+OH$	photorate	n8
$oROOH \rightarrow OH+HO_2$	photorate	n8
$obioH \rightarrow OH+HO_2$	photorate	n8
$PANH \rightarrow OH+HO_2$	photorate	n8
$PAN \rightarrow CH_3COO+NO_2$	photorate	[3]

– n9: Three body Troe reactions, given in the form as in
Atkinson et al. (1997):

$$k = \frac{k_0[M]}{1 + \frac{k_0[M]}{k_\infty}} f^p \tag{A1}$$

with

$$p = (1 + (\log_{10}(k_0[M]/k_\infty))^2)^{-1}, \tag{A2}$$

$$k_0 = A_0 e^{\left(-\frac{B_0}{T}\right)} \left(\frac{T}{300}\right)^{-n}, \tag{A3}$$

$$k_\infty = A_\infty e^{\left(-\frac{B_\infty}{T}\right)} \left(\frac{T}{300}\right)^{-n}, \tag{A4}$$

The parameters are given in the order
$A_0, B_0, n, A_\infty, B_\infty, m, f$.

The publication of this article
is financed by CNRS-INSU.

References

Akagi, S. K., Yokelson, R. J., Wiedinmyer, C., Alvarado, M. J.,
Reid, J. S., Karl, T., Crounse, J. D., and Wennberg, P. O.: Emis-
sion factors for open and domestic biomass burning for use
in atmospheric models, Atmos. Chem. Phys., 11, 4039–4072,
doi:10.5194/acp-11-4039-2011, 2011.

Alfaro, S. C. and Gomes, L.: Modeling mineral aerosol production
by wind erosion: Emission intensities and aerosol size distribu-
tion in source areas, J. Geophys. Res., 106, 18075–18084, 2001.

Allen, A., Nemitz, E., Shi, J., Harrison, R., and Greenwood, J.: Size
distribution of trace metals in atmospheric aerosols in the United
Kingdom, Atmos. Environ., 35, 4581–4591, 2001.

Alvarado, M. J. and Prinn, R. G.: Formation of ozone and growth
of aerosols in young smoke plumes from biomass burning, Part
1: Lagrangian parcel studies, J. Geophys. Res., 114, D09306,
doi:10.1029/2008JD011144, 2009.

Anav, A., Menut, L., Khvorostiyanov, D., and Viovy, N.: Im-
pact of tropospheric ozone on the Euro-Mediterranean vegeta-
tion, Glob. Change Biol., 17, 2342–2359, doi:10.1111/j.1365-
2486.2010.02387.x, 2011.

Atkinson, R.: Gas-phase tropospheric chemistry of organic-
compounds – a review, Atmos. Environ., 24, 1–41, 1990.

Atkinson, R.: Gas-phase tropospheric chemistry of organic-
compounds, J. Phys. Chem. Ref. Data, p. R1, 1994.

Atkinson, R., Baulsch, D. L., Cox, R. A., Hampton, R. F., Kerr,
J. A., Rossi, M. J., and Troe, J.: Evaluated kinetics, photochemi-
cal and heterogeneous data, J. Phys. Chem., 26, 521–1012, 1997.

Attrep, M. and Anirudhan, M.: Atmospheric inorganic and organic
arsenic, Trace Subst. Environ. Health, 11, 365–369, 1977.

Aumont, B., Chervier, F., and Laval, S.: Contribution of HONO to
the $NO_x/HO_x/O_3$ chemistry in the polluted boundary layer, At-
mos. Environ., 37, 487–498, 2003.

Aumont, B., Szopa, S., and Madronich, S.: Modelling the evolution
of organic carbon during its gas-phase tropospheric oxidation:
development of an explicit model based on a self generating ap-
proach, Atmos. Chem. Phys., 5, 2497–2517, doi:10.5194/acp-5-
2497-2005, 2005.

Baer, M. and Nester, K.: Parameterization of trace gas dry deposi-
tion velocities for a regional mesoscale diffusion model., Ann.
Geophys., 10, 912–923, 1992,
http://www.ann-geophys.net/10/912/1992/.

Berge, E.: Coupling of wet scavenging of sulphur to clouds in a
numerical weather prediction model, Tellus, 45B, 1–22, 1993.

Bessagnet, B., Hodzic, A., Vautard, R., Beekmann, M., Cheinet, S.,
Honoré, C., Liousse, C., and Rouil, L.: Aerosol modeling with
CHIMERE: preliminary evaluation at the continental scale, At-
mos. Environ., 38, 2803–2817, 2004.

Bessagnet, B., Hodzic, A., Blanchard, O., Lattuati, M., Le Bi-
han, O., and Marfaing, H.: Origin of particulate matter pollution
episodes in wintertime over the Paris Basin, Atmos. Environ., 39,
6159–6174, 2005.

Bessagnet, B., Menut, L., Aymoz, G., Chepfer, H., and Vautard,
R.: Modelling dust emissions and transport within Europe: the
Ukraine March 2007 event, J. Geophys. Res., 113, D15202,
doi:10.1029/2007JD009541, 2008.

Bessagnet, B., Menut, L., Curci, G., Hodzic, A., Guillaume, B., Li-
ousse, C., Moukhtar, S., Pun, B., Seigneur, C., and Schulz, M.:
Regional modeling of carbonaceous aerosols over Europe – Fo-
cus on Secondary Organic Aerosols, J. Atmos. Chem., 61, 175–
202, 2009.

Bicheron, P., Amberg, V., Bourg, L., Petit, D., Huc, M., Miras, B.,
Brockmann, C., Hagolle, O., Delwart, S., Ranera, F., Leroy, M.,
and Arino, O.: Geolocation Assessment of MERIS GlobCover
Orthorectified Products, IEEE Trans. Geosci. Remote Sens., 49,
2972–2982, doi:10.1109/TGRS.2011.2122337, 2011.

Bierbach, A., Barnes, I., Becker, K. H., and Wiesen, E.: Atmospheric chemistry of unsaturated carbonyls – butenedial, 4-oxo-2-pentenal, 3-hexene-2,5-dione, maleic-anhydride, 3H-furan-2-one, and 5-mehtyl-3H-furan-2-one, Environ. Sci. Technol., 28, 715–729, 1994.

Blond, N. and Vautard, R.: Three-dimensional ozone analyses and their use for short-term ozone forecasts, J. Geophys. Res.-Atmos., 109, D17303, doi:10.1029/2004JD004515, 2004.

Blond, N., Bel, L., and Vautard, R.: Three-dimensional ozone data analysis with an air quality model over the Paris area, J. Geophys. Res.-Atmos., 108, 4744, doi:10.1029/2003JD003679, 2003.

Blond, N., Boersma, K. F., Eskes, H. J., van der A, R. J., Van Roozendael, M., De Smedt, I., Bergametti, G., and Vautard, R.: Intercomparison of SCIAMACHY nitrogen dioxide observations, in situ measurements and air quality modeling results over Western Europe, J. Geophys. Res.-Atmos., 112, D10311, doi:10.1029/2006JD007277, 2007.

Boichu, M., Menut, L., Khvorostyanov, D., Clarisse, L., Clerbaux, C., Turquety, S., and Coheur, P.-F.: Inverting for volcanic SO_2 flux at high temporal resolution using spaceborne plume imagery and chemistry-transport modelling: the 2010 Eyjafjallajökull eruption case-study, Atmos. Chem. Phys. Discuss., 13, 6553–6588, doi:10.5194/acpd-13-6553-2013, 2013.

Bowman, F. m., Odum, J. R., Seinfeld, J. H., and Pandis, S. N.: Mathematical model for gas-particle parttioning of secondary organic aerosols, Atmos. Environ., 31, 3921–3931, 1997.

Broquet, G., Chevallier, F., Rayner, P., Aulagnier, C., Pison, I., Ramonet, M., Schmidt, M., Vermeulen, A. T., , and Ciais, P.: A European summertime CO2 biogenic flux inversion at mesoscale from continuous in situ mixing ratio measurements, J. Geophys. Res., 116, D23303, doi:10.1029/2011JD016202, 2011.

Burney, P., Chinn, S., Jarvis, D., Luczynska, C., and Lai, E.: Variations in the prevalence of respiratory symptoms, self-reported asthma attacks, and use of asthma medication in the European Community Respiratory Health Survey (ECRHS), Eur. Respir. J., 9, 687–695, 1996.

Byun, D. W., Young, J., Pleim, J., Odman, M. T., and Alapaty, K.: Numerical transport algorithms for the community multiscale air quality (CMAQ) chemical transport model in generalized coordinates, in: Science Algorithms of the EPA Models-3 Community Multiscale Air Quality (CMAQ) Modeling System, US-EPA Office of Research and Development Washington, DC 20460, EPA/600/R-99/030, 1999.

Cakmur, R. V., Miller, R. L., and Torres, O.: Incorporating the effect of small-scale circulations upon dust emission in an atmospheric general circulation model, J. Geophys. Res., 109, D07201, doi:10.1029/2003JD004067, 2004.

Canosa-Mas, C. E., King, M. D., Lopez, R., Percival, C. J., Wayne, R. P., Pyle, J. A., Shallcross, D. E., and Daele, V.: Is the reaction between CH3C(O)O2 and NO3 important in the night-time troposphere?, J. Chem. Soc. Faraday Trans., 92, 4385–4389, 1996.

Carter, W. P. L.: A detail mechanism for the gas-phase atmospheric reactions of organic compounds, Atmos. Environ., 24, 481–518, 1990.

Carter, W. P. L.: Documentation of the SAPRC-99 chemical mechanism for VOC reactivity assessment: Final report to California Air Resources Board, Contract 92-329 and Contract 95-308, California Air Resources Board, Sacramento, Calif., 2000.

Carter, W. P. L.: Development of the SAPRC-07 chemical mechanism, Atmos. Environ., 44, 5324–5335, doi:10.1016/j.atmosenv.2010.01.026, 2010.

Chaxel, E., Rieux, C., Rios, I., Thibaudon, M., and Oliver, G.: Modeling the 2011 ragweed season in the French region Rhone-Alpes with the dispersion model CHIMERE, in: International Ragweed Conference, Lyon, France, 28 March 2012, 2012.

Cheinet, S. and Teixeira, J.: A simple formulation for the eddy-diffusivity parameterization of cloud-topped boundary layers, Geophys. Res. Lett., 30, 1930, doi:10.1029/2003GL017377, 2003.

Christensen, J. H., Carter, T. R., Rummukainen, M., and Amanatidis, G.: REvaluating the performance and utility of regional climate models: the PRUDENCE project, Climatic Change, 81, 1–6, 2007.

Clerbaux, C., Boynard, A., Clarisse, L., George, M., Hadji-Lazaro, J., Herbin, H., Hurtmans, D., Pommier, M., Razavi, A., Turquety, S., Wespes, C., and Coheur, P.-F.: Monitoring of atmospheric composition using the thermal infrared IASI/MetOp sounder, Atmos. Chem. Phys., 9, 6041–6054, doi:10.5194/acp-9-6041-2009, 2009.

Colella, P. and Woodward, P. R.: The piecewise parabolic method (PPM) for gas-dynamical simulations, J. Comput. Phys., 11, 38–39, 1984.

Colette, A., Favez, O., Meleux, F., Chiappini, L., Haeffelin, M., Morille, Y., Malherbe, L., Papin, A., Bessagnet, B., Menut, L., Leoz, E., and Rouïl, L.: Assessing in near real time the impact of the April 2010 Eyjafjallajokull ash plume on air quality, Atmos. Environ., 45, 1217–1221, 2011a.

Colette, A., Granier, C., Hodnebrog, Ø., Jakobs, H., Maurizi, A., Nyiri, A., Bessagnet, B., D'Angiola, A., D'Isidoro, M., Gauss, M., Meleux, F., Memmesheimer, M., Mieville, A., Rouïl, L., Russo, F., Solberg, S., Stordal, F., and Tampieri, F.: Air quality trends in Europe over the past decade: a first multi-model assessment, Atmos. Chem. Phys., 11, 11657–11678, doi:10.5194/acp-11-11657-2011, 2011b.

Colette, A., Meleux, F., Bessagnet, B., Granier, C., Hodnebrog, A., Pirovano, G., and Szopa, S.: On the impact of chemical boundary conditions on air quality modelling, Geophys. Res. Abstr., EGU2011–11 655, doi:10.1007/978-1-4020-6766-2_6, EGU General Assembly 2011, Vienna, Austria, 2011.

Coman, A., Foret, G., Beekmann, M., Eremenko, M., Dufour, G., Gaubert, B., Ung, A., Schmechtig, C., Flaud, J.-M., and Bergametti, G.: Assimilation of IASI partial tropospheric columns with an Ensemble Kalman Filter over Europe, Atmos. Chem. Phys., 12, 2513–2532, doi:10.5194/acp-12-2513-2012, 2012.

COSY: Experimental regional forecast at Laboratoire de Meteoologie Dynamique, with WRF and CHIMERE, Daily comparisons to the SIRTA observatory measurements, available at: http://www.lmd.polytechnique.fr/cosy/ (last access: March 2013), 2013.

Courant, R., Isaacson, E., and Rees, M.: On the solution of nonlinear hyperbolic differential equations by finite differences, Comm. Pure Appl. Math., 5, 243–255, 1952.

Curci, G., Beekmann, M., Vautard, R., Smiatek, G., Steinbrecher, R., Theloke, J., and Friedrich, R.: Modelling study of the impact of isoprene and terpene biogenic emissions on European ozone levels, Atmos. Environ., 43, 1444–1455, doi:10.1016/j.atmosenv.2008.02.070, 2009.

Curci, G., Palmer, P. I., Kurosu, T. P., Chance, K., and Visconti, G.: Estimating European volatile organic compound emissions using satellite observations of formaldehyde from the Ozone Monitoring Instrument, Atmos. Chem. Phys., 10, 11501–11517, doi:10.5194/acp-10-11501-2010, 2010.

Cuvelier, C., Thunis, P., Vautard, R., Amann, M., Bessagnet, B., Bedogni, M., Berkowicz, R., Brocheton, F., Builtjes, P., Denby, B., Douros, G., Graf, A., Honoré, C., Jonson, J., Kerschbaumer, A., de Leeuw, F., Moussiopoulos, N., Philippe, C., Pirovano, G., Rouil, L., Schaap, M., Stern, R., Tarrason, L., Vignati, E., Volta, L., White, L., Wind, P., and Zuber, A.: CityDelta: a model intercomparison study to explore the impact of emission reductions in European cities in 2010, Atmos. Environ., 41, 189–207, doi:10.1016/j.atmosenv.2006.07.036, 2007.

Darbah, J., Kubiske, M., Nelson, N., Oksanen, E., and Vapaavuori, E.: Effects of decadal exposure to interacting elevated CO_2 and/or O_3 on paper birch (Betula papyrifera) reproduction, Environ. Pollut., 155, 446–452, 2008.

Deguillaume, L., Beekmann, M., and Derognat, C.: Uncertainty evaluation of ozone production and its sensitivity to emission changes over the Ile-deFrance region during summer periods, J. Geophys. Res., 113, D02304, doi:10.1029/2007JD009081, 2008.

de Meij, A., Gzella, A., Cuvelier, C., Thunis, P., Bessagnet, B., Vinuesa, J. F., Menut, L., and Kelder, H. M.: The impact of MM5 and WRF meteorology over complex terrain on CHIMERE model calculations, Atmos. Chem. Phys., 9, 6611–6632, doi:10.5194/acp-9-6611-2009, 2009.

De Moore, W. B., Sandetr, S. P., Golden, D. M., Hampton, R. F., Kurylo, M. J., Howard, C. J., Ravishankara, A. R., Kolb, C. E., and Molina, M. J.: Chemical kinetics and photochimical data for use in stratospheric modelling evaluation, JPL publication, 94, 26, JPL, Pasadena, US, 1994.

DeMore, W., Sander, S., Golden, D., Molina, M., Hampson, R., Kurylo, M., Howard, C., and Ravishankara, A.: Chemical kinetics and photochemical data for use in stratospheric modeling. Evaluation number 9, Jet Propulsion Lab., California Inst. Technol., Pasadena, CA, 1990.

Derognat, C., Beekmann, M., Baeumle, M., Martin, D., and Schmidt, H.: Effect of biogenic volatile organic compound emissions on tropospheric chemistry during the Atmospheric Pollution Over the Paris Area (ESQUIF) campaign in the Ile-de-France region, J. Geophys. Res.-Atmos., 108, 8560, doi:10.1029/2001JD001421, 2003.

Donahue, N. M., Dubey, M. K., Mohrschladt, R., Demerjian, K. L., and Anderson, J. G.: High-pressure flow study of the reactions $OH + NO_x \rightarrow HONO_x$: Errors in the falloff region, J. Geophys. Res., 102, 6159–6168, 1997.

Dufour, G., Wittrock, F., Camredon, M., Beekmann, M., Richter, A., Aumont, B., and Burrows, J. P.: SCIAMACHY formaldehyde observations: constraint for isoprene emission estimates over Europe?, Atmos. Chem. Phys., 9, 1647–1664, doi:10.5194/acp-9-1647-2009, 2009.

Dufour, G., Eremenko, M., Griesfeller, A., Barret, B., LeFlochmoën, E., Clerbaux, C., Hadji-Lazaro, J., Coheur, P.-F., and Hurtmans, D.: Validation of three different scientific ozone products retrieved from IASI spectra using ozonesondes, Atmos. Meas. Tech., 5, 611–630, doi:10.5194/amt-5-611-2012, 2012.

ECCAD: Emissions of atmospheric Compounds and Compilation of Ancillary Data, available at: http://eccad.sedoo.fr/eccad_extract_interface/JSF/page_login.jsf, last access: June 2013.

Elbern, H. and Schmidt, H.: Ozone episode analysis by four dimensional variational chemistry data assimilation, J. Geophys. Res., 106, 3569–3590, 2001.

EPA: National Air Toxics Program: The Integrated Urban Strategy, United States Environmental Protection Agency's Federal Register, US EPA Reports, last updated on 19 July 2012, available at: www.epa.gov/ttn/uatw/urban/urbanpg.html (last access: June 2013), 1999.

Eremenko, M., Dufour, G., Foret, G., Keim, C., Orphal, J., Beekmann, M., Bergametti, G., and Flaud, J. M.: Tropospheric ozone distributions over Europe during the heat wave in July 2007 observed from infrared nadir spectra recorded by IASI, Geophys. Res. Lett., 35, doi:10.1029/2008GL034803, 2008.

Erisman, J. W., van Pul, A., and Wyers, P.: Parameterization of surface resistance for the quantification of atmospheric deposition of acidifying pollutants and ozone, Atmos. Environ., 28, 2595–2607, 1994.

Evensen, G.: Sequential data assimilation with a nonlinear quasi-geostrophic model using Monte Carlo methods to forecast error statistics, J. Geophys. Res., 99, 143–162, 1994.

Fenger, J.: Air pollution in the last 50 years – From local to global, Atmos. Environ., 43, 13–22, 2009.

Finlayson-Pitts, B. J. and Pitts, J.: Theory, Experiments, and Applications, in: Chemistry of the Upper and Lower Atmosphere, 1st Edn., San Diego, Academic Press, ISBN:978-0-12-257060-5, 2000.

Folberth, G. A., Hauglustaine, D. A., Lathière, J., and Brocheton, F.: Interactive chemistry in the Laboratoire de Météorologie Dynamique general circulation model: model description and impact analysis of biogenic hydrocarbons on tropospheric chemistry, Atmos. Chem. Phys., 6, 2273–2319, doi:10.5194/acp-6-2273-2006, 2006.

Freitas, S. R., Longo, K. M., Chatfield, R., Latham, D., Silva Dias, M. A. F., Andreae, M. O., Prins, E., Santos, J. C., Gielow, R., and Carvalho Jr., J. A.: Including the sub-grid scale plume rise of vegetation fires in low resolution atmospheric transport models, Atmos. Chem. Phys., 7, 3385–3398, doi:10.5194/acp-7-3385-2007, 2007.

Freitas, S. R., Rodrigues, L. F., Longo, K. M., and Panetta, J.: Impact of a monotonic advection scheme with low numerical diffusion on transport modeling of emissions from biomass burning, J. Adv. in Model. Earth Syst., 3, M01001, doi:10.1029/2011MS000084, 2011.

Friedrich, R.: GENEMIS: Generation of European Emission Data for Episodes, in: Transport and Chemical Transformation of Pollutants in the Troposphere, edited by: Borrell, P. and Borrell, P., vol. 1 of Transport and Chemical Transformation of Pollutants in the Troposphere, pp. 375–386, Springer Berlin Heidelberg, doi:10.1007/978-3-642-59718-3_18, 2000.

Fuchs, N.: The Mechanics of Aerosols, Pergamon Press, Oxford, 1964.

Gelbard, F. and Seinfeld, J. H.: Simulation of multicomponent aerosol dynamics, J. Colloid Int. Sci., 78, 485–501, 1980.

Giglio, L., Randerson, J. T., van der Werf, G. R., Kasibhatla, P. S., Collatz, G. J., Morton, D. C., and DeFries, R. S.: Assessing variability and long-term trends in burned area by merging

multiple satellite fire products, Biogeosciences, 7, 1171–1186, doi:10.5194/bg-7-1171-2010, 2010.

Ginoux, P., Chin, M., Tegen, I., Prospero, J. M., Holben, B., Dubovik, O., and Lin, S. J.: Sources and distributions of dust aerosols simulated with the GOCART model, J. Geophys. Res., 106, 20255–20273, 2001.

Giorgi, F.: A particle dry deposition scheme for use in tracer transport models, J. Geophys. Res., 91, 9794–9806, 1986.

González, M., Vivanco, M. G., Palomino, I., Garrido, J., Santiago, M., and Bessagnet, B.: Modelling some heavy metals air concentration in Europe, Water Air Soil Pollut., 223, 5227–5242, doi:10.1007/s11270-012-1274-6, 2012.

Griffin, R. J., Cocker, E. R., Flagan, R. C., and Seinfeld, J. H.: Organic aerosol formation from the oxidation of biogenic hydrocarbons, J. Geophys. Res., 104, 3555–3567, 1999.

Guelle, W., Balkanski, Y. J., Dibb, J. E., Schulz, M., and Dulac, F.: Wet deposition in a global size-dependent aerosol transport model. 2. Influence of the scavenging scheme on Pb vertical profiles, and deposition, J. Geophys. Res., 103, 28875–28891, 1998.

Guenther, A., Karl, T., Harley, P., Wiedinmyer, C., Palmer, P. I., and Geron, C.: Estimates of global terrestrial isoprene emissions using MEGAN (Model of Emissions of Gases and Aerosols from Nature), Atmos. Chem. Phys., 6, 3181–3210, doi:10.5194/acp-6-3181-2006, 2006.

Hall, S., Khudaish, E., and Hart, A.: Electrochemical oxidation of hydrogen peroxide at platinum electrodes, Part III: Effect of temperature, Electrochim, Electrochim. Acta, 44, 2455–2462, 1999.

Hamaoui-Laguel, L., Meleux, F., Beekmann, M., Bessagnet, B., Genermont, S., Cellier, P., and Létinois, L.: Improving ammonia emissions in air quality modelling for France, Atmos. Environ., doi:10.1016/j.atmosenv.2012.08.002, 2012.

Hanea, R. G., Velders, G. J. M., and Heemink, A.: Data assimilation of ground-level ozone in Europe with a Kalman filter and chemistry transport model, J. Geophys. Res. Atmos., 109, D10302, doi:10.1029/2003JD004283, 2004.

Hansen, M. C. and Reed, B.: A comparison of the IGBP DISCover and University of Maryland 1 km global land cover products, Int. J. Remote Sens., 21, 1365–1373, 2000.

Harrison, R. and Kito, A.: Field intercomparison of filter pack and denuder sampling methods for reactive gaseous and particulate pollutants, Atmos. Environ., 24, 2633–2640, 1990.

HEI: Summary of a Workshop on Metal-Based Fuel Additives and New Engine Technologies, 1998.

Hodzic, A.: Modélisation des aérosols de pollution en Ile de France, Ph.D. thesis, Ecole Polytechnique, 2005.

Hodzic, A. and Jimenez, J. L.: Modeling anthropogenically controlled secondary organic aerosols in a megacity: a simplified framework for global and climate models, Geosci. Model Dev., 4, 901–917, doi:10.5194/gmd-4-901-2011, 2011.

Hodzic, A., Chepfer, H., Vautard, R., Chazette, P., Beekmann, M., Bessagnet, B., Chatenet, B., Cuesta, J., Drobinski, P., Goloub, P., Haeffelin, M., and Morille, Y.: Comparison of aerosol chemistry transport model simulations with lidar and Sun photometer observations at a site near Paris, J. Geophys. Res.-Atmos., 109, D23201, doi:10.1029/2004JD004735, 2004.

Hodzic, A., Vautard, R., Bessagnet, B., Lattuati, M., and Moreto, F.: Long-term urban aerosol simulation versus routine particulate matter observations, Atmos. Environ., 39, 5851–5864, 2005.

Hodzic, A., Bessagnet, B., and Vautard, R.: A model evaluation of coarse-mode nitrate heterogeneous formation on dust particles, Atmos. Environ., 40, 4158–4171, 2006a.

Hodzic, A., Vautard, R., Chazette, P., Menut, L., and Bessagnet, B.: Aerosol chemical and optical properties over the Paris area within ESQUIF project, Atmos. Chem. Phys., 6, 3257–3280, doi:10.5194/acp-6-3257-2006, 2006b.

Hodzic, A., Vautard, R., Chepfer, H., Goloub, P., Menut, L., Chazette, P., Deuzé, J. L., Apituley, A., and Couvert, P.: Evolution of aerosol optical thickness over Europe during the August 2003 heat wave as seen from CHIMERE model simulations and POLDER data, Atmos. Chem. Phys., 6, 1853–1864, doi:10.5194/acp-6-1853-2006, 2006.c.

Hodzic, A., Madronich, S., Bohn, B., Massie, S., Menut, L., and Wiedinmyer, C.: Wildfire particulate matter in Europe during summer 2003: meso-scale modeling of smoke emissions, transport and radiative effects, Atmos. Chem. Phys., 7, 4043–4064, doi:10.5194/acp-7-4043-2007, 2007.

Hodzic, A., Jimenez, J. L., Madronich, S., Aiken, A. C., Bessagnet, B., Curci, G., Fast, J., Lamarque, J.-F., Onasch, T. B., Roux, G., Schauer, J. J., Stone, E. A., and Ulbrich, I. M.: Modeling organic aerosols during MILAGRO: importance of biogenic secondary organic aerosols, Atmos. Chem. Phys., 9, 6949–6981, doi:10.5194/acp-9-6949-2009, 2009.

Hodzic, A., Jimenez, J. L., Madronich, S., Canagaratna, M. R., DeCarlo, P. F., Kleinman, L., and Fast, J.: Modeling organic aerosols in a megacity: potential contribution of semi-volatile and intermediate volatility primary organic compounds to secondary organic aerosol formation, Atmos. Chem. Phys., 10, 5491–5514, doi:10.5194/acp-10-5491-2010, 2010a.

Hodzic, A., Jimenez, J. L., Prévôt, A. S. H., Szidat, S., Fast, J. D., and Madronich, S.: Can 3-D models explain the observed fractions of fossil and non-fossil carbon in and near Mexico City?, Atmos. Chem. Phys., 10, 10997–11016, doi:10.5194/acp-10-10997-2010, 2010b.

Hoffmann, M. R. and Calvert, J. G.: Chemical transformation modules for eulerian acid deposition models, ePA/600/3-85/017, 1985.

Hollingsworth, A., Engelen, R. J., Benedetti, A., Dethof, A., Flemming, J., Kaiser, J. W., Morcrette, J.-J., Simmons, A. J., Textor, C., Boucher, O., Chevallier, F., Rayner, P., Elbern, H., Eskes, H., Granier, C., Peuch, V.-H., Rouil, L., and Schultz, M. G.: Toward a monitoring and forecasting system for atmospheric composition: The GEMS project, B. Am. Meteorol. Soc., 89, 1147–1164, 2008.

Honoré, C. and Vautard, R.: Photochemical regimes in urban atmospheres: The influence of dispersion, Geophys. Res. Lett., 27, 1895–1898, 2000.

Honoré, C., Rouïl, L., Vautard, R., Beekmann, M., Bessagnet, B., Dufour, A., Elichegaray, C., Flaud, J., Malherbe, L., Meleux, F., Menut, L., Martin, D., Peuch, A., Peuch, V., and Poisson, N.: Predictability of European air quality: The assessment of three years of operational forecasts and analyses by the PREV'AIR system, J. Geophys. Res., 113, D04301, doi:10.1029/2007JD008761, 2008.

Hourdin, F. and Armengaud, A.: On the use of finite volume methods for atmospheric advection of trace species, Part I: Test of various formulations in a General Circulation Models, Mon. Weather Rev., 127, 822–837, 1999.

Huijnen, V., Eskes, H. J., Poupkou, A., Elbern, H., Boersma, K. F., Foret, G., Sofiev, M., Valdebenito, A., Flemming, J., Stein, O., Gross, A., Robertson, L., D'Isidoro, M., Kioutsioukis, I., Friese, E., Amstrup, B., Bergstrom, R., Strunk, A., Vira, J., Zyryanov, D., Maurizi, A., Melas, D., Peuch, V.-H., and Zerefos, C.: Comparison of OMI NO2 tropospheric columns with an ensemble of global and European regional air quality models, Atmos. Chem. Phys., 10, 3273–3296, doi:10.5194/acp-10-3273-2010, 2010.

Huneeus, N., Chevallier, F., and Boucher, O.: Estimating aerosol emissions by assimilating observed aerosol optical depth in a global aerosol model, Atmos. Chem. Phys., 12, 4585–4606, doi:10.5194/acp-12-4585-2012, 2012.

Jacob, D. J.: Heterogeneous chemistry and tropospheric ozone, Atmos. Environ., 34, 2131–2159, 2000.

Jaffe, D. A. and Wigder, N. L.: Ozone production from wildfires : a critical review, Atmos. Environ., 51, 1–10, doi:10.1016/j.atmosenv.2011.11.063, 2012.

Jenkin, M. E., Saunders, S. M., and Pilling, M.: The tropospheric degradation of volatile organic compounds: A protocol for mechanism development, Atmos. Environ., 31, 81–104, 1997.

Johnson, D. L. and Braman, R. S.: Alkyl- and inorganic arsenic in air samples, Chemosphere, 6, 333–338, 1975.

Johnston, H. S., Davis, H. F., and Lee, Y. T.: NO3 photolysis product channels: Quantum yields from observed energy thresholds, J. Phys. Chem., 100, 4713–4723, 1996.

Jung, C., Kim, Y., and Lee, K.: Analytic solution for polydispersed aerosol dynamics by a wet removal process, J. Aerosol Sci., 33, 753–767, 2002.

Kaiser, J. W., Heil, A., Andreae, M. O., Benedetti, A., Chubarova, N., Jones, L., Morcrette, J.-J., Razinger, M., Schultz, M. G., Suttie, M., and van der Werf, G. R.: Biomass burning emissions estimated with a global fire assimilation system based on observed fire radiative power, Biogeosciences, 9, 527–554, doi:10.5194/bg-9-527-2012, 2012.

Kavouras, I., Mihalopoulos, N., and Stephanou, E.: Formation of atmospheric particles from organic acids produced by forests, Nature, 395, 683–686, 1998.

Khvorostyanov, D. V., Menut, L., Dupont, J.-C., Morille, Y., and Haeffelin, M.: The role of WRF land surface schemes on weather simulations in Paris area, in: Proceedings of ISARS 2010 conference, Guyancourt, France, 28 June 2010, abstract number: O-SUR/11, 2010.

Kirchner, F. and Stockwell, W. R.: Effect of peroxy radical reactions on the predicted concentrations of ozone, nitrogenous compounds, and radicals, J. Geophys. Res., 101, 21007–21022, 1996.

Konovalov, I. B., Beekmann, M., Vautard, R., Burrows, J. P., Richter, A., Nüß, H., and Elansky, N.: Comparison and evaluation of modelled and GOME measurement derived tropospheric NO2 columns over Western and Eastern Europe, Atmos. Chem. Phys., 5, 169–190, doi:10.5194/acp-5-169-2005, 2005.

Konovalov, I. B., Beekmann, M., Richter, A., and Burrows, J. P.: Inverse modelling of the spatial distribution of NOx emissions on a continental scale using satellite data, Atmos. Chem. Phys., 6, 1747–1770, doi:10.5194/acp-6-1747-2006, 2006.

Konovalov, I. B., Beekmann, M., Kuznetsova, I. N., Yurova, A., and Zvyagintsev, A. M.: Atmospheric impacts of the 2010 Russian wildfires: integrating modelling and measurements of an extreme air pollution episode in the Moscow region, Atmos. Chem. Phys., 11, 10031–10056, doi:10.5194/acp-11-10031-2011, 2011.

Konovalov, I. B., Beekmann, M., D'Anna, B., and George, C.: Significant light induced ozone loss on biomass burning aerosol: Evidence from chemistry-transport modeling based on new laboratory studies, Geophys. Res. Lett., 39, L17807, doi:10.1029/2012GL052432, 2012.

Krinner, G., Viovy, N., de Noblet-Ducoudre, N., Ogee, J., Polcher, J., Friedlingstein, P., Ciais, P., Sitch, S., and Prentice, I.: A dynamic global vegetation model for studies of the coupled atmosphere-biosphere system, Global Biogeochem. Cy., 19, GB1015, doi:10.1029/2003GB002199, 2005.

Kroll, J. H., Ng, N. L., Murphy, S. M., Flagan, R. C., and Seinfeld, J. H.: Secondary organic aerosol formation from isoprene photooxidation, Environ. Sci. Technol., 40, 1869–1877, doi:10.1021/es0524301, 2006.

Kuenen, J., Denier van der Gon, H., Visschedijk, A., and van der Brugh, H.: High resolution European emission inventory for the years 2003–2007, in: TNO report TNO-060-UT-2011-00588, Utrecht, 2011, 2011.

Kulmala, M., A., L., and Pirjola, L.: Parameterization for sulfuric acid / water nucleation rates, J. Geophys. Res., 103, 8301–8307, 1998.

Kuloglu, E. and Tuncel, G.: Size distribution of trace elements and major ions in the eastern Mediterranean atmosphere, Water Air Soil Pollut., 167, 221–241, 2005.

Kurtenbach, R., Becker, K., Gomes, J., Kleffmann, J., Lorzer, J., Spittler, M., Wiesen, P., Ackermann, R., Geyer, A., and Platt, U.: Investigations of emissions and heterogeneous formation of {HONO} in a road traffic tunnel, Atmos. Environ., 35, 3385–3394, doi:10.1016/S1352-2310(01)00138-8, 2001.

Kwok, E. and Atkinson, R.: Estimation of hydroxyl radical reaction-rate constants for gas-phase organic-compounds using a structure-reactivity relationship – an update, Atmos. Environ., 29, 1685–1695, 1995.

Lattuati, M.: Contribution à l'étude du bilan de l'ozone troposphérique à l'interface de l'Europe et de l'Atlantique Nord: modélisation lagrangienne et mesures en altitude, Phd thesis, Université P.M.Curie, Paris, France, 1997.

LeBras, G., Ravishankara, A., and Fish, D.: Oxidation of atmospheric reduced sulphur compounds: Perspective from laboratory studies – Discussion, Phil. Trans. Roy. Soc. London, 352, 181–182, 1997.

Lee, Y. N. and Schwartz, S. E.: Precipitation scavenging, dry deposition and resuspension, vol. 1., chap. Kinetics of oxidation of aqueous sulfur (IV) by nitrogen dioxide, Elsevier, New York, 1983.

Lightfoot, P. and Cox, R.: Organic peroxy-radicals – kinetics, spectroscopy and tropospheric chemistry, Atmos. Environ., 26, 1805–1961, 1992.

Loosmore, G. and Cederwall, R.: Precipitation scavenging of atmospheric aerosols for emergency response applications: testing an updated model with new real-time data, Atmos. Environ., 38, 993–1003, 2004.

Louis, J., Tiedke, M., and Geleyn, J.: A short history of the PBL parametrization at ECMWF, in: ECMWF Workshop on Planetary Boundary Layer parametrization, 59–80, University of Reading, 1982.

Madronich, S., McKenzie, R. E., Bjorn, L. O., and Caldwell, M. M.: Changes in biologically active ultraviolet radiation reaching the Earth's surface, J. Photochem. Photobiol. B,, 46, 5–19, 1998.

Marticorena, B. and Bergametti, G.: Modeling the atmospheric dust cycle: 1 Design of a soil derived dust production scheme, J. Geophys. Res., 100, 16415–16430, 1995.

Martinez, R. D., Buitrago, A. A., Howell, N. W., Hearn, C. H., and Joens, J. A.: The near UV absorption-spectra of several aliphatic-aldehydes and ketones at 300-K, Atmos. Environ., 26, 785–792, 1992.

McRae, G., Goodin, W., and Seinfeld, J.: Development of a second generation mathematical model for urban air pollution: I. model formulation, Atmos. Environ., 16, 679–696, 1982.

Mentel, T. F., Bleilebens, D., and Wahner, A.: A study of nighttime nitrogen oxide oxidation in a large reaction chamber – The fate of NO_2, N_2O_5, HNO_3, and O_3 at different humidities, Atmos. Environ., 30, 4007–4020, 1996.

Menut, L.: Adjoint modelling for atmospheric pollution processes sensitivity at regional scale during the ESQUIF IOP2, J. Geophys. Res., 108, 8562, doi:10.1029/2002JD002549, 2003.

Menut, L.: Sensitivity of hourly Saharan dust emissions to NCEP and ECMWF modelled wind speed, J. Geophys. Res. Atmos., 113, D16201, doi:10.1029/2007JD009522, 2008.

Menut, L. and Bessagnet, B.: Atmospheric composition forecasting in Europe, Ann. Geophys., 28, 61–74, doi:10.5194/angeo-28-61-2010, 2010.

Menut, L., Vautard, R., Beekmann, M., and Honoré, C.: Sensitivity of Photochemical Pollution using the Adjoint of a Simplified Chemistry-Transport Model, J. Geophys. Res., 105, 15379–15402, 2000a.

Menut, L., Vautard, R., Flamant, C., Abonnel, C., Beekmann, M., Chazette, P., Flamant, P. H., Gombert, D., Guédalia, D., Kley, D., Lefebvre, M. P., Lossec, B., Martin, D., Mégie, G., Perros, P., Sicard, M., and Toupance, G.: Measurements and modelling of atmospheric pollution over the Paris area: an overview of the ESQUIF Project, Ann. Geophys., 18, 1467–1481, doi:10.1007/s00585-000-1467-y, 2000b.

Menut, L., Coll, I., and Cautenet, S.: Impact of meteorological data resolution on the forecasted ozone concentrations during the ESCOMPTE IOP 2a and 2b, Atmos. Res., 74, 139–159, 2005a.

Menut, L., Schmechtig, C., and Marticorena, V.: Sensitivity of the sandblasting fluxes calculations to the soil size distribution accuracy, J. Atmos. Ocean. Technol., 22, 1875–1884, 2005b.

Menut, L., Foret, G., and Bergametti, G.: Sensitivity of mineral dust concentrations to the model size distribution accuracy, J. Geophys. Res. Atmos., 112, D10210, doi:10.1029/2006JD007766, 2007.

Menut, L., Chiapello, I., and Moulin, C.: Previsibility of mineral dust concentrations: The CHIMERE-DUST forecast during the first AMMA experiment dry season, J. Geophys. Res. Atmos., 114, D07202, doi:10.1029/2008JD010523, 2009a.

Menut, L., Masson, O., and Bessagnet, B.: Contribution of Saharan dust on radionuclides aerosols activity levels in Europe? The 21–22 February 2004 case study, J. Geophys. Res. Atmos., 114, D16202, doi:10.1029/2009JD011767, 2009b.

Menut, L., Goussebaile, A., Bessagnet, B., Khvorostiyanov, D., and Ung, A.: Impact of realistic hourly emissions profiles on air pollutants concentrations modelled with CHIMERE, Atmos. Environ., 49, 233–244, doi:10.1016/j.atmosenv.2011.11.057, 2012.

Menut, L., Bessagnet, B., Colette, A., and Khvorostyanov, D.: On the impact of the vertical resolution on chemistry transport modelling, Atmos. Environ., 67, 370–384, 2013.

Middleton, P., Stockwell, W. R., and Carter, W. P.: Agregation and analysis of volatile organic compound emissions for regional modelling, Atmos. Environ., 24, 1107–1133, 1990.

Milford, J. and Davidson, C.: The sizes of particulate trace elements in the atmosphere-a review, J. Air Pollut. Control Assoc., 35, 1249–1260, 1985.

Mircea, M. and Stefan, S.: A theoretical study of the microphysical parameterization of the scavenging coefficient as a function of precipitation type and rate, Atmos. Environ., 32, 2931–2938, 1998.

Molnar, A., Meszaros, E., Polyak, K., Borbely-Kiss, I., Koltay, E., G., S., and Horvath, Z.: Atmospheric budget of different elements in aerosol particles over Hungary, Atmos. Environ., 29, 1821–1828, 1995.

Monahan, E. C.: In The Role of Air-Sea Exchange in Geochemical Cycling, chap. The ocean as a source of atmospheric particles, Kluwer Academic Publishers, Dordrecht, Holland, 129–163, 1986.

Monks, P. E. A.: Atmospheric composition change – global and regional air quality, Atmos. Environ., 43, 5268–5350, 2009.

Nenes, A., Pilinis, C., and Pandis, S.: ISORROPIA: A new thermodynamic model for inorganic multicomponent atmospheric aerosols, Aquatic Geochem., 4, 123–152, 1998.

Odum, J. R., Jungkamp, T. P. W., Griffin, R. J., Forster, H. J. L., Flagan, R. C., and Seinfeld, J. H.: Aromatics, reformulated gasoline and atmospheric organic aerosol formation, Environ. Sci. Technol., 31, 1890–1897, 1997.

Oliviè, D. J. L., van Velthoven, P., Beljaars, A., and Kelder, H.: Comparison between archived and off-line diagnosed convective mass fluxes in the chemistry transport model TM3, J. Geophys. Res., 109, D11303, doi:10.1029/2003JD004036, 2004.

Pankow, J. F.: An absorption model of gas/aerosol partition involved in the formation of secondary organic aerosol, Atmos. Environ., 28, 189–193, 1994.

Paulson, S. E. and Seinfeld, J. H.: Development and evaluation of a photooxidation mechanism for isoprene, J. Geophys. Res., 97, 20703–20715, 1992.

Péré, J. C., Mallet, M., Pont, V., and Bessagnet, B.: Impact of aerosol direct radiative forcing on the radiative budget, surface heat fluxes, and atmospheric dynamics during the heat wave of summer 2003 over western Europe: A modeling study, J. Geophys. Res., 116, D23119, doi:10.1029/2011JD016240, 2011.

Peters, K. and Eiden, R.: Modelling the dry deposition velocity of aerosol particles to a spruce forest, Atmos. Environ., 26A, 2555–2564, 1992.

Pirovano, G., Balzarini, A., Bessagnet, B., Emery, C., Kallos, G., Meleux, F., Mitsakou, C., Nopmongcol, U., Riva, G., and Yarwood, G.: Investigating impacts of chemistry and transport model formulation on model performance at European scale, Atmos. Environ., 53, 93–109, doi:10.1016/j.atmosenv.2011.12.052, 2012.

Pison, I., Menut, L., and Blond, N.: Inverse modeling of emissions for local photooxidant pollution: Testing a new methodology with kriging constraints, Ann. Geophys., 24, 1523–1535, doi:10.5194/angeo-24-1523-2006, 2006.

Pison, I., Menut, L., and Bergametti, G.: Inverse modeling of surface NOx anthropogenic emissions fluxes in the Paris area during the ESQUIF campaign, J. Geophys. Res. Atmos., 112, D24302, doi:10.1029/2007JD008871, 2007.

Plum, C. N., Sanhueza, E., Atkinson, R., Carter, W. P., and Pitts, J. N.: Hydroxyl radical rate constants and photolysis rates of alpha-dicarbonyls, Environ. Sci. Technol., 17, 479–484, 1983.

Priestley, C.: Heat transport and zonal stress between latitudes, Q. J. Roy. Meteorol., 75, 28–40, 1949.

Pryor, S., Schoof, J., and Barthelmie, R.: Empirical downscaling of wind speed probability distributions, J. Geophys. Res., 110, D19109, doi:10.1029/2005JD005899, 2005.

Pun, B. K., Seigneur, C., and Lohman, K.: Modeling secondary organic aerosol formation via multiphase partitioning with molecular data, Environ. Sci. Technol., 40, 4722–4731, 2006.

Rao, S., Galmarini, S., and Puckett, K.: Air Quality Model Evaluation International Initiative (AQMEII): Advancing the State of the Science in Regional Photochemical Modeling and Its Applications, Bull. Am. Meteor. Soc., 92, 23–30, 2011.

Rio, C., Hourdin, F., and Chédin, A.: Numerical simulation of tropospheric injection of biomass burning products by pyro-thermal plumes, Atmos. Chem. Phys., 10, 3463–3478, doi:10.5194/acp-10-3463-2010, 2010.

Roberts, G. J. and Wooster, M. J.: Fire Detection and Fire Characterization Over Africa Using Meteosat SEVIRI, IEEE Trans. Geosci. Remote Sens., 46, 1200–1218, 2008.

Robinson, A. L., Donahue, N. M., Shrivastava, M. K., Weitkamp, E., Sage, A. M., Grieshop, A. P., Lane, T. E., Pandis, S. N., and Pierce, J. R.: Rethinking organic aerosols: Semivolatile emissions and photochemical aging, Science, 315, 1259–1262, 2007.

Rogers, C., Wayne, P., Macklin, E., Muilenberg, M., and Wagner, C.: Interaction of the onset of spring and elevated atmospheric CO_2 on ragweed (Ambrosia artemisiifolia L.) pollen production, Environ. Health Perspect., 114, 865–869, 2006.

Rouïl, L., Honoré, C., Vautard, R., Beekmann, M., Bessagnet, B., Malherbe, L., Meleux, F., Dufour, A., Elichegaray, C., Flaud, J., Menut, L., Martin, D., Peuch, A., Peuch, V., and Poisson, N.: PREV'AIR : an operational forecasting and mapping system for air quality in Europe, B. Am. Meteorol. Soc., 90, 73–83, doi:10.1175/2008BAMS2390.1, 2009.

Royer, P., Chazette, P., Sartelet, K., Zhang, Q. J., Beekmann, M., and Raut, J.-C.: Comparison of lidar-derived PM_{10} with regional modeling and ground-based observations in the frame of MEGAPOLI experiment, Atmos. Chem. Phys., 11, 10705–10726, doi:10.5194/acp-11-10705-2011, 2011.

Ryaboshapko, A., Ilyin, I., Gusev, A., Afinogenova, O., Berg, T., and Hjellbrekke, A.: Monitoring and Modelling of Lead, Cadmium and Mercury Transboundary Transport in the Atmosphere of Europe, EMEP/MSC-E Report, Meteorological Synthesizing Centre East, Moscow, Russia, 1/99, 1999.

Rybnicek, O. and Jaeger, S.: Ambrosia (Ragweed) in Europe, in: ACI International, Allergy and Clinical Immunology International, Hofgrefe and Huber Publishers, March/April 2001, 13, 60–66, 2001.

Sander, G. C., Parlange, J.-Y., Smith, R. E., Haverkamp, R., and Hogarth, W.: Estimation of ponding time for constant surface flux, Hydrology days, AGU Pub. 19, San Francisco, 402–410, 1999.

Sander, S., Friedl, R., Golden, D., Kurylo, M., Moortgat, G., Keller-Rudek, H., Wine, P., Ravishankara, A., Kolb, C., Molina, M., Finlayson-Pitts, B., Huie, R., and Orkin, V.: Chemical Kinetics and Photochemical Data for Use in Atmospheric Studies, Evaluation Number 15, JPL Publication 06-2, Jet Propulsion Laboratory, 2006.

Saunders, S. M., Jenkin, M. E., Derwent, R. G., and Pilling, M. J.: Protocol for the development of the Master Chemical Mechanism, MCM v3 (Part A): tropospheric degradation of non-aromatic volatile organic compounds, Atmos. Chem. Phys., 3, 161–180, doi:10.5194/acp-3-161-2003, 2003.

Schaap, M., Vautard, R., Bergstrom, R., van Loon, M., Bessagnet, B., Brandt, J., Christensen, H., Cuvelier, K., Foltescu, V., Graff, A., E., J. J., Kerschbaumer, A., Krol, M., Langner, J., Roberts, P., Rouil, L., Stern, R., Tarrason, L., Thunis, P., Vignati, E., White, L., Wind, P., and Builtjes, P. H. J.: Evaluation of long-term aerosol simulations from seven air quality models and their ensemble in the EURODELTA study, Atmos. Environ., 41, 2083–2097, 2007.

Schere, K., Flemming, J., Vautard, R., Chemel, C., Colette, A., Hogrefe, C., Bessagnet, B., Meleux, F., Mathur, R., Roselle, S., Hu, R.-M., Sokhi, R. S., Rao, S. T., and Galmarini, S.: Trace gas/aerosol boundary concentrations and their impacts on continental-scale AQMEII modeling domains, Atmos. Environ., 53, 38–50, doi:10.1016/j.atmosenv.2011.09.043, 2012.

Schmidt, H., Derognat, C., Vautard, R., and Beekmann, M.: A comparison of simulated and observed ozone mixing ratios for the summer of 1998 in western Europe, Atmos. Environ., 35, 6277–6297, 2001.

Seigneur, C. and Constantinou, E.: Chemical Kinetic Mechanism for Atmospheric Chromium, Environ. Sci. Technol., 29, 222–231, 1995.

Seiler, W. and Crutzen, P.: Estimates of gross and net fluxes of carbon between the biosphere and the atmosphere from biomass burning, Climatic Change, 2, 207–247, doi:10.1007/BF00137988, 1980.

Seinfeld, J. H. and Pandis, S. N.: Atmospheric chemistry and physics: From air pollution to climate change, Wiley-Interscience, J. Wiley, New York, 1997.

Shao, Y. and Lu, I.: A simple expression for wind erosion threshold friction velocity, J. Geophys. Res., 105, 22437–22443, 2000.

Simpson, D.: Long period modeling of photochemical oxidants in Europe, Calculations for July 1985, Atmos. Environ., 26, 1609–1634, 1992.

Skamarock, W., Klemp, J., Dudhia, J., Gill, D., Barker, D., Wang, W., and Powers, J.: A Description of the Advanced Research WRF Version 2, NCAR Technical Note, Boulder, Colorado, USA, NCAR/TN–468+STR, 2007.

Slinn, W.: Precipitation scavenging, Division of Biomedical Environmental Research, US Department of Energy, Washington, DC, Atmospheric Sciences and Power Production 1979, 1983.

Sofiev, M., Siljamo, P., Ranta, H., and Rantio-Lehtimaki, A.: Towards numerical forecasting of long-range air transport of birch pollen: theoretical considerations and a feasibility study, Int. J. Biometeorol., 50, 392–402, 2006.

Sofiev, M., Siljamo, P., Ranta, H., Linkosalo, T., Jaeger, S., Rasmussen, A., Rantio-lehtimaki, A., Severova, E., and Kukkonen, J.: A numerical model of birch pollen emission and dispersion in the atmosphere, Description of the emission module, Int. J. Biometeorol., 57-1, 45–58, 2013.

Solazzo, E., Bianconi, R., Pirovano, G., Matthias, V., Vautard, R., Moran, M. D., Appel, K. W., Bessagnet, B., Brandt, J., Christensen, J. H., Chemel, C., Coll, I., Ferreira, J., Forkel, R., Francis, X. V., Grell, G., Grossi, P., Hansen, A. B., Miranda, A. I.,

Nopmongcol, U., Prank, M., Sartelet, K. N., Schaap, M., Silver, J. D., Sokhi, R. S., Vira, J., Werhahn, J., Wolke, R., Yarwood, G., Zhang, J., Rao, S. T., and Galmarini, S.: Operational model evaluation for particulate matter in Europe and North America in the context of AQMEII, Atmos. Environ., 53, 75–92, doi:10.1016/j.atmosenv.2012.02.045, 2012a.

Solazzo, E., Bianconi, R., Vautard, R., Appel, K. W., Moran, M. D., Hogrefe, C., Bessagnet, B., Brandt, J., Christensen, J. H., Chemel, C., Coll, I., van der Gon, H. D., Ferreira, J., Forkel, R., Francis, X. V., Grell, G., Grossi, P., Hansen, A. B., Jericevic, A., Kraljevic, L., Miranda, A. I., Nopmongcol, U., Pirovano, G., Prank, M., Riccio, A., Sartelet, K. N., Schaap, M., Silver, J. D., Sokhi, R. S., Vira, J., Werhahn, J., Wolke, R., Yarwood, G., Zhang, J., Rao, S., and Galmarini, S.: Model evaluation and ensemble modelling of surface-level ozone in Europe and North America in the context of AQMEII, Atmos. Environ., 53, 60–74, doi:10.1016/j.atmosenv.2012.01.003, 2012b.

Sovde, O. A., Gauss, M., Smyshlyaev, S. P., and Isaksen, I. S. A.: Evaluation of the chemical transport model Oslo CTM2 with focus on arctic winter ozone depletion, J. Geophys. Res. Atmos., 113, D11303, doi:10.1029/2007JD009240, 2008.

Stern, R., Builtjes, P., Schaap, M., Timmermans, R., Vautard, R., Hodzic, A., Memmesheimer, M., Feldmann, H., Renner, E., Wolke, R., and Kerschbaumer, A.: A model inter-comparison study focusing on episodes with elevated PM_{10} concentrations, Atmos. Environ., 42, 4567–4588, 2008.

Stohl, A., Williams, E., Wotawa, G., and Kromp-Kolb, H.: A European inventory of soil nitric oxide emissions and the effect of these emissions on the photochemical formation of ozone, Atmos. Environ., 30, 3741–3755, doi:10.1016/1352-2310(96)00104-5, 1996.

Szopa, S., Foret, G., Menut, L., and Cozic, A.: Impact of large scale circulation on European summer surface ozone: consequences for modeling, Atmos. Environ., 43, 1189–1195, doi:10.1016/j.atmosenv.2008.10.039, 2009.

Thunis, P., Rouil, L., Stern, R., Kerschbaumer, A., Bessagnet, B., Builtjes, P., Douros, J., Moussiopoulos, N., Pirovano, G., and Bedogni, M.: Analysis of model responses to emission-reduction scenarios within the City-Delta project, Atmos. Environ., 41, 208–220, 2007.

Tiedtke, M.: A comprehensive mass flux scheme for cumulus parameterization in large-scale models, Mon. Weather Rev., 117, 1779–1800, 1989.

Troen, I. and Mahrt, L.: A simple model of the atmospheric boundary layer: Sensitivity to surface evaporation, Bound.-Lay. Meteorol., 37, 129–148, 1986.

Tsyro, S.: First estimates of the effect of aerosol dynamics in the calculation of PM_{10} and $PM_{2.5}$, EMEP report, 4/02, Norwegian Meteorological Institute, Oslo, 2002.

Turquety, S.: Fire emission inventory for the Euro-Mediterranean region: variability, uncertainty and adaptability to short-term forecasting, Geosci. Model Dev. Discuss., in preparation, 2012.

Ullrich, P. A., Jablonowski, C., and Leer, B. V.: High-order finite-volume methods for the shallow-water equations on the sphere, J. Comput. Phys, 229, 6104–6134, doi:10.1016/j.jcp.2010.04.044, 2010.

Valari, M. and Menut, L.: Does an increase in air quality models resolution bring surface ozone concentrations closer to reality?, J. Atmos. Ocean. Technol., 25, 1955–1968,

doi:10.1175/2008JTECHA1123.1, 2008.

Valari, M. and Menut, L.: Transferring the heterogeneity of surface emissions to variability in pollutant concentrations over urban areas through a chemistry transport model, Atmos. Environ., 44, 3229–3238, 2010.

Valari, M., Chatignoux, E., and Menut, L.: Using a chemistry transport model to account for the spatial variability of exposure-concentrations in epidemiologic air pollution studies, J. Air Waste Manage. Assoc., 61, 164–179, 2011.

Van der Gon, D. H., van het Bolscher, M., Visschedijk, A., and Zandveld, P.: Study to the effectiveness of the UNECE Heavy Metals Protocol and costs of possible additional measures, Phase I: Estimation of emission reduction resulting from the implementation of the HM Protocol, TNO-report, TNO Utrecht, The Netherlands, p. 193, 2005.

van der Werf, G. R., Randerson, J. T., Giglio, L., Collatz, G. J., Mu, M., Kasibhatla, P. S., Morton, D. C., DeFries, R. S., Jin, Y., and van Leeuwen, T. T.: Global fire emissions and the contribution of deforestation, savanna, forest, agricultural, and peat fires (1997–2009), Atmos. Chem. Phys., 10, 11707–11735, doi:10.5194/acp-10-11707-2010, 2010.

Van Leer, B.: Towards the ultimate conservative difference scheme, V A second order sequel to Godunov's method, J. Computational Phys., 32, 101–136, 1979.

Van Loon, M., Vautard, R., Schaap, M., Bergstrom, R., Bessagnet, B., Brandt, J., Builtjes, P., Christensen, J. H., Cuvelier, K., Graf, A., Jonson, J., Krol, M., Langner, J., Roberts, P., Rouil, L., Stern, R., Tarrason, L., Thunis, P., Vignati, E., White, L., and Wind, P.: Evaluation of long-term ozone simulations from seven regional air quality models and their ensemble average, Atmos. Environ., 41, 2083–2097, 2007.

Vautard, R., Beekmann, M., and Menut, L.: Applications of adjoint modelling in atmospheric chemistry: sensitivity and inverse modelling, Environ. Model. Softw., 15, 703–709, 2000.

Vautard, R., Beekmann, M., Roux, J., and Gombert, D.: Validation of a hybrid forecasting system for the ozone concentrations over the Paris area, Atmos. Environ., 35, 2449–2461, 2001.

Vautard, R., Menut, L., Beekmann, M., Chazette, P., Flamant, P., Gombert, D., Guedalia, D., Kley, D., Lefebvre, M., Martin, D., Megie, G., Perros, P., and Toupance, G.: A synthesis of the Air Pollution over the Paris Region (ESQUIF) field campaign, J. Geophys. Res.-Atmos., 108, 8558, doi:10.1029/2003JD003380, 2003.

Vautard, R., Bessagnet, B., Chin, M., and Menut, L.: On the contribution of natural Aeolian sources to particulate matter concentrations in Europe: testing hypotheses with a modelling approach, Atmos. Environ., 39, 3291–3303, 2005.

Vautard, R., Maidi, M., Menut, L., Beekmann, M., and Colette, A.: Boundary layer photochemistry simulated with a two-stream convection scheme, Atmos. Environ., 41, 8275–8287, 2007.

Vautard, R., Schaap, M., Bergstrom, R., Bessagnet, B., Brandt, J., Builtjes, P., Christensen, J., Cuvelier, C., Foltescu, V., Graf, A., Kerschbaumer, A., Krol, M., Roberts, P., Rouil, L., Stern, R., Tarrason, L., Thunis, P., Vignati, E., and Wind, P.: Skill and uncertainty of a regional air quality model ensemble, Atmos. Environ., 39, 2957–2967, 2009.

Verwer, J.: Gauss-Seidel iteration for stiff ODEs from chemical kinetics, J. Sci. Comput., 15, 1243–1250, 1994.

Vestreng, V.: Review and revision of emission data reported to CLR-TAP, EMEP Status report, Norwegian Meteorological Institute, Oslo, 2003.

Vestreng, V., Ntziachristos, L., Semb, A., Reis, S., Isaksen, I. S. A., and Tarrasón, L.: Evolution of NO_x emissions in Europe with focus on road transport control measures, Atmos. Chem. Phys., 9, 1503–1520, doi:10.5194/acp-9-1503-2009, 2009.

Vivanco, M., Palomino, I., Vautard, R., Bessagnet, B., Martin, F., Menut, L., and Jimenez, S.: Multi-year assessment of photochemical air quality simulation over Spain, Environ. Model. Softw., 24, 63–73, doi:10.1016/j.envsoft.2008.05.004, 2008.

Vivanco, M., Gonzalez, M., Palomino, I., Garrido, J., Querol, X., Bessagnet, B., de la Rosa, J., and Sanchez de la Campa, A.: Modelling Arsenic, Lead, Cadmium and Nickel Ambient Air Concentrations in Spain, in: Computational Science and Its Applications (ICCSA), 2011 International Conference, Santander Spain, 20–23 June 2011, 243–246, doi:10.1109/ICCSA.2011.54, 2011.

Vuolo, M., Chepfer, H., Menut, L., and Cezana, G.: Comparison of mineral dust layers vertical structures modelled with CHIMERE-DUST and observed with the CALIOP lidar, J. Geophys. Res. Atmos., 114, D09214, doi:10.1029/2008JD011219, 2009a.

Vuolo, M., Menut, L., and Chepfer, H.: Impact of transport schemes accuracy on modelled dust concentrations variability, J. Atmos. Ocean. Technol., 26, 1135–1143, doi:10.1175/2008JTECHA1197.1, 2009b.

Warren, D. R.: Nucleation and growth of aerosols, Ph.D. thesis, Dissertation (Ph.D.), California Institute of Technology, Pasadena, 1986.

Wesely, M.: Parameterization of Surface Resistances to Gaseous Dry Deposition in Regional-Scale Numerical Models, Atmos. Environ., 23, 1293–1304, 1989.

Wiedinmyer, C., Akagi, S. K., Yokelson, R. J., Emmons, L. K., Al-Saadi, J. A., Orlando, J. J., and Soja, A. J.: The Fire INventory from NCAR (FINN): a high resolution global model to estimate the emissions from open burning, Geosci. Model Dev., 4, 625–641, doi:10.5194/gmd-4-625-2011, 2011.

Wilson, R. C., Fleming, Z. L., Monks, P. S., Clain, G., Henne, S., Konovalov, I. B., Szopa, S., and Menut, L.: Have primary emission reduction measures reduced ozone across Europe? An analysis of European rural background ozone trends 1996–2005, Atmos. Chem. Phys., 12, 437–454, doi:10.5194/acp-12-437-2012, 2012.

Wu, L., Mallet, V., Bocquet, M., and Sportisse, B.: A comparison study of data assimilation algorithms for ozone forecasts, J. Geophys. Res. Atmos., 113, D20310, doi:10.1029/2008JD009991, 2008.

Zhang, L., Gong, S., Padro, J., and Barrie, L.: A size-segregated particle dry deposition scheme for an atmospheric aerosol module, Atmos. Environ., 35, 549–560, 2001.

Zhang, Y., Huang, J.-P., Henze, D. K., and Seinfeld, J. H.: Role of isoprene in secondary organic aerosol formation on a regional scale, J. Geophys. Res. Atmos., 112, D20207, doi:10.1029/2007JD008675, 2007.

Zyryanov, D., Foret, G., Eremenko, M., Beekmann, M., Cammas, J.-P., D'Isidoro, M., Elbern, H., Flemming, J., Friese, E., Kioutsioutkis, I., Maurizi, A., Melas, D., Meleux, F., Menut, L., Moinat, P., Peuch, V.-H., Poupkou, A., Razinger, M., Schultz, M., Stein, O., Suttie, A. M., Valdebenito, A., Zerefos, C., Dufour, G., Bergametti, G., and Flaud, J.-M.: 3-D evaluation of tropospheric ozone simulations by an ensemble of regional Chemistry Transport Model, Atmos. Chem. Phys., 12, 3219–3240, doi:10.5194/acp-12-3219-2012, 2012.